

Remediation of an anoxic arsenic-contaminated site with Zero Valent Iron (ZVI)

- Evaluation of a field study and subsequent mobility experiments with sulfidized ZVI

Clara Kieschnick-Llamas

Degree project/Independent project • 60 credits Swedish University of Agricultural Sciences, SLU Department of Soil and Environment Soil, Water, and Environment



Remediation of an anoxic arsenic-contaminated site with Zero Valent Iron (ZVI)

Evaluation of a field study and subsequent mobility experiments with sulfidized ZVI

Clara Kieschnick-Llamas

Supervisor: Geert Cornelis, SLU, Department of Soil and Environment

Assistant supervisor: Dan Berggren Kleja, SLU, Department of Soil and

Environment

Assistant supervisor: Wiebke Mareile Heinze, SLU, Department of Soil and

Environment

Examiner: Erik Karltun, SLU, Department of Soil and Environment

Credits: 60 hp Level: A2E

Course title: Master thesis in Environmental Science

Course code: EX0899

Programme/education: Soil, Water, and Environment

Course coordinating dept: Department of Soil and Environment

Place of publication: Uppsala, Sweden

Year of publication: 2025 Partnumber: 2025:20

Series title: Examensarbeten/Institutionen för Mark och miljö, SLU

Copyright: All featured images are used with permission from the

copyright owner.

Keywords: Zero Valent Iron, ZVI, Arsenic, Anoxic, Column Experiment,

Remediation, Immobilization, Mobility

Swedish University of Agricultural Sciences

Faculty of Natural Resources and Agricultural Sciences Department of Soil and Environment

Abstract

Arsenic (As) is a toxic metalloid that can lead to serious health effects. Based on promising lab results, microscale and nanoscale zero valent iron (mZVI and nZVI) were injected into an anoxic As-contaminated site in Sweden as a remediation effort. However, monitoring showed a limited effect on groundwater As concentrations. For this study, we took groundwater and soil samples, along with x-ray absorption spectroscopy (XAS) measurements, to determine why the pilot test was mostly unsuccessful. Aggregation upon injection was the main cause of poor performance for mZVI: there were concentrated high levels of solid-phase Fe and visible black clumps in soil cores. As a result, mZVI had no impact on groundwater conditions. On the other hand, nZVI showed an impact on groundwater conditions at one sample point. At this point, the nZVI had a better distribution than mZVI, but was limited to upper layers of the aquifer, and did not have a large-scale impact. Additionally, after 2 years in the field it had not fully corroded—up to 38% of Fe(0) remained in some areas. Groundwater conditions were more reducing than expected, leading to As(III), the more toxic and mobile species of As, dominating over As(V) in the groundwater at all sites, further limiting As immobilization. Immobilization mechanisms were very different compared to previous lab studies, with sulfur (S) playing a bigger role than expected, as monothioarsenate, orpiment, realgar, and arsenopyrite were present. Sulfidized mZVI (S-mZVI) has been shown to be more mobile than unmodified ZVI, so follow-up short-term column experiments were conducted at varying flow speeds with sediment material from this field site to determine feasibility for future implementation. Overall, recovery rates (of <2% for all flow rates) were not promising. Subsequent modeling with HYDRUS-1D, however, showed evidence of heavy blocking (when the binding of particles to a collector limits the binding of subsequent particles), a property which could be beneficial for field distribution of S-mZVI. This study shows the limitations of transferring successful lab tests to the field. It also indicates that ZVI, regardless of size, is not an effective remediation strategy for As at this site, where heterogeneous ZVI distribution and very reducing conditions are strong limiting factors. S-mZVI, however, could be a promising remediation strategy in the field, despite recovery rates in the lab.

Popular scientific abstract

Arsenic (As) is a toxic metal found globally in drinking water. Toxic levels are of special concern in parts of South Asia, South America, and the USA, where naturally high levels are common. Human-caused sources of As are also a concern. One such source is from wood impregnation plants, where wood impregnation products (since banned in the EU) used As to prevent fungal growths on wood. At a wood impregnation site in Hjältevad, Sweden, a vat of the arsenic-containing product leaked into the groundwater in 1968. Despite remediation efforts, As levels in the groundwater continue to rise. The site is especially difficult to remediate because the groundwater is oxygen-depleted (it is "anoxic"), so a more toxic and mobile form of As dominates.

Zero Valent Iron (ZVI) is a remediation tool that has been effective for other contaminants. At a lab scale, it has also been successful for immobilizing As, including under anoxic conditions. There have been, however, limited studies on field-scale applications for As in anoxic conditions. Two years ago, two sizes of ZVI (microscale [mZVI] and nanoscale [nZVI]) were injected in a pilot trial at the Hjältevad site, in a remediation attempt. Subsequent monitoring, though, showed little impact on total As concentrations. In this study, we took both groundwater and soil samples around the injection points to determine why the injection was unsuccessful.

The main factor for poor mZVI performance was limited ZVI spreading—instead of spreading evenly, mZVI aggregated around the injection points. With these high levels of aggregation, As in the groundwater only came in contact with the outer layer of ZVI, and inner layers did not interact with As-contaminated water at all. As a result, the total immobilized As was very small. At the same time, nZVI did show an impact on As concentrations at one sample point. This point showed better nZVI distribution than mZVI, but it was limited to the upper layers of the soil. Although the nZVI chemistry worked, the distribution was still too limited to have a large-scale impact on As levels.

Some key factors in lab conditions differed from the field, giving an indication of why the field-scale application showed such different results from lab tests. First, the field area where ZVI was injected was much more anoxic than in the lab, so the more toxic and mobile form of As was favored, limiting As immobilization (in its less mobile form, As would bind easier to ZVI). Temperature could also have played a role—lab experiments were conducted at room temperature (25°C), while the field has an average temperature of 6°C. Under cold conditions, reactions, including ZVI corrosion, are much slower than at room temperature. ZVI corrosion is imperative for As binding, and results showed that up to 38% of nZVI at some points had not corroded.

S-mZVI is ZVI with an iron sulfide (FeS) coating. This coating should make it more mobile, so in a follow-up lab experiment we examined its mobility with sediment from this site. Results, however, showed limited mobility of S-mZVI. At the same time, lab conditions are quite different from the field, so a field injection could still prove to be successful.

Overall, this study demonstrates the gap between lab and field studies, and the difficulty in simulating field conditions accurately at a lab scale. Additionally, it indicates that ZVI is not an effective remediation strategy at this site.

Acknowledgements

I would like to thank first and foremost my supervisor, Geert Cornelis, and my cosupervisors Dan Berggren-Kleja and Wiebke Mareile Heinze for their support, guidance, and encouragement during this thesis. Thank you to Erik Karltun, my examiner, and Lisa Deiglmayr, my student opponent, for their feedback. A special thanks to Sweco, Niras, and Sonic Geo Drill for their contribution to field work sample collection, as well as Regenesis for their collaboration on the column experiments. I would also like to thank Jon-Petter Gustafsson, Carin Sjöstedt, and Kajsa Sigfridsson Clauss for their contribution to sample preparation, execution, and analysis of x-ray absorption spectroscopy at MAX IV. Finally, a special thanks to Mina Spångberg, Marloes Groeneveld, and Ylva Bellander for all their help in the lab.

Table of contents

Ackr	nowledgements	6
List	of tables	9
List	of figures	10
Abbı	reviations	15
1.	Introduction	16
2.	Theoretical background	19
2.1	Arsenic	19
2.2	Zero Valent Iron (ZVI)	20
2.3	Sulfidated Zero-Valent Iron (S-ZVI)	23
2.4	ZVI and particle mobility	25
2.5	Colloid Filtration Theory (CFT)	27
3.	Site description and previous findings	
3.1	Overview	_
3.2	History of arsenic contamination	
3.3	State of arsenic pollution	
3.4	ZVI injection: previous pilot study	
3.5	Initial findings	
	3.5.1 Batch tests and column experiments	
	3.5.2 Mobility column experiments	
	3.5.3 Pre-injection groundwater samples	
	3.5.4 Post-injection monitoring	
	3.5.5 Long-term monitoring	40
4.	Materials and methods	42
4.1	Groundwater samples	
4.2	Soil samples	44
4.3	X-ray absorption spectroscopy	
4.4	Column experiments with S-MicroZVI	
4.5	Mobility modeling	48
5.	Results	
5.1	mZVI treatment plot	
	5.1.1 Groundwater	
	5.1.2 Soil samples	
	5.1.3 X-ray fluorescence measurements	60

5.2	nZVI treatment site	61
	5.2.1 Groundwater	61
	5.2.2 Soil samples	63
	5.2.3 X-ray fluorescence measurements	66
	5.2.4 X-ray absorption spectroscopy	69
5.3	Column transport experiments with S-MicroZVI	74
6.	Discussion	78
6.1	mZVI injection site	78
6.2	nZVI injection site	79
6.3	ZVI reaction mechanisms in the field compared to the lab	81
	6.3.1 Differing groundwater conditions	81
	6.3.2 XAS binding mechanisms	82
6.4	S-microZVI recovery and mobility	85
7.	Conclusion	87
Refe	rences	88
Appe	endix	96

List of tables

Table 1. Total As and Fe(0) remaining in solution after phases A and B of batch tests.	
Data from Formentini et al. 2024.	. 35
Table 2. Monitoring well depths for wells shown in Fig. 11b and 11c	.41
Table 3. Numerical results for the second replicate of column experiments. Effective porosity, dispersivity, attachment coefficient, and S _{max} are all fitted by the	
Hydrus-1D model	.75

List of figures

Figure 1.	As stability diagram at 25°C for a typical pH and Eh range for groundwater. Stability lines were calculated using thermodynamic data from the database of Visual MINTEQ, vers. 3.1 (Gustafsson 2013). Gray shading shows the typical pH range for untreated pore waters
Figure 2.	Immobilization mechanisms for As(III) and As(V) by nZVI (left) and S-nZVI (right). Figure from Singh et al. 2021
Figure 3.	Effect of pH on As(III) and As(V) sorption to ferrihydrite. Model made with Visual MINTEQ ver 4.0 (Gustafsson 2013). Inputs are 10 μM As(III), 10 μM As(V), and 0.03 g L ⁻¹ hydrous ferric oxide (ferrihdyrite). Values for inputs are from Dixit & Hering 2003.
Figure 4.	Overview map of the contaminated site. Figure from Cao et al. 202330
Figure 5.	Side profile of the injection zone and contamination plume, SSE-NNW. Double-verticle lines indicate groundwater wells, and singular lines represent dynamic groundwater sampling conducted right before mZVI and nZVI injection. Figure by Sweco for Berggren Kleja et al. 2024.
Figure 6.	Injection points for mZVI and nearby wells used for short-term monitoring. Figure (a) shows a map of the injection points, and (b) displays injection depths (bottom-up) and other injection data. Data from Berggren Kleja et al. 202433
Figure 7.	Injection points for nZVI and nearby wells used for short-term monitoring. Figure (a) shows a map of the injection points, and (b) displays injection depths and other injection data. All points were injected bottom-up except na7, which was injected top-down. Data from Berggren Kleja et al. 2024
Figure 8.	Stability diagram for sorbed-phase (red line) and solution-phase (black lines) As(III) and As(V), overalyed with Eh/pH of water conditions from batch tests after Phase A (uncontrolled pH) and B (pH 7). From Formentini et al. 202435
Figure 9.	Total aqueous As, Eh, and pH in the groundwater in wells near the mZVI (a-c) and nZVI (d-f) injection points right before injection, with depth in meters above sea level (MASL). A map of these wells can be found in Fig. 6 (mZVI) and Fig. 7 (nZVI). Data from Berggren Kleja et al. 2024
Figure 10	Dissolved organic carbon (DOC), total aqueous As, pH, and Eh in the groundwater in wells near the injection points for 30-40 weeks after injection for both mZVI (a-d) and nZVI (e-h). Map of the wells can be found in Fig. 6 (mZVI) and Fig. 7 (nZVI). Data from Berggren Kleja et al. 2024

Figure 11	. Map of monitoring wells in the area alongside As data. Figure (a) is an overview map of injection points and permanent monitoring wells. Graph (b) shows As levels in TB8 over time, and (c) shows other relevant monitoring wells (ones in the vicinity of the injection points with data collected both before and after injection). Data from 2022 was collected before the injections. Figure (a) and data for (b) and (c) are from Sweco 2025
Figure 12	. Groundwater and soil sampling images: the geoprobe, for groundwater sampling (a) ; the sonic drill, for soil sampling (b) ; an anoxic sample being taken (c) , and x-ray fluorescence (XRF) measurements taken directly on a soil core (d)
Figure 13	. Map of groundwater and soil samples at the mZVI injection site. X's represent points where only a groundwater sample was taken, whereas stars show areas where both a groundwater and soil sample were taken. Green circles have a radius of 1 m
Figure 14	. Map of groundwater and soil samples at the nZVI injection site. X's represent points where only a groundwater sample was taken, whereas the star shows the point where both a groundwater and soil sample were taken. Green circles have a radius of 1.5 m
Figure 15	Column experimental set-up. Image (a) is the overall setup: pump [a1], ZVI stock solution [a2], column [a3], conductivity meter [a4], and fraction collector [a5]. Image (b) is a close-up of a packed column, and (c) shows the leachate collected in the fraction collector after 2 pore volumes of ZVI have been pumped through. Image (d) is the ZVI that settled in the bottom of the beaker during the experiment.
Figure 16	. Total aqueous As, Eh, pH, and percentage As(III) in the groundwater near the two most downstream mZVI injection points (mi4 and mi5), 2 years after injection, with depth in meters above sea level (MASL). Map of sample points is in Fig. 13. For comparison, pre-injection data is found in Fig. 9
Figure 17	. Pourbaix diagram for the distribution of aqueous As as either As(III) or As(V), overlayed with groundwater conditions from mZVI groundwater sampling. Graph (a) displays values at 25 °C—room temperature—and graph (b) at 6 °C, the average annual temperature of the aquifer. Stability lines were calculated using thermodynamic data from the database of Visual MINTEQ, vers. 3.1 (Gustafsson 2013).
Figure 18	. Solid-phase Fe and As concentrations for mZVI soil profiles ms1 (a) and ms12 (b). Depth is in meters above sea level (MASL). Boxes to the right of each graph represent successfully collected samples in dark gray, and attempted sample collection as a black box. No images were taken for these samples54

Figure 19	9. Soil profile for mZVI sampling point ms3 Fe and As results alongside groundwater data and images. Graph (a) shows solid-phase Fe and As concentrations. The box to the right of the graph represents successfully collected samples in dark gray, and attempted sample collection as a black box; red lines are samples taken separately from the larger 50 cm section due to visual presence of a dark Fe clump. The last sample extracted more soil than expected, and runs deeper than the attempted sample depth. Groundwater results corresponding to the soil sample point for total aqueous As (b), Eh (c), pH (d), and % As(III) (e) are also shown for comparison. Images of successful cores are represented with depths in meters above sea level (MASL) in (f). Red boxes correspond to zoomed-in photos to the right of the main image.
Figure 20	Soil profile for mZVI sampling point ms4 Fe and As results alongside groundwater data and images. Graph (a) shows solid-phase Fe and As concentrations. The box to the right of the graph represents successfully collected samples in dark gray, and attempted sample collection as a black box; the red line is a sample taken separately from the larger 50 cm section due to visual presence of a dark Fe clump. The last sample extracted more soil than expected, and runs deeper than the attempted sample depth. Groundwater results corresponding to the soil sample point for total aqueous As (b), Eh (c), pH (d), and % As(III) (e) are also shown for comparison. Images of successful cores are represented with depths in meters above sea level (MASL) in (f). Red boxes correspond to zoomed-in photos to the right of the main image.
Figure 21	Soil profile for mZVI sampling point ms5 Fe and As results alongside images. Solid-phase Fe and As concentrations (a) and photos of successful samples with depth in meters above sea level (MASL) (b) are shown. The box to the right of the graph represents successfully collected samples in dark gray, and attempted sample collection as a black box. The last sample extracted more soil than expected, and runs deeper than the attempted sample depth59
Figure 22	Soil profile for mZVI sampling point ms6 Fe and As results alongside images. Solid-phase Fe and As concentrations (a) and photos of successful samples with depths in meters above sea level (MASL) (b) are shown. Box to the right of the graph represents successfully collected sa ples in dark gray, and attempted sample collection as a black box.
Figure 23	. XRF measurements for solid-phase Fe for soil profiles ms3 (a) and ms4 (b) at the mZVI injection site. Depth is in meters above sea level (MASL). Profile ms3 is shown in more detail in Fig. 19 and ms4 in Fig. 20
Figure 24	. XRF measurements taken on mixed bulk samples for solid-phase Fe at all mZVI soil profiles. Two measurements were taken on each bag; an average of

	both is shown. Graphs (a-f) correspond to profiles ms1, ms3, ms4, ms5, ms6, and ms12, respectively. Depth is in meters above sea level (MASL)61
Figure 25	. Total aqueous As (a) , Eh (b) , pH (c) , and percentage As(III) (d) in the groundwater near nZVI injection point na4. Depth is in meters above sea level (MASL). Map of sample points is in Fig. 14. For comparison, pre-injection data is found in Fig. 9
Figure 26	Pourbaix diagram for the distribution of aqueous As as either As(III) or As(V), overlayed with groundwater conditions from nZVI groundwater sampling. Red points represent groundwater samples that correspond to the soil profile (used for XAS). Graph (a) displays values at 25 °C—room temperature—and graph (b) at 6 °C, the average annual temperature of the aquifer. Stability lines were calculated using thermodynamic data from the database of Visual MINTEQ, vers. 3.1 (Gustafsson 2013).
Figure 27	Soil core for nZVI Fe and As results alongside groundwater data and images. Graph (a) shows solid-phase Fe and As concentrations. The box to the right of the graph represents succesfully collected samples in dark gray, and attempted sample collection as a black box. Groundwater results corresponding to the soil sample point for total aqueous As (b), Eh (c), pH (d), and % As(III) (e) are also shown for comparison. Images of successful cores with depths in meters above sea level (MASL) are represented in (f). The red box corresponds to a zoomed-in photo to the right of the main image
Figure 28	. XRF measurements taken directly on the nZVI soil profile for solid-phase Fe and As. Depth is in meters above sea level (MASL)67
Figure 29	. XRF measurements taken on mixed bulk samples for solid-phase Fe and As for the nZVI soil profile. Depth is in meters above sea level (MASL). Two measurements were taken on each bag; an average of both is shown67
Figure 30	. Correlation between ALS solid-phase Fe results and XRF solid-phase Fe measurements. Graph (a) shows all points, and graph (b) omits the high-value outlier. Both mZVI and nZVI measurements are depicted
Figure 31	. Correlation between ALS solid-phase As results and XRF solid-phase As measurements. Only nZVI values are shown, as As levels were below the detection limit for XRF at the mZVI site
Figure 32	. Normalized As K-edge XANES spectra for anoxic nZVI samples. Graphs (a,b,c) show results, by depth and sample, and (d) includes standards for reference. Relevant reference lines are included in each graph. Analysis conducted by Jon-Petter Gustafsson
Figure 33	. Fractional distribution of As species from XANES analyses, by depth in meters above sea level (MASL). LCF analysis conducted by Jon-Petter Gustafsson. 71

Figure 34	. Fe and As solid-phase concentrations from anoxic samples used for XAS. Depth is in meters above sea level (MASL). Usually, 2 samples were taken per depth—both samples are plotted along with their average. The line connects the averages
Figure 35	Pourbaix diagrams for Fe (a) and As (b) in the presence of S and As or Fe, respectively. Groundwater conditions for mZVI from groundwater sampling are overlayed. Stability is modeled at 6°C. Soluble Fe and As content are averages from mZVI groundwater samples (8.21 mg L ⁻¹ and 741.13 mg L ⁻¹ , respectively). Concentration of S is an average of the whole study site (17 mg L ⁻¹), from Cao et al. 2023. Diagrams made in Geochemist's Workbench vers. 18 (Bethke 2022).
Figure 36	Pourbaix diagrams for Fe (a) and As (b) in the presence of S and As or Fe, respectively. Groundwater conditions for nZVI from groundwater sampling are overlayed. Red points represent groundwater samples that correspond to the soil profile (used for XAS). Stability is modeled at 6°C. Soluble Fe and As content are averages from nZVI groundwater samples (7.7 mg L ⁻¹ and 1857 mg L ⁻¹ , respectively). Concentration of S is an average of the whole study site (17 mg L ⁻¹ , from Cao et al. 2023. Diagrams made in Geochemist's Workbench vers. 18 (Bethke 2022).
Figure 37	. Fractional distribution of Fe species from XANES analyses, by depth in meters above sea level (MASL). LCF analysis conducted by Jon-Petter Gustafsson. 73
Figure 38	. Attachment rate (k) at varying flow speeds. Results are only shown for the second batch of column experiments
Figure 39	Breakthrough curves at varying flow speeds, both excluding blocking (a–d) and including blocking (e–h) . From top to bottom, flow speeds are: 1.34, 2.67, 3.52, and 5.50 mL min ⁻¹ . Open circles are experimental values and continuous lines are modeled values

Abbreviations

Abbreviation Description

AGW Artifical Groundwater

Al Aluminum As Arsenic

CCA Chromated copper arsenate
CFT Colloid filtration theory
DOC Dissolved organic carbon

Fe Iron

Fh Ferrihydrite

ICP-MS Inductively coupled plasma mass spectrometry

k First-order attachment rate constant $[T^{-1}]$

Kd Partitioning coefficient for metal mobility in soils

MTAs^V Monothioarsenate

mZVI Microscale zero valent iron nZVI Nanoscale zero valent iron

OM Organic matter
PAA Polyacrylic acid
PIM Protoimogolite

RH2000 Swedish national height system, 2000

ROI Radius of influence

S-mZVI Sulfidized Microscale Zero Valent Iron S-nZVI Sulfidized Nanoscale Zero Valent Iron

S_{max} Maximum solid-phase concentration of a colloid [M M⁻¹]

XAS X-ray absorption spectroscopy

XRF X-ray fluorescence ZVI Zero valent iron

1. Introduction

Arsenic (As) is the 20th most abundant element in the Earth's crust (most commonly found as arsenopyrite). As a result, there is a natural background of As in the atmosphere, groundwater, sediments, and soils. For example, one third of the atmospheric flux of As is of natural origin, mainly from volcanic activity (WHO 2001). In the groundwater, natural sources of As mainly stem from weathering and leaching from geological materials with As, drainage from thermal springs and geysers, and atmospheric deposition (NAS 1977). At the same time, As contamination, both in the atmosphere and groundwater, can also come from anthropogenic sources of As, such as mining, coal burning, agriculture, wood preservatives, waste material, and other industrial processes.

In terms of human health, As is a toxic metalloid that is primarily consumed through drinking water, rather than through food (Ng et al. 2003). High levels of As (>50μg L⁻¹) increase the risk of cardiovascular disease (Moon et al. 2012). They can also lead to dermatological effects, reproductive issues, immune system defects, cancer, and other serious human health concerns (World Health Organization 2001; Mohammed Abdul et al. 2015). Both Word Health Organization (WHO) guidelines and the European Union (EU) drinking water directive suggest a limit of 10 μg L⁻¹ As in drinking water. Between 94 and 220 million people worldwide are affected by toxic levels of As in the groundwater (Podgorski & Berg 2020). It is especially of concern in countries such as Argentina, Bangladesh, Chile, Pakistan, and the USA, where groundwater levels are naturally high in As due to As-rich bedrock (WHO 2001).

In Sweden, natural concentrations of As in groundwaters and surface waters are generally low, though ubiquitous (Lindau 1977), with the exception of areas with mining activity. The Bergslagen district in central Sweden, for example, has high levels of As from sulfide ores. Copper ores in northern Sweden are also a focal point of anthropogenic As contamination (Gustafsson et al. 2007). Recently, Sweden lowered its drinking water limit from $10~\mu g~L^{-1}$ to $5~\mu g~L^{-1}$, to be adopted in 2026 (Livsmedelsverket 2025).

An important anthropogenic source of As contamination is from wood impregnation plants. In Sweden, the historically most common wood preservative was chromated copper arsenate (CCA) (Augustsson et al. 2017). CCA is an inorganic, waterborne preservative that was a product used in Europe until 2004, when its use and marketing were both restricted by the EU, as metals released from the wood had serious health implications (EEC 2003). Additionally, As has been found on children's hands in playgrounds with CCA-treated wood, indicating that it is unsafe for commercial use (Kwon et al. 2004).

Typically, As exists in 4 valency states: -3, 0, +3, and +5, with arsenite (As(III)) and arsenate (As(V)) being the most common. Under anoxic conditions,

As(IIII) (H₃AsO₃ / H₂AsO₃⁻) dominates, whereas As(V) (H₃AsO₄⁻ / HAsO₄²-) is more prevalent in oxic ones. Additionally, As(III) is both more mobile (Gustafsson et al. 2007) and more toxic (WHO 2001) than As(V).

A partitioning coefficient (K_d) is often used to express mobility of metals in soils or aquifers. A low K_d value indicates low interaction between the solid phase and the particle, and therefore high mobility. K_d values vary widely with soil properties, but they are generally orders of magnitude lower for As(III) than As(V) (Cao et al. 2023). There is therefore often a higher risk of As leaching in reducing groundwater conditions, where As(III) is mostly present, compared to oxic conditions where As(V) dominates (Gustafsson et al. 2007).

Both in situ (e.g. phytoextraction, electrokinetic migration, and chemical immobilization) and ex situ (e.g. soil washing and solidification/stabilization) remediation methods have been used for As-contaminated soil. Chemical immobilization has proven to be very effective for high levels of As contamination; compared to other remediation techniques, it is also highly efficient and cost-effective (Liao et al. 2022). Recently, zero valent iron (ZVI) has become a popular focus of research as a promising chemical immobilization technique because it is cheap, efficient, non-toxic, and easy to produce. It has proved effective against many contaminants, including chlorinated organic compounds, heavy metals, and volatile organic compounds (Fu et al. 2014; Chen & Qian 2024). During lab experiments, it has also proven highly capable of immobilizing both As(V) in oxic conditions (Manning et al. 2002; Bang et al. 2005b; Kanel et al. 2006), and As(III) in anoxic ones (Lackovic et al. 2000; Kanel et al. 2005; Formentini et al. 2024). There are, however, only few documented studies that assess ZVI's impact on As in field conditions. Additionally, field studies that have examined ZVI remediation of As have mainly been in oxic environments (Otaegi & Cagigal 2017; Castaño et al. 2021). To the best of our knowledge, only one field study has been conducted on As remediation by ZVI in anoxic conditions (Wilkin et al. 2008).

ZVI used for soil remediation is produced commercially in different compositions and sizes and is often modified, either with organic surface coatings or by altering the ZVI core (e.g. with sulfidation), mainly to improve mobility during injection. Formentini et al. 2024 conducted batch tests to examine the impact of four different types of ZVI particles—nanoscale ZVI (nZVI), microscale ZVI (mZVI), sulfidated nZVI (S-nZVI), and sulfidated mZVI (S-mZVI)—on As(III) immobilization under anoxic conditions, using soil sampled from an anoxic aquifer in Hjältevad, Sweden. At this site, the soil was contaminated with As following a spill from a CCA tank. The laboratory study found that all ZVI materials were highly efficient in immobilizing As, with mZVI and nZVI being the most efficient. A follow-up column experiment (Nyström 2022) with the same products found comparable results. Here, mZVI and nZVI

were the most efficient at immobilizing As; S-nZVI was successful, but less efficient, and results for S-mZVI were inconclusive due to experimental uncertainties.

At Hjältevad, mZVI and nZVI were subsequently injected *in situ* at the original site to evaluate whether these results could be confirmed in the field (Berggren Kleja et al. 2024). Concentrations of As were monitored in the aquifer around and downstream of the injection sites for over two years, but monitoring wells showed a limited change in total As concentrations in the groundwater.

The primary aim of this study was to evaluate the suitability of ZVI for As immobilization in reducing aquifer conditions. The first objective aimed to understand why ZVI injections two years prior did not have a measurable impact on As concentrations in the groundwater at field scale despite promising results at lab scale. We hypothesized that aggregation around the injection wells was the main limiting factor, as low particle mobility would lead to low contact of ZVI with As, limiting its potential to immobilize As at detectable rates for the whole aquifer. In order to evaluate this hypothesis, while also testing alternative explanations for insufficient As immobilization in the field, groundwater and soil samples were taken to determine the radius of influence (ROI) of ZVI at the injection sites. Anoxic soil samples were also taken for solid-phase X-ray absorption spectroscopy (XAS), in order to compare lab-scale with field immobilization mechanisms. These results served to establish whether the inefficiency of the ZVI was due to poor binding between As and ZVI or poor mobility and field conditions. Based on field results, the second objective in this study aimed at examining if sulfidized mZVI (S-mZVI) would be a potentially more mobile alternative in this field compared to the previously injected ZVI's. S-ZVI has previously been found to have higher mobility than its unsulfidized counterparts due to its FeS coating. S-mZVI's mobility was studied through a series of column experiments and modeling (Šimunek et al. 2013). This study aids in understanding the transition from successful lab studies to field implementations. More importantly, the combination of both parts of this study provides crucial insights into the behavior of different forms of ZVI in field and lab conditions to maximize its potential for As remediation in anoxic sites.

2. Theoretical background

2.1 Arsenic

Arsenic is a redox-sensitive metalloid, so its speciation in both solution and solid phase is affected by pH and redox potential (Eh). Fig. 1 shows the Eh/pH stability diagram for As at room temperature (25°C). At the typical pH range of untreated soil pore waters (pH 4-9), As(III) and As(V) are present. As(III) is typically found under anoxic conditions as H₃AsO₃, and As(V) in oxic conditions as H₂AsO₄⁻ and HASO₄²⁻. Under particularly reducing conditions, As(II), As(I), and even As(0) can be present.

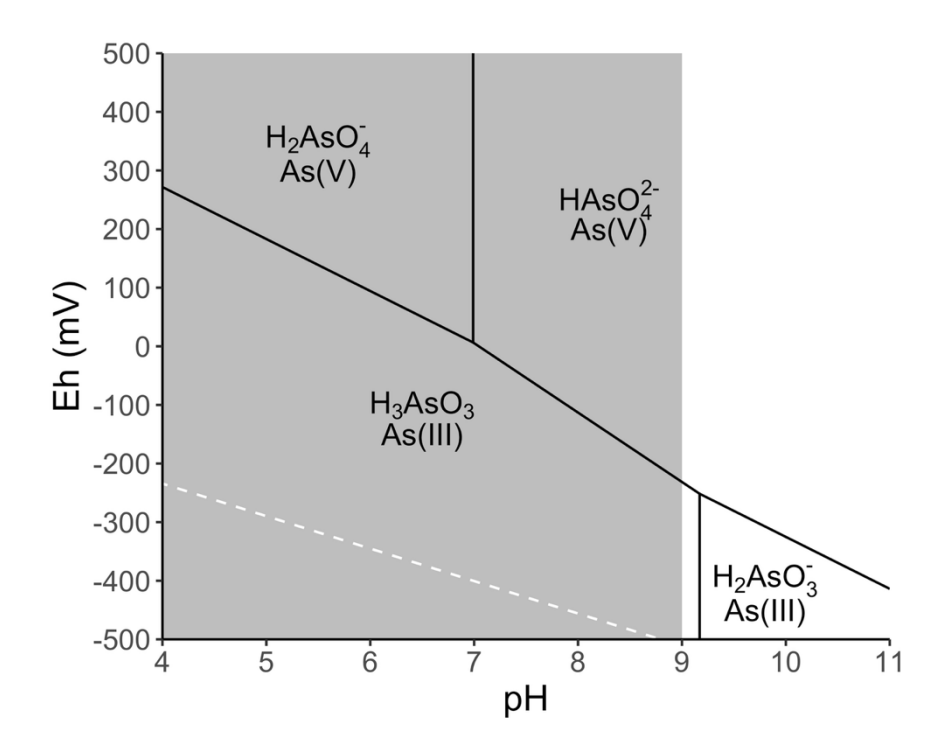


Figure 1. As stability diagram at 25°C for a typical pH and Eh range for groundwater. Stability lines were calculated using thermodynamic data from the database of Visual MINTEQ, vers. 3.1 (Gustafsson 2013). Gray shading shows the typical pH range for untreated pore waters.

As(V) has a generally high K_d value because it binds strongly to aluminum (Al) and iron (Fe) (hydr)oxides in soils. As(III), on the other hand, adsorbs more weakly to Al and Fe (hydr)oxides and other minerals in soils, resulting in lower K_d values and a higher mobility in soils. As(V), as well as more reduced forms of As, can be affected by presence of sulfide (S²-), which is often present in anoxic conditions when sulfate (SO₄²-) is reduced. Sulfide and As can react to form

soluble thioarsenite and thioarsenate complexes. Arsenite can also precipitate as As-S solid phases such as amorphous As₂S₃ (orpiment) or As₄S₄ (realgar) in high dissolved sulfide concentrations (Kocar et al. 2010). In the presence of high Fe concentrations, pyrite (FeS₂) can act as a sink for As under reducing conditions, forming arsenopyrite (FeAsS). In oxidizing conditions, these minerals dissolve; in these environments, therefore, an increase in Eh can cause a serious threat for As discharge into the environment. Mackinawite (FeS) can also immobilize As in reducing environments: during the initial stages of FeS formation, mackinawite is the first precipitate to form. It can then form both surface complexes and insoluble As sulfides (AsS) (Karimian et al. 2018).

2.2 Zero Valent Iron (ZVI)

All forms of ZVI affect groundwater conditions by raising the pH and lowering the Eh, creating more reducing conditions (Luna et al. 2015; Formentini et al. 2024). Under anoxic conditions, Fe(0), the ZVI core, is primarily corroded by water (Ponder et al. 2000; Farrell et al. 2001; Shi et al. 2015), raising the surrounding pH through the following reaction:

$$Fe(0)_{(s)} + 2H_2O \rightleftharpoons Fe^{2+} + H_{2(g)} + 2OH^-$$
 (1)

This reaction between ZVI and oxidants (here H₂O) creates a natural reductant demand, leading to the formation of Fe(II/III) (hydr)oxide precipitates (Shi et al. 2015). Final corrosion products include amorphous Fe(III) (hydr)oxides, magnetite (Fe₃O₄), maghemite (γ-Fe₂O₃), and lepidocrocite (γ-FeOOH) (Manning et al. 2002; Kanel et al. 2005), depending on redox and pH. Under particularly reducing conditions, mixed Fe(II/III) (hydr)oxide complexes such as green rust are formed as an intermediate stage to magnetite (Kumar et al. 2014) or lepidocrocite (Randall et al. 2000).

Two main mechanisms have been shown for As immobilization by ZVI. (1) As(III)/As(V) can be reduced to As(0) (Bang et al. 2005a; Yan et al. 2012; Tuček et al. 2017). At high ZVI concentrations, As—O bonds are broken, reducing As; the As then diffuses past the Fe oxide outer shell, forming an Fe—As intermetallic phase with the Fe(0) core (Yan et al. 2012). One study found an Fe(0) core with a double-shell structure: an inner region of exclusively As and an outer region of Fe(III) oxide. However, this product only occurred under acidic conditions and with pyrophoric oxidic-shell-free nZVI (OSF-nZVI) (Tuček et al. 2017). (2) An alternative reaction mechanism includes adsorption of As(V) and/or As(III) onto ZVI's corrosion products (Su & Puls 2001; Manning et al. 2002; Kanel et al. 2005; Lien & Wilkin 2005). For example, one study found that goethite and lepidocrocite adsorb As(III) without oxidation; hematite and magnetite adsorb As(III) weakly, and maghemite both adsorbs and oxidizes

arsenite. Despite varying binding strengths, As adsorbed to all corrosion products as inner-sphere, bidentate As(III) and As(V) complexes, with mixed As(III)/As(V) speciation found in the ZVI (Manning et al. 2002). Fe(III) can oxidize As(III) to As(V) via:

$$2Fe(OH)_3 + 3H^+ + As(OH)_3^0 \rightleftharpoons 2Fe^{2+} + 5H_2O + H_2AsO_4^-$$
 (2)

Other literature has confirmed the adsorption of As(V) to ZVI through innersphere complexes (Kanel et al. 2005; Wu et al. 2018). Co-precipitation of As(V) or As(III) with corrosion products resulting in physical occlusion of As can also be a factor in As immobilization (Lien & Wilkin 2005; Wu et al. 2018).

Singh et al. 2021 give a detailed explanation for As(III) and As(V) complexes with ZVI and its corrosion products (Fig. 2). One path for both As(III) and As(V) is adsorption onto the Fe(0) core as a reduced form of an As-Fe intermetallic structure with undefined valence state (in the figure termed "As(0)"). Otherwise, As(V) could form complexes with the Fe oxide outer shell. As(III) could form similar complexes, either directly as As(III) or as the oxidized As(V). In both cases, the As(V) could then be reduced back to As(III) to form inner-sphere complexes with the Fe oxide layer. Finally, Fe(II)/Fe(III) corrosion products coprecipitate with As(III) to form Fe-As (hydr)oxides.

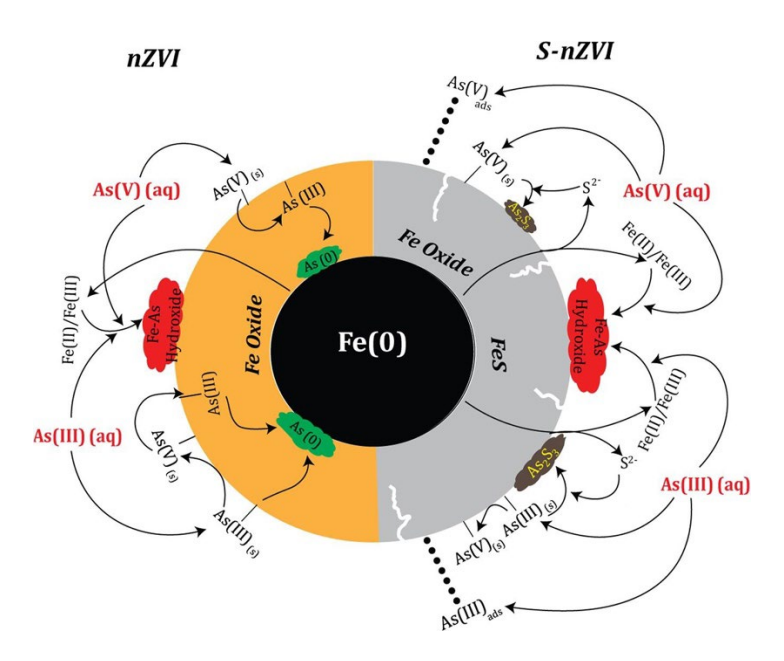


Figure 2. Immobilization mechanisms for As(III) and As(V) by nZVI (left) and S-nZVI (right). Figure from Singh et al. 2021.

The previous mechanisms were observed in aqueous suspensions of ZVI, where As salts were added. Formentini et al. 2024, however, used sediments, closer simulating field conditions. They found that As(III) removal by ZVI under

anoxic conditions was driven by the increase in pH resulting from ZVI corrosion: due to the pH increase, As(III) was first oxidized to As(V) (Fig. 1) and then bound to Fe (hydr)oxides. Reduction to As(0) by the metallic core could not be confirmed.

The size of ZVI has an impact on the extent and speed for binding As. Owing to its higher specific surface area, nZVI can work in minutes and is about 1000 times faster at binding As than mZVI (Kanel et al. 2005). It also corrodes faster – Formentini et al. 2024 found that only 4% of nZVI remained uncorroded after 30 days, compared to 36% for mZVI. However, both sizes showed similar effectiveness at adsorbing As.

As ZVI slowly corrodes over time, the increased quantity of Fe (hydr)oxide products leads to increased As binding (Kanel et al. 2005). Corrosion speed is therefore relevant: although, in Formentini et al. 2024, mZVI and nZVI showed similar effectiveness in As immobilization after 30 days, the slower corrosion of mZVI could lead to higher total sorption on a long-term scale if pH increase is the primary driver in As adsorption. Indeed, a review paper found that mZVI is generally more effective at contaminant remediation than nZVI, likely because nZVI is more reactive and thus cannot maintain an increased pH over an extended period of time (Comba et al. 2011). However, if adsorption, and not pH change, is the dominating immobilization process, a faster corrosion speed should lead to more effective results, as the fast creation of oxidation products can more quickly adsorb As.

Sorption is also pH-dependent. The point of zero charge (pH_{PZC}) of ZVI corrosion products ranges from about 6-9 (e.g. the pH_{PZC} of magnetite is 6.5 and of hematite is 7) (Kosmulski 2004). As(V) is negatively charged across pH's (as H₂AsO₄⁻ and HAsO₄²-) (Fig. 1), making it more pH-dependent: above the pH_{PZC} of the respective Fe product, the negative charges of As and Fe repel each other, resulting in weaker-sorbed As. Below the pH_{PZC}, however, As(V) sorbs strongly from electrostatic attraction. As(III) is less pH-dependent, but sorption is weaker. Up to pH 9.2 (at 25°C), the dominant form As(III) is H₃AsO₃⁰ (Fig. 1)—there is no electrostatic attraction with Fe oxides. Above pH 9.2, As(III) exists as H₂AsO₃⁻. At that point, ZVI corrosion products are typically also negatively charged, and the two ions repel each other at the surface (Fig. 3).

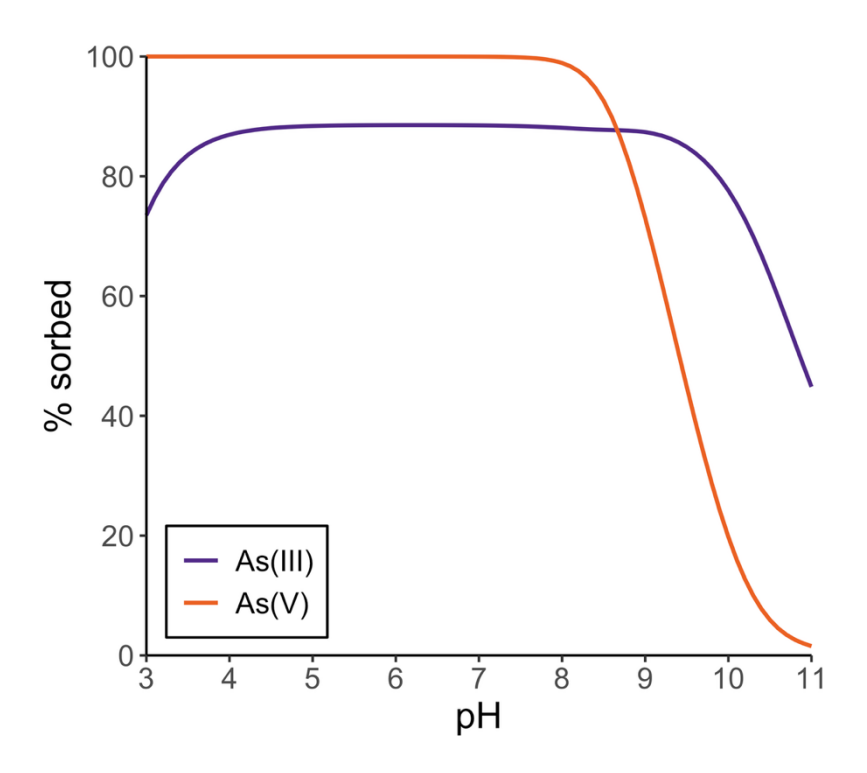


Figure 3. Effect of pH on As(III) and As(V) sorption to ferrihydrite. Model made with Visual MINTEQ ver 4.0 (Gustafsson 2013). Inputs are 10 μ M As(III), 10 μ M As(V), and 0.03 g L^{-1} hydrous ferric oxide (ferrihdyrite). Values for inputs are from Dixit & Hering 2003.

2.3 Sulfidated Zero-Valent Iron (S-ZVI)

Ideally, S-ZVI should have an Fe(0) core covered by an FeS shell to optimize its physico-chemical properties; however, this structure has not yet been achieved in a lab. Instead, the shell is typically a mixture of Fe oxides and FeS. Sulfur (S) speciation on the shell also depends on the creation process (one-pot or two-step method). With the one-pot method, S2²⁻, Sn²⁻, S⁰, and SO3²⁻/SO4²⁻ have all been found as surface groups on S-nZVI shells. In the two-step method, only FeS (or, with high degrees of sulfidation, FeS₂ as well) is found on the surface (Su et al. 2019). Although the two-step method does not create extraneous surface groups, the FeS is less uniformly distributed compared to the one-pot method (Fan et al. 2013; Su et al. 2015). S-ZVI's mobility depends on the FeS coating, so the extraneous surface groups in the one-pot method and the uneven distribution of FeS in the two-step method can both have negative impacts on S-ZVI's distribution.

Regardless of the synthesis method, S-nZVI is characterized by having larger flake-like structures than unaltered nZVI. Where nZVI has a core-shelled structure with an inner core and an outer smooth shell, S-nZVI shows that same spherical core-shelled structure, but with a flaky outer shell (Singh et al. 2021).

This flake-like structure has been shown to increase the number of binding sites for S-ZVI, augmenting its removal capacity compared to ZVI (Wu et al. 2018).

The S/Fe molar ratio of the coating has an effect on surface roughness and removal capacity. A higher S/Fe ratio leads to more FeS precipitates, which in turn causes higher surface roughness/flakiness and more As removal (Wu et al. 2018; Singh et al. 2021). However, there is an optimal S/Fe ratio for As immobilization. FeS is more hydrophobic than other Fe (oxyhydr)oxides; when the Fe/S ratio is too high, the increased S/Fe ratio causes a level of hydrophobicity that ultimately decreases the interactions between S-ZVI and hydrophilic As(III) under anoxic conditions, despite higher levels of flakiness (Zhao et al. 2021).

S-nZVI has been found to be very effective for As immobilization during laboratory experiments in both oxic and anoxic conditions (Wu et al. 2018; Singh et al. 2021). This effectiveness was linked to S-nZVI's slower corrosion rate compared to pristine nZVI, leading to a longer reactivity period that sustains reducing conditions and high pH (Singh et al. 2021). On the other hand, the coating can be a drawback for As immobilization: Formentini et al. 2024 found that S-nZVI was 10 times less effective than nZVI at immobilizing As(III), likely because the FeS coating was mostly insoluble, excessively hindering corrosion and therefore limiting As binding sites during the 30-day test period. A balance, therefore, is needed for corrosion speed, where corrosion occurs fast enough to create available binding sites, but slow enough to maintain favorable groundwater conditions for As immobilization over time.

There is significant variation in the literature discussing the dominating process for As immobilization by S-nZVI. The immobilization method is important as it dictates the strength (and reversibility) of As removal from the groundwater. Outer-sphere adsorption, for example, involves electrostatic attraction, an adsorption method which is quite weak compared to the covalent bonds involved in inner-sphere adsorption. Overall, co-precipitation (of AsFeS) (Wu et al. 2018; Zhao et al. 2021), surface precipitation (of As₂S₃) (Singh et al. 2021), and formation of As sulfides (Zhao et al. 2021) seem to be the dominating processes for As removal. Inner-sphere (Wu et al. 2018) and outer-sphere (Singh et al. 2021) complexes, however, also play a role.

In addition to As immobilization by nZVI (section 2.2), Fig. 2 depicts mechanisms of S-nZVI for As adsorption (Singh et al. 2021). Both As(III) and As(V) formed outer-sphere complexes directly onto the FeS surface, either directly in their original speciation or, for As(III), as oxidized As(V). Both species also reacted readily with S²⁻ from the FeS surface, creating As₂S₃ surface precipitates, although As(III) formed more of these precipitates than As(V). The presence of S, therefore, is an important factor in As immobilization by S-nZVI. On top of the two dominating processes, partially oxidized As(III) to As(V) could also react with Fe(III), an intermediate phase from the adsorption of Fe(II) on the

Fe (hydr)oxides that are present in the outer shell, forming Fe-As (hydr)oxide precipitates.

Adsorption of As on S-ZVI is pH-dependent. As with As adsorption onto soil minerals, the effect of a change in pH differs somewhat between As(V) and As(III). The pH_{PZC} of S-nZVI is about 8.3 (Lv et al. 2019), but the Isoelectric Point (IEP) varies significantly between studies, from 4.2 to 7, possibly due to different degrees of sulfidation and/or working conditions (e.g. ionic strength) (Su et al. 2019). As discussed in section 2.2, As(V) primarily exists as an anion regardless of pH, leading to repulsion with negatively charged S-ZVI above the respective pH_{PZC} and a resulting sharp drop in adsorption rate after this point (Singh et al. 2021). At a more acidic pH, however, S-ZVI is effective at adsorbing As(V). As(III) is neutrally charged below pH 9.2 (25°C); above that point, it becomes negatively charged and also repels the S-ZVI surface, decreasing S-ZVI's immobilization effectiveness (Fig. 1).

2.4 ZVI and particle mobility

ZVI transport in soils is controlled by various chemical and physical factors: particle-specific properties (e.g. size, shape, chemical composition, surface charge, and surface coating); physical properties of the aquifer (e.g. texture and particle distribution); the resulting particle-media interactions; groundwater composition (e.g. ionic strength, pH, and dissolved organic matter content), and ZVI injection conditions (e.g. concentration, flow rate, and viscosity) (Petosa et al. 2010; Shi et al. 2015; Berggren Kleja et al. 2024).

Most field studies have found that nZVI distributes effectively in the field (He et al. 2010; Wei et al. 2010; Kocur et al. 2014; Köber et al. 2014). However, these studies relied heavily on indirect measurements (e.g. decrease in oxidation/reduction potential or change in pH), only observed nZVI at less than 2 m from the injection well, and showed generally nonuniform nZVI distribution (Johnson et al. 2013). In a study that controlled for these factors, nZVI was found to distribute very poorly, making it an ineffective remediation method (Johnson et al. 2013).

Much fewer field studies have been conducted on mZVI, but they have found that mZVI distributed effectively in the field, although all contained some sort of modification to improve mobility (Truex et al. 2011; Luna et al. 2015).

Particle transport in soils, including ZVI, is strongly dictated by the relation between particle and pore size. Pore sizes are categorized into micropores (<2 nm in diameter) and macropores (>50 nm in diameter) (IUPAC 2003). Generally, ZVI size has a strong effect on particle mobility. For example, mZVI particles are ~1 µm or larger, restricting their movement in micropores. In more clayey soils, where macropores are common, mZVI transport tends to be restricted to these macropores. In sandy soils, where natural macropores are few, mZVI transport

tends to follow preferential flow paths created during high-pressure injection of ZVI. Therefore, nZVI is expected to have higher mobility than mZVI, as its smaller size leads to more unrestricted mobility. Additionally, mZVI can have mobility issues due to physical filtering, or straining, and sedimentation (Gastone et al. 2014; Luna et al. 2015), although nZVI is also subject to colloidal interactions between the particles themselves as well as between nZVI and pore surfaces (Su et al. 2019).

Transport and immobilization of a particle in soil or sediment can either follow favorable or unfavorable attachment. The interaction of two particles is termed aggregation, while homoaggregation is the interaction of like particles.

Attachment is the interaction between particles and immobile particle surfaces, also referred to as collectors. Under unfavorable attachment, particles, or particle and collector, have like charges, leading to electric double layer interactions that create an energy barrier to attachment, preventing attachment and aggregation. With favorable attachment, the colloid and collector have opposite charges, creating an electrostatic attractive force. Unfavorable attachment is most common in nature, as most particles and collectors are negatively charged at typical groundwater pH. However, favorable attachment can occur when there is especially low pH, high ionic strength, or presence of minerals that are positively charged at neutral or near-neutral pH (e.g. titanium oxide, iron oxide, magnesium oxide, or magnesium calcite) (Elimelech et al. 2013).

While smaller particle size can lead to more mobility, it can also increase the particle's interactions with colloid surfaces in the soil. Specifically, nZVI can have low mobility (Schrick et al. 2004; Ahn et al. 2021) owing to deposition onto aquifer solids, aggregating and settling from Van der Waals forces, electric double layer interactions, and magnetic attractive forces (Su et al. 2019). The primary driving force behind low mobility in nZVI is magnetic attractive forces leading to homoaggregation (Phenrat et al. 2007; Dalla Vecchia et al. 2009; Ahn et al. 2021). When nZVI is pumped into groundwater, particles initially form micrometer-sized aggregates in the presence of groundwater ions (Ahn et al. 2021); the aggregates then link into chains ("gelation") (Phenrat et al. 2007).

Magnetic attractive forces are hard to overcome. In order to increase nZVI's transport distance during injection, a strong, long-range, steric repulsive force is necessary to prevent particle aggregation. If the particles are experiencing a simple head-to-dipole interaction, adding a biodegradable polymer will create a brush layer that causes steric repulsion, and therefore less aggregation (Dalla Vecchia et al. 2009). The polymer should be biodegradable so that it reduces aggregation during injection but does not inhibit contaminant immobilization over time. One such biodegradable polymer is polyacrylic acid (PAA). PAA adds a negative charge to the particles, increasing electrostatic repulsion between the particles themselves and between the nZVI particles and the soil (Hydutsky et al.

2007), reducing the sticking coefficient of nZVI (Schrick et al. 2004). Guar gum can also be added to increase transport distances. Guar gum, if added in high quantities, increases viscosity of the solution, slowing down sedimentation, and therefore aggregation, of the particles (Tiraferri et al. 2008). Previous studies have shown guar gum to be effective at dispersing both mZVI (Luna et al. 2015) and nZVI (Tiraferri et al. 2008). The addition of guar gum reduces the hydrodynamic radius of bare nZVI particles from 500 nm to less than 200 nm, preventing nZVI aggregation even at high salt concentrations (Tiraferri et al. 2008).

Sulfidation of the ZVI particles themselves can also increase ZVI mobility: compared to unaltered ZVI, S-ZVI has been shown to have higher mobility (Song et al. 2017; Gong et al. 2020). S-nZVI does not show the usual nano-chain structure from van der Waals forces, electric double layer interactions, and magnetic attractive forces present in unaltered nZVI because of S-nZVI's FeS coating, thereby inhibiting aggregation and sedimentation (Song et al. 2017). S-ZVI's mobility could also be a result of S-ZVI's pH_{PZC}/IEP, although the IEP varies significantly between studies, as mentioned earlier. If the S-ZVI in question is negatively charged at the groundwater pH, this negative charge both creates electrostatic repulsion with the collector and improves the colloidal stability of ZVI (Su et al. 2020).

Besides particle properties and environmental factors, there are also injection characteristics that can influence ZVI mobility, as discussed below.

2.5 Colloid Filtration Theory (CFT)

Colloid filtration theory (CFT) is a concept for predicting colloid-collector interactions. In CFT, surface attachment kinetics are described by a single, irreversible first-order process using the equation:

$$\frac{dC_p}{dt} = -k \cdot C_p \tag{3}$$

 C_p is the concentration of particles in the pores, and k [T⁻¹] is the first-order attachment rate constant, where:

$$k = \alpha \cdot \beta \tag{4}$$

 α [-] is the attachment efficiency, or the probability that particles that reach the collector adhere. β [T⁻¹] is a measure of the physical processes that bring particles close to the collector surface, such as diffusion, convection, and sedimentation. α is a function of the surface forces acting between the particle and collector: electrostatic double layer repulsion and van der Waals forces. It is therefore affected by charge (favorable/unfavorable attachment). Overall, a low α , and thus

a low k, indicates a slow interaction of the particle with collector surfaces, and therefore high particle mobility.

CFT is an apt concept for particles that attach irreversibly to the collector. The interaction between nZVI and porous media is likely through a practically irreversible attachment (Phenrat et al. 2019), a process that can be accurately described by CFT. A previous study that performed column experiments and modeling, in Hydrus-1D, of nZVI particles in Hjältevad soil found a positive relationship between flow rate and k, a correlation which suggests that colloid-collector interactions between these materials were irreversible (Berggren Kleja et al. 2024). These findings further support the use of CFT for nZVI mobility studies.

As attachment rate increased with flow speed, these results also indicate a lower ROI with higher injection speed. Subsequent modeling applied the column results in field conditions using a 1D radial flow model in the software MNM (Bianco et al. 2018). MNM can account for more complicated measurements than Hydrus-1D, such as colloidal aggregation, colloidal deposition, and nanoparticle diameter. These results, contrary to previous findings, found that injection speed in the field has a minor impact on mobility (Berggren Kleja et al. 2024).

According to CFT, an increased injection concentration should increase particle-collector contact, thereby leading to an increased attachment of particles to the collector. At the same time, CFT does not account for other important factors caused by increased particle concentration, such as higher particle-particle interactions that lead to aggregation and clogged pores (Phenrat et al. 2007; Ersenkal et al. 2011; Ahn et al. 2021). Adding aggregation as a factor significantly complicates the modeling and is beyond the scope of this study.

3. Site description and previous findings

3.1 Overview

The contaminated site is a former wood impregnation plant in Hjältevad, Eksjö Municipality, Sweden. It is 5.3 ha and surrounded primarily by residential housing and forest. Lake Hjälten and the river Brusaån are about 300 m north of the site. The river flows from the lake from west to northeast. The site is composed of granite bedrock at 18–38 m depth, covered by glaciofluvial deposits that have gradually built up in layers of sand, gravel, and silt. Soil texture is dominated by sand at all depths, with coarse sand on the surface and fine sand increasing with depth, especially below the groundwater surface. Silt also increases with depth, until a maximum of about 10% (Sweco 2019). Hydraulic conductivity (K) ranges from 4 m d⁻¹ near the ground surface to 80 m d⁻¹ at around 18 m depth, following decreasing grain size with depth (Cao et al. 2023). There is a shallow, unconfined aquifer within the glaciofluvial deposits.

The average groundwater depth is 3 m, or 165 MASL (RH2000). Groundwater levels have been steady for the last few years, although there was a spike in November 2021 with groundwater levels 25–30 cm higher than average (Sweco 2025). The groundwater flow is northwestern and is naturally drained by the nearby Brusaån River. The average hydraulic gradient is 0.16% (Cao et al. 2023).

According to data from monitoring wells between 2017 and 2021, pH in the untreated aquifer ranges from 5.7 to 7.3 (average of 6.4). The Eh varies from -270 to 264 mV, differing both spatially and temporally. Anoxic conditions, however, dominate, as a result of high dissolved organic matter content from the surrounding forest. The dissolved organic carbon concentration (DOC) is between 2.0 and 3.6 mg L⁻¹ (average of 2.8 mg L⁻¹) (Cao et al. 2023).

The climate is warm and temperate overall. The average annual temperature in the area between 1991 and 2020 was 6.3°C, and the average annual precipitation was 700 mm (Swedish Meterological and Hydrological Institute [SMHI]).

3.2 History of arsenic contamination

The wood impregnation plant operated from 1949–1985 and applied CCA as an impregnation product. This plant used Boliden K33 CCA, composed of 24.0% As₂O₅, 26.6% CrO₃, 14.8% CuO, and 24.6% water.

In August 1968, a 50 m³ tank of CCA found on the site leaked into the groundwater. The leakage was caused by corrosion that had created a 70–80 cm hole above the bottom of the tank. Around 15–18 m³ of CCA leaked, corresponding to 65–80 kg of As. However, it was later found that previous drips and spills also contributed to As contamination, although these primarily affected

upper soil layers while the leak affected deeper ones. An estimated total of 2–3 tons of As leaked from the tank over the years.

"Pump and treat" began a couple weeks after the leak was discovered. Pumping continued consistently until December 1968, then off and on between 1985 and 1993.

In 1997, the soil was further treated with soil washing. The surface soil was excavated in 0.1 m layers until As concentrations were <40 mg kg⁻¹. Around the storage tank, this corresponded to a depth of 10 m and an area of 800 m². A total of 26,600 tons of soil were treated (1.2 tons As). Soil with As >40 mg kg⁻¹ was treated off-site at a soil washing plant, and the deep excavated zone was then backfilled with uncontaminated and treated soil. This filling led to the creation of a hill 5–7 m tall on top of the contamination source zone. A map of the site can be found in Fig. 4 and a side profile of the mound in Fig. 5.

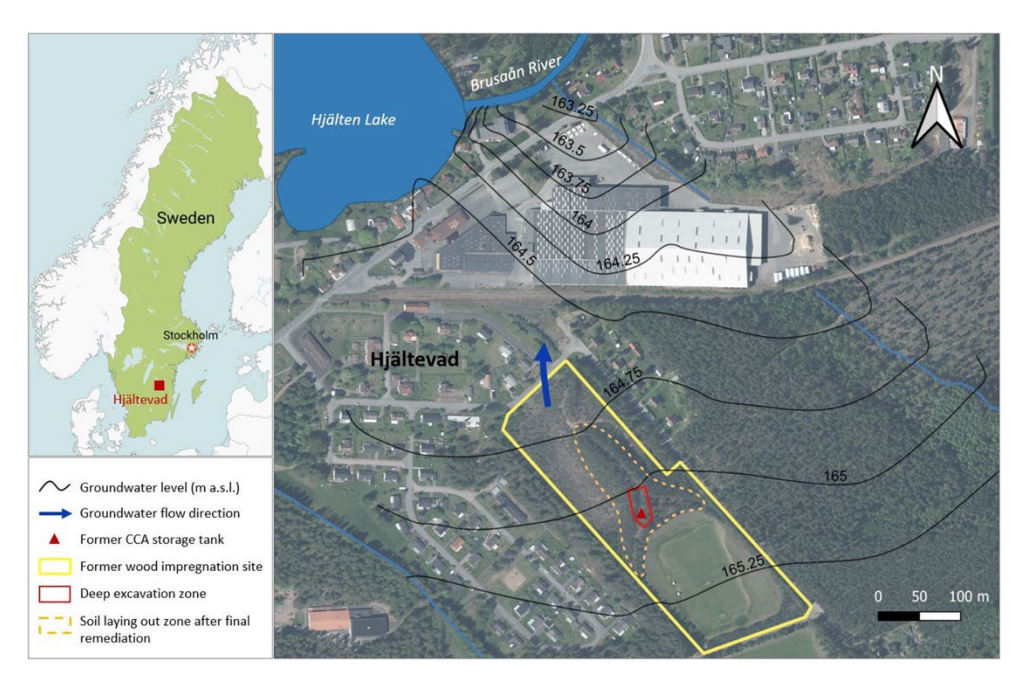


Figure 4. Overview map of the contaminated site. Figure from Cao et al. 2023.

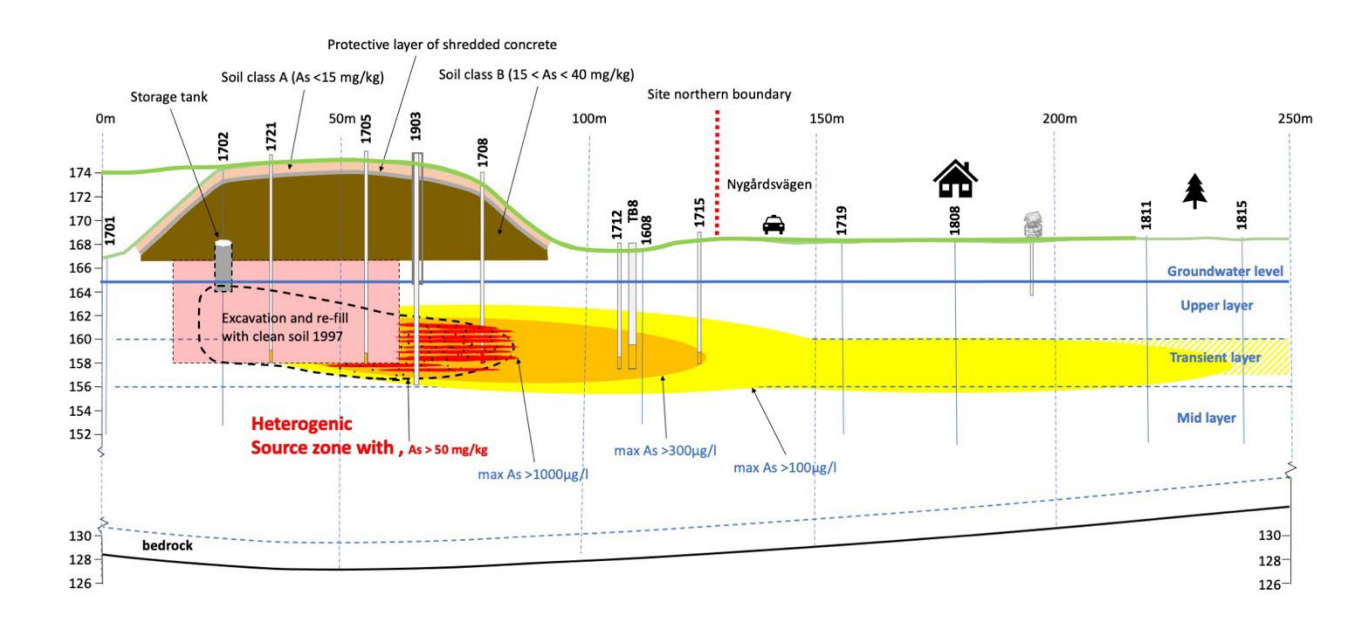


Figure 5. Side profile of the injection zone and contamination plume, SSE-NNW. Double-verticle lines indicate groundwater wells, and singular lines represent dynamic groundwater sampling conducted right before mZVI and nZVI injection. Figure by Sweco for Berggren Kleja et al. 2024.

3.3 State of arsenic pollution

Despite efforts to remediate the area, As levels have continued to rise. In TB8, a monitoring well 90 m downstream of the original CCA tank, an annual increase in dissolved As concentrations of 30 $\mu g \, L^{-1}$ was measured, with annual variations of up to 25% (100 $\mu g \, L^{-1}$) (Fig. 11b). Dissolved As concentrations peaked at 700 $\mu g \, L^{-1}$ in 2023. The current pollution plume, where As is >10 $\mu g \, L^{-1}$, is 20,000 m². Modeling with MODFLOW GMS (Harbaugh 2005) shows that it continues to spread at a rate of 0.7 m year⁻¹. This spread is faster at shallow layers, consistent with grain size distribution (Cao et al. 2023).

The highest levels of dissolved As have been detected between 162.5–153.5 MASL, with the highest levels at 157.5 MASL (the depth of the deep excavation). Shallower zones (above 162.5 MASL) and lower zones (below 153.5 MASL) have low concentrations (<10 µg L⁻¹). Total As at 160.5–153.5 MASL ranges from 143 to 1450 µg L⁻¹ (average 593 µg L⁻¹). Owing to anoxic conditions, As(III) dominates over As(V), representing 91% of total As. The partitioning coefficient of As in groundwater (GW) (K_{d(GW)}) values vary spatially and temporally, but are overall low (between 1 and 107 L kg⁻¹), as expected based on the dominance of As(III) (Cao et al. 2023).

3.4 ZVI injection: previous pilot study

In Autumn 2022, before this study, mZVI and nZVI were injected at two locations on the contaminated site. Before ZVI injections took place, dynamic groundwater sampling near the injection points was conducted with a geoprobe, at 1 m depth increments, to determine existing groundwater conditions. The pH and Eh were measured in the field with a flow cell. Samples were then passed through $0.45~\mu m$ filters before analyzing metal concentrations with inductively coupled plasma mass spectrometry (ICP-MS).

Injections of mZVI and nZVI all occured below the groundwater table. Both mZVI and nZVI were injected with bottom-up direct push injection (DPI) using a 2.21" Geoprobe retractable single-port injection tip over a total depth range of 160.8–154.5 MASL for mZVI and 161–154.2 MASL for nZVI, although exact ranges varied by injection point (Fig. 6, Fig. 7). Compared to other injection techniques, DPI should minimize soil alteration and lead to more permeability by minimizing air bubbles and clay mixing (Comba et al. 2011).

The mZVI injected, commercially available as Ferox Target®, arrived in powder form from Hepure Technologies (USA). It contains 95% Fe(0), 1.5–2.0% carbon, 1.0–1.5% silicon, and 0.1% sulfur and phosphorus. Its nominal particle diameter is 44 µm. An ROI test was conducted with 550 g L⁻¹ mZVI and 5 g L⁻¹ guar gum, and showed a heterogeneous dispersion, with a change in conductivity and color occurring only at 157 MASL. The north and south directions showed limited spread in the upper soil layers (161.5–157.5 MASL), and only a spread to 0.5 m in the eastern direction. Injection was then conducted at 5 injection points with 300 g L⁻¹ mZVI and the same amount of guar gum, to be consistent with typical mZVI injection concentrations. A larger injection volume than the ROI test was used to compensate for low mobility.

For nZVI, NANOFER STAR, a powder form of nZVI manufactured by NANOIRON (Czech Republic) was used. It consists of 65–80% Fe(0) and 35–20% iron oxide (Fe₃O₄). Its average particle size is 59.8 ± 1.3 nm. This product is stabilized with a thin iron oxide layer, preventing reactivity when in contact with air—the particles are "activated" when mixed into an aqueous suspension. The nZVI powder was mixed with water and combined with PAA for increased mobility: final concentrations were 5 g L⁻¹ nZVI and 0.75 g L⁻¹ PAA, in accordance with typical nZVI injections (Geosyntec 2022). Before injection, an ROI test was performed and resulted in an ROI of 0.6 m from the injection point.

A map of the injection points can be found in Fig. 6 for mZVI and Fig. 7 for nZVI.

A detailed explanation of the injection can be found in Berggren Kleja et al. 2024.

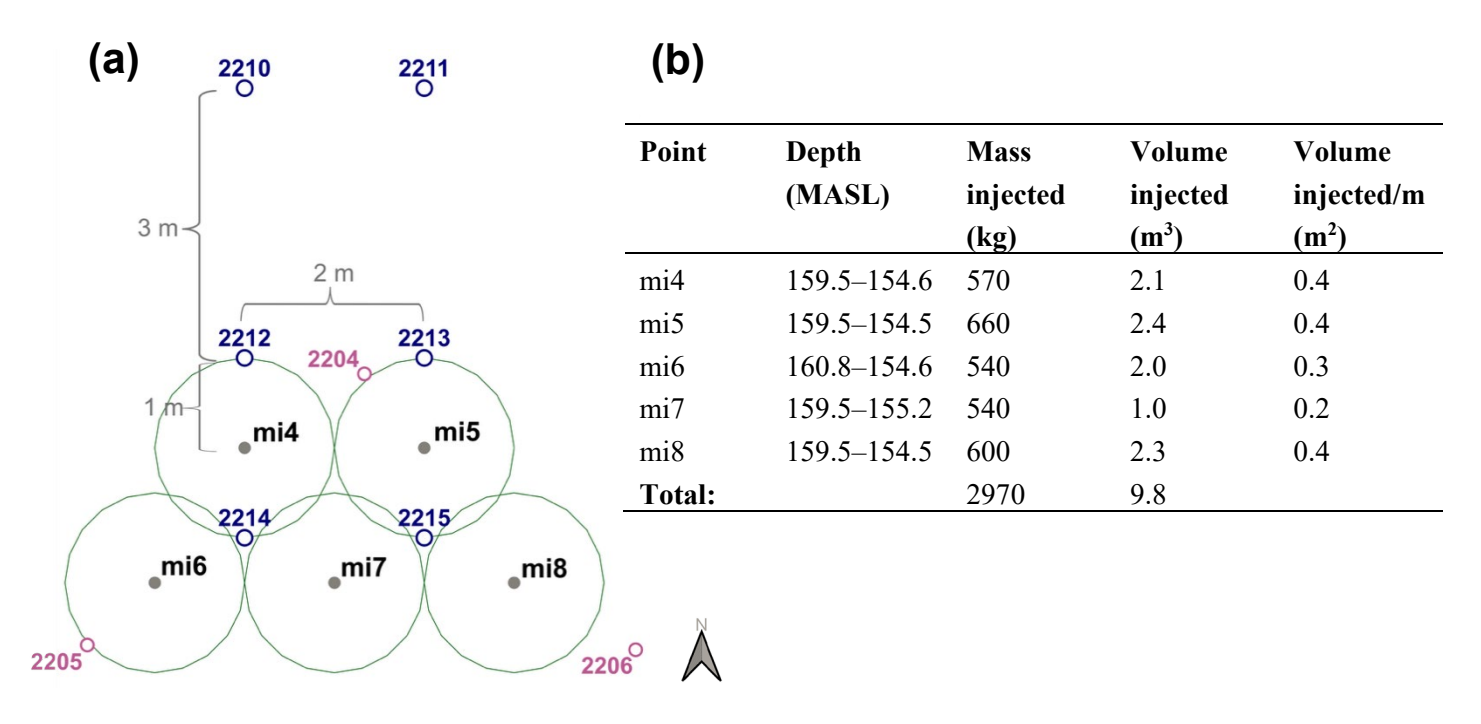


Figure 6. Injection points for mZVI and nearby wells used for short-term monitoring. Figure (a) shows a map of the injection points, and (b) displays injection depths (bottomup) and other injection data. Data from Berggren Kleja et al. 2024.

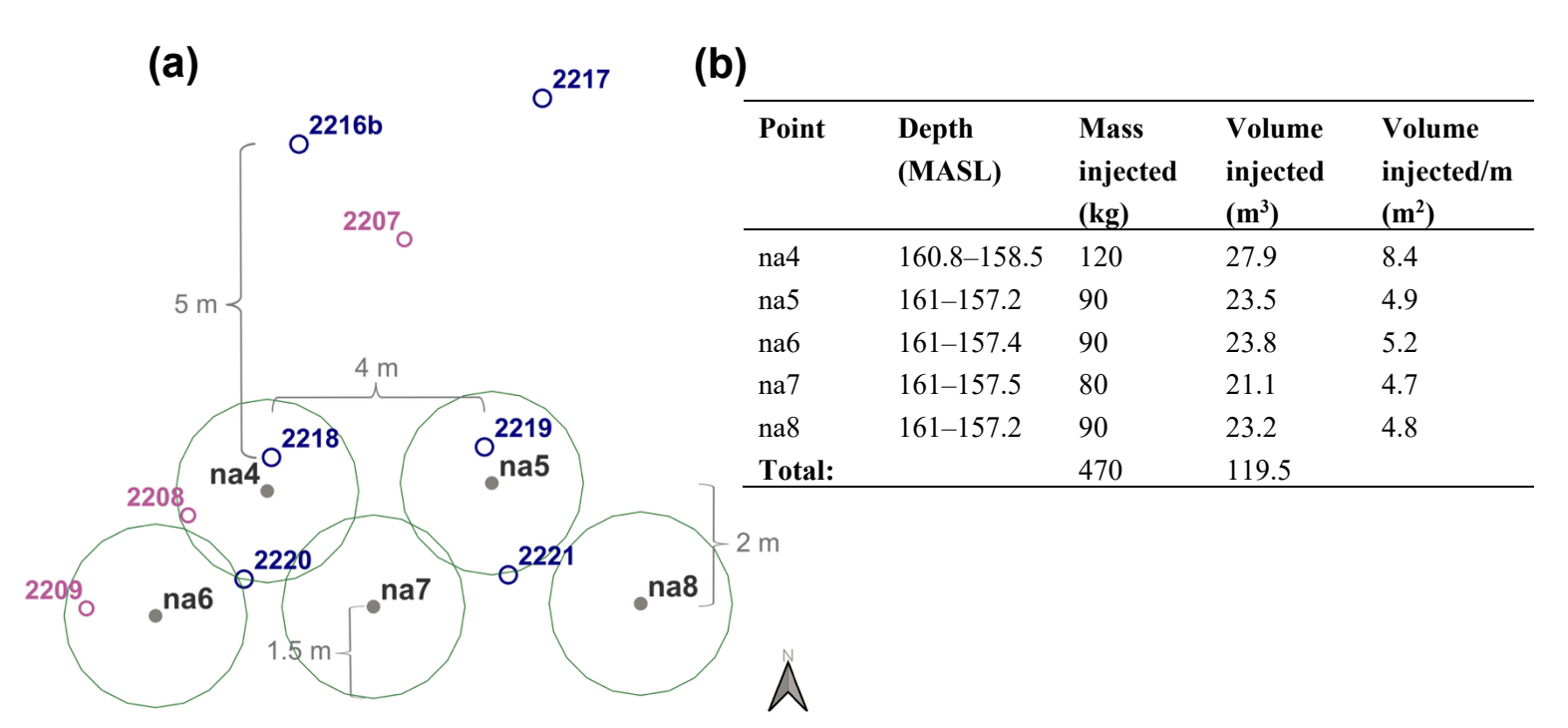


Figure 7. Injection points for nZVI and nearby wells used for short-term monitoring. Figure (a) shows a map of the injection points, and (b) displays injection depths and other injection data. All points were injected bottom-up except na7, which was injected top-down. Data from Berggren Kleja et al. 2024.

3.5 Initial findings

3.5.1 Batch tests and column experiments

As mentioned previously, Formentini et al. 2024 conducted batch tests studying the effectiveness of nZVI, mZVI, S-nZVI, and S-mZVI for adsorbing As(III) in anoxic conditions. The batch tests involved continuous shaking of a mixture of artificial groundwater (AGW), As-contaminated sediment from the Hjältevad study site, and the respective ZVI. In phase A, samples were shaken for 30 days. In phase B, the pH was subsequently adjusted to 7 to simulate a long-term system where the pH of groundwater would return to pre-injection values. The second phase also allowed isolation of phase A, in order to study the direct effect of pH change on As immobilization. Phase B samples were shaken in pairs for another 7, 14, and 35 days. S-mZVI had no effect on pH, so it was only studied in phase A.

The AGW was at pH 6 before ZVI addition. In the control, with no ZVI, pH drifted during equilibration, from 6.5 to 7.3, and Eh was consistent at around 0 mV. At the end of phase A, mZVI and nZVI had both increased the pH to 9.4 and 9.8, respectively, and decreased the Eh to below -200 mV. S-mZVI had little effect on pH (it stayed at around 7.3), but did decrease the Eh slightly to -100 mV. S-nZVI increased the pH to 9.3 and lowered the Eh to -200 mV. The As speciation based on these Eh/pH values is found in Fig. 8. All forms of ZVI were effective at immobilizing As. Additionally, the study found that all forms of ZVI remained, to some extent, unoxidized at the end of 30 days; S-mZVI oxidized the least and nZVI the most (Table 1).

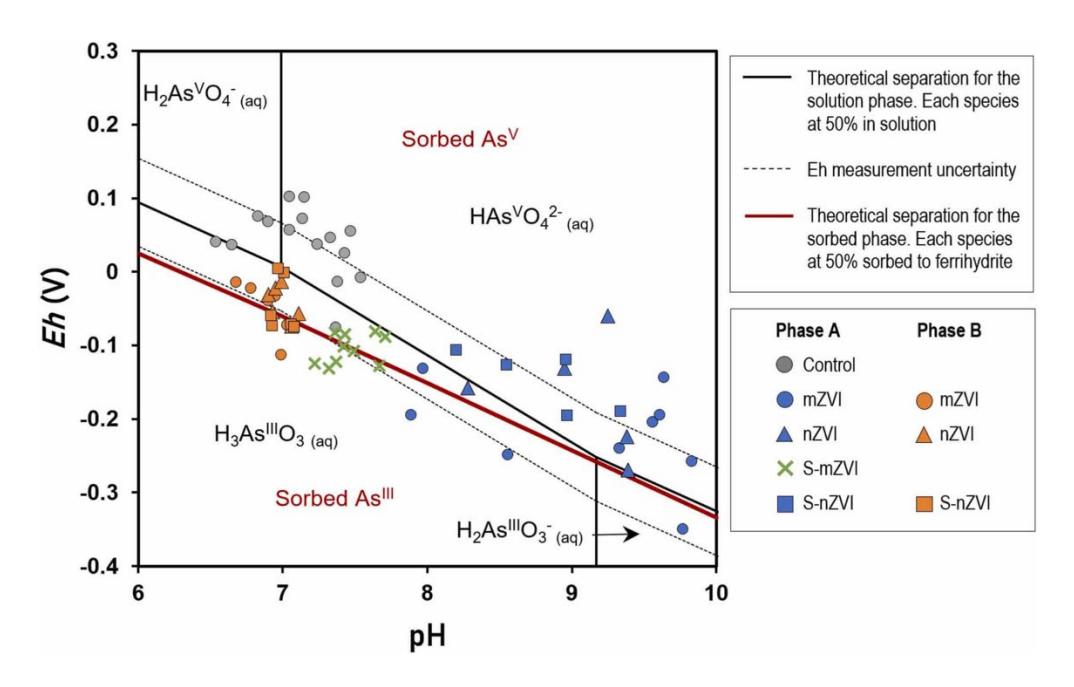


Figure 8. Stability diagram for sorbed-phase (red line) and solution-phase (black lines) As(III) and As(V), overalyed with Eh/pH of water conditions from batch tests after Phase A (uncontrolled pH) and B (pH 7). From Formentini et al. 2024.

Table 1. Total As and Fe(0) remaining in solution after phases A and B of batch tests. Data from Formentini et al. 2024.

Treatment	Phase A			Phase B	
	$As_{(total)}$	% of the	Fe(0)	$As_{(total)}$	% of the
	(µg/L)	control	(% ZVI)	(µg/L)	control
mZVI	11	1	36	3	<1
S-mZVI	29	4	91	-	-
nZVI	19	3	4	41	5
S-nZVI	114	15	16	47	6

As mentioned in section 1, Nyström 2022 conducted a follow-up column experiment testing these same ZVI particles. Columns were each packed with Ascontaminated soil from Hjältevad, as well as an aqueous suspension of each respective sorbent. There was also a control. AGW was then pumped through each column at 193 mL day⁻¹ for 52 days, or about 650 pore volumes. Overall, this study found that immobilization efficiency was highest for mZVI, followed by nZVI and then S-nZVI. Results for S-mZVI, the same one used in this current study, were inconclusive. S-mZVI showed a very high initial Fe loss (within 50 pore volumes), indicating fast leaching of S-mZVI. These results support the hypothesis that S-mZVI will be more mobile than both unsulfidated alternatives and S-nZVI.

3.5.2 Mobility column experiments

Further column experiments were conducted to examine nZVI mobility. Both nZVI and S-nZVI from previous experiments were tested. The nZVI was suspended in 3% PAA to increase mobility; manufacturers said that the S-nZVI suspension did not require additional modification. Columns were packed with contaminated Hjältevad soil. After a tracer was pumped through, 2 pore volumes of the respective ZVI suspension was pumped through. Another 4 pore volumes of AGW was then passed through the column. This experiment studied 4 different flow rates: 1.3, 2.5, 3.5, and 5.8 mL min⁻¹.

S-nZVI had a very low recovery rate (<0.1%), showing its very limited mobility. It was therefore discarded from this study. On the other hand, nZVI had more promising recovery rates, between 3.3 and 4.3% depending on flow speed. A positive linear relationship was found between flow rate and k, indicating irreversible interactions between ZVI particles and the colloid surfaces.

These experiments are discussed in detail in Berggren Kleja et al. 2024.

3.5.3 Pre-injection groundwater samples

Groundwater samples were taken at both injection sites prior to mZVI and nZVI injection, showing similar depth-dependent trends between the two plots for total aqueous As, pH, and Eh. For mZVI, total As peaked between 157.5 and 156.5 MASL, with a range of 1040–1940 µg L⁻¹. The pH increased with depth, from an average of 6.1 at 160.5 MASL to 7.4 at 154.5 MASL. Conversely, the Eh decreased with depth, from -34.1 at 160.5 MASL to -184.3 at 154.5 MASL. The nZVI site is over the source zone and consequently showed higher As levels: the peak was between 1940 and 4390 µg L⁻¹ between 161.5 and 154.5 MASL, respectively. The pH and Eh pattern followed mZVI's. The pH ranged from 6.49 at 161.5 MASL to 7.28 at 155.5 MASL, and the Eh from 1.33 at 161.5 MASL to -174.6 at 155.5 MASL (Fig. 9).

These results are discussed in detail in Berggren Kleja et al. 2024.

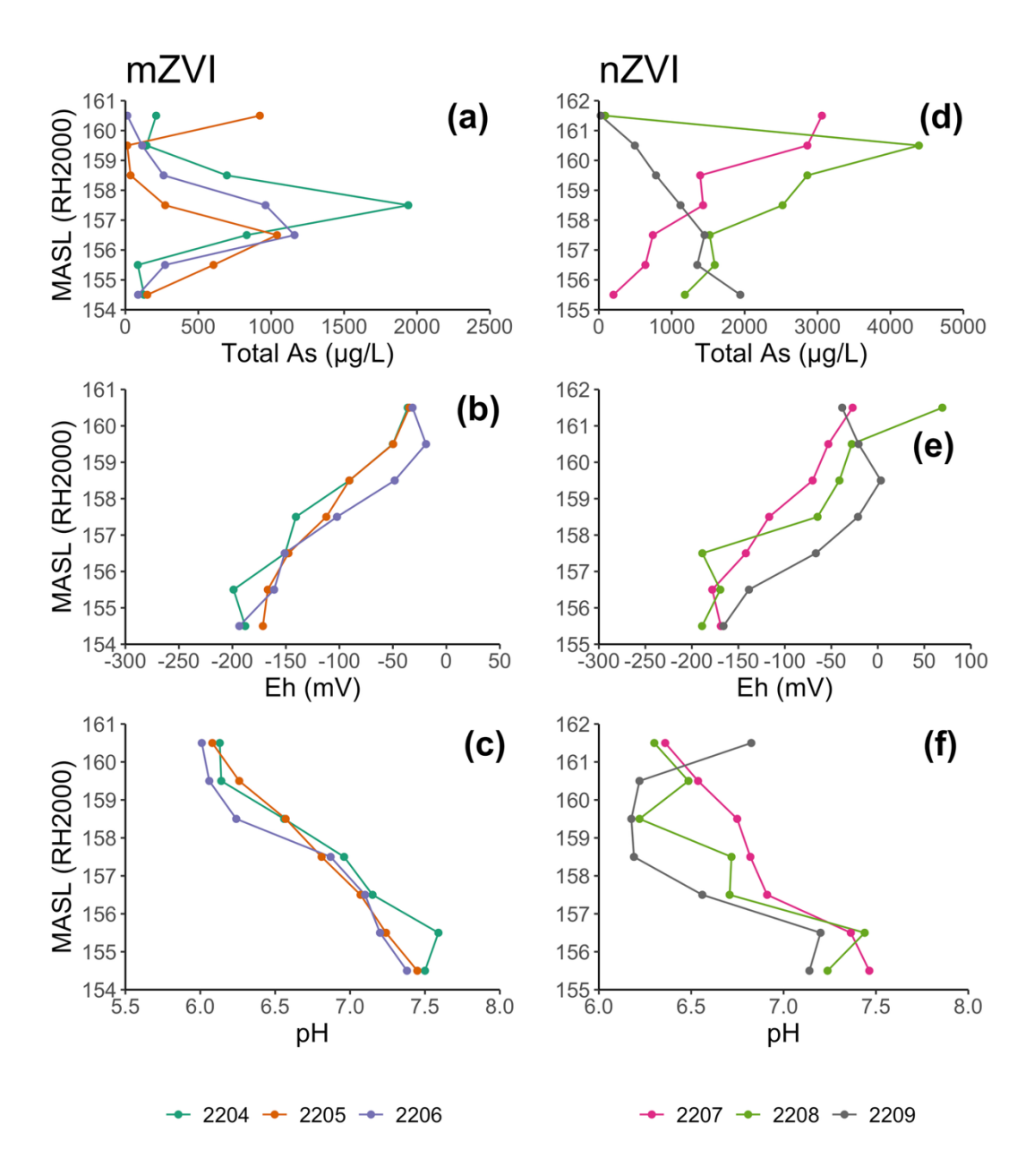


Figure 9. Total aqueous As, Eh, and pH in the groundwater in wells near the mZVI (a-c) and nZVI (d-f) injection points right before injection, with depth in meters above sea level (MASL). A map of these wells can be found in Fig. 6 (mZVI) and Fig. 7 (nZVI). Data from Berggren Kleja et al. 2024

3.5.4 Post-injection monitoring

After injection, 6 monitoring wells around each injection site (mZVI and nZVI) (Fig. 6, Fig. 7) were sampled 6 times over the course of 30 weeks.

PAA was added to the nZVI treatment to increase colloidal stability and mobility, and guar gum was added to mZVI for the same reason. Both can be detected as DOC, which can give an indication of ZVI's travel path.

Near the mZVI injection site, wells 2212 and 2213 showed an immediate spike in DOC levels post-injection, up to about 130 mg L⁻¹. These wells are found 1 m

downstream of mi4 and mi5, respectively. Well 2214, 1 m upstream of mi4, also saw a slight peak immediately after injection, to 57.7 mg L⁻¹. Wells 2210 and 2211, 4 m north of the injection site, saw a slight peak 10 weeks after injection to 39.9 and 51 mg L⁻¹, respectively. Within 18 weeks, however, DOC returned to background levels at all wells, likely from degradation of guar gum. Overall, the peaks in DOC were much lower than expected, indicating low mobility of mZVI. Additionally, there was no clear effect on total As, pH, or Eh across monitoring wells. Values across wells followed the same trends, providing further proof that mZVI had no effect on groundwater conditions, as otherwise there would be an inverse relationship between distance from the injection point and groundwater impact.

For the nZVI site, DOC only increased in wells 2218 and 2220, both of which are near injection point na4 (2218 is 0.5 m upstream and 2220 is 1.5 m downstream). These levels increased to 30.9 and 27 mg L⁻¹, respectively, but they soon returned to background levels. Assuming PAA is more mobile than ZVI, these results suggest very low nZVI mobility. Additionally, there was no clear effect on total As, pH, or Eh outside of natural variation. Although there was variation in total As both spatially and temporally, it was found that these changes were strongly controlled by proportion of As(III), not ZVI.

This data is summarized in Fig. 10 and outlined fully in Berggren Kleja et al. 2024.

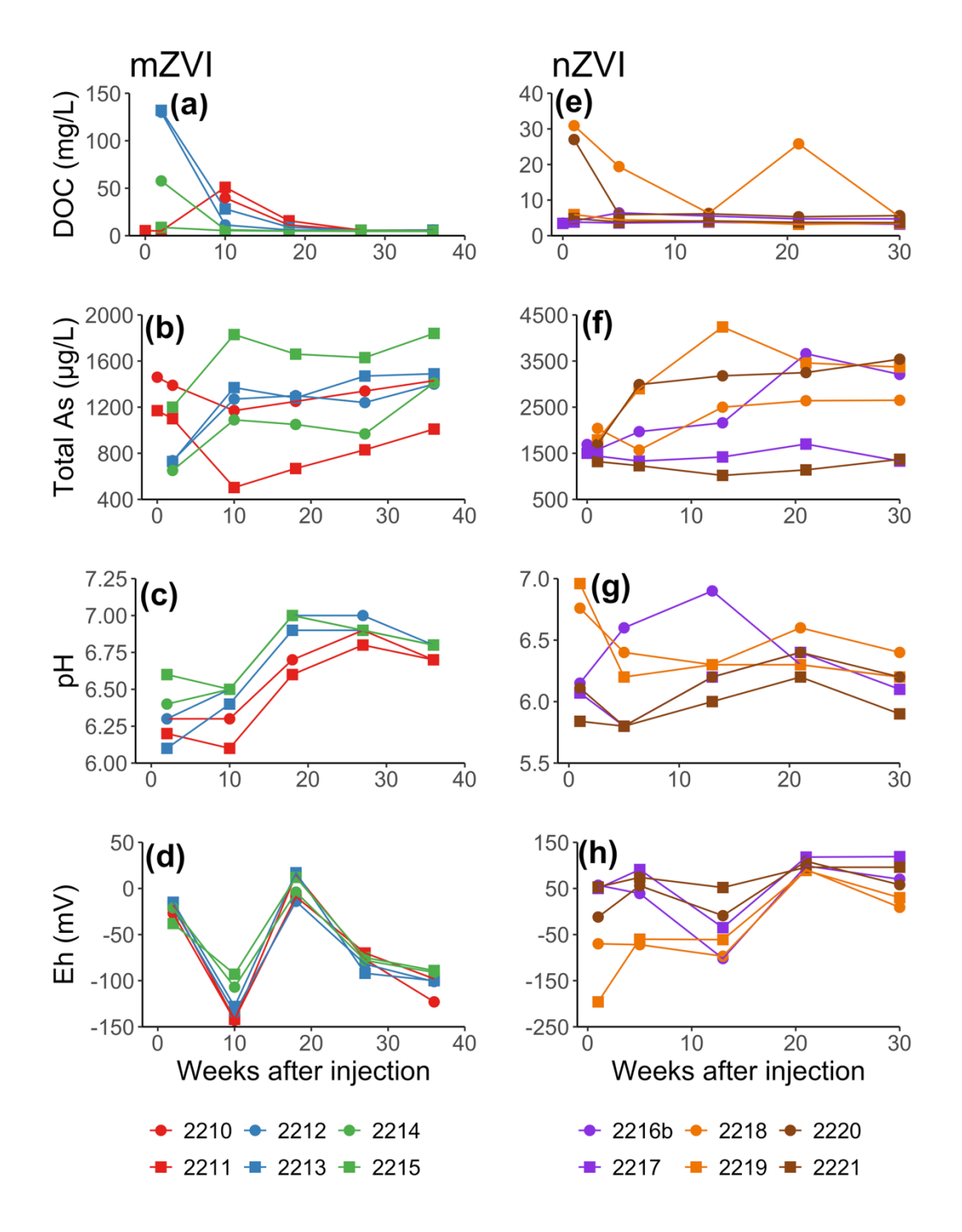


Figure 10. Dissolved organic carbon (DOC), total aqueous As, pH, and Eh in the groundwater in wells near the injection points for 30-40 weeks after injection for both mZVI (a-d) and nZVI (e-h). Map of the wells can be found in Fig. 6 (mZVI) and Fig. 7 (nZVI). Data from Berggren Kleja et al. 2024.

3.5.5 Long-term monitoring

Sweco has maintained a long-term monitoring of the site across several monitoring wells, both before and after injection (Fig. 11). Samples taken in 2022 occurred right before the injection. Overall, most wells do not show a change in total As.

In 2023, 2 samples taken from TB8 showed an increase in total dissolved As post-injection (Fig. 11b). However, there was a drop of 70 µg L⁻¹ between October 2023 and November 2024. It is hard to say at this point if this change is from natural fluctuations of As levels or an impact by ZVI.

Groundwater well 1903, however, showed a significant change in dissolved As after injection. This well is found approximately 1.5 m downstream of the nZVI site. Total dissolved As dropped from 3120 $\mu g \, L^{-1}$ in 2022 to 1940 $\mu g \, L^{-1}$ in 2023 and subsequently 1490 $\mu g \, L^{-1}$ in 2024. Groundwater well 1715_2, about 5 m downstream of the mZVI site, also saw a change. In 2023, dissolved As levels dropped from 1520 $\mu g \, L^{-1}$ to 192 $\mu g \, L^{-1}$ in 2023. However, they rose again to 1890 $\mu g \, L^{-1}$ in 2024. Overall, the results from these two wells (Fig. 11c) indicated that ZVI did have an impact on total As levels, although the effect was local and short-lived. Contrary to what was expected, the nZVI's effects seemed to be more enduring than those of mZVI.

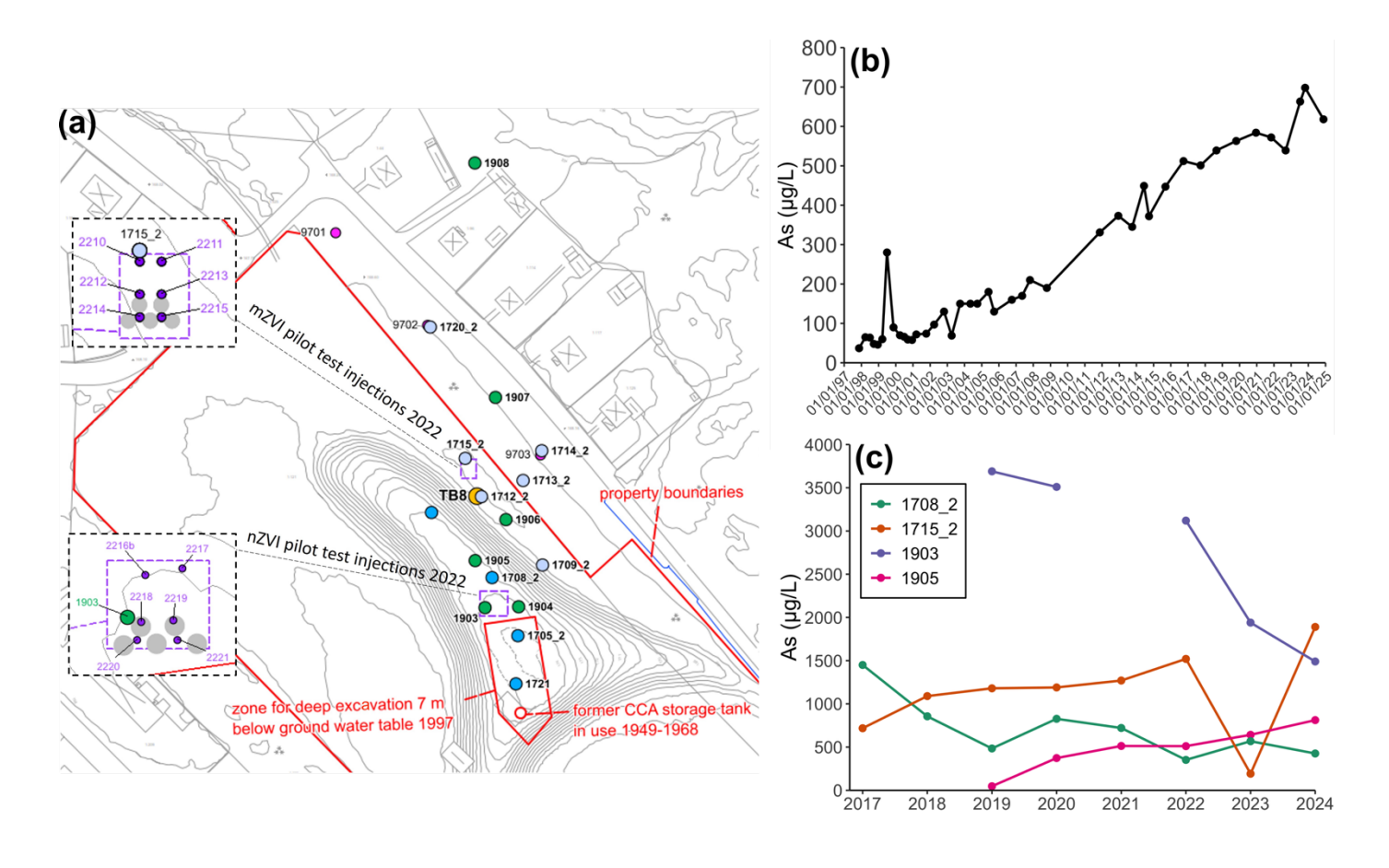


Figure 11. Map of monitoring wells in the area alongside As data. Figure (a) is an overview map of injection points and permanent monitoring wells. Graph (b) shows As levels in TB8 over time, and (c) shows other relevant monitoring wells (ones in the vicinity of the injection points with data collected both before and after injection). Data from 2022 was collected before the injections. Figure (a) and data for (b) and (c) are from Sweco 2025.

Table 2. Monitoring well depths for wells shown in Fig. 11b and 11c.

Monitoring well	Filter length (m)	Starting depth	Ending depth
		(MASL)	(MASL)
TB8	2	159.6	157.6
1708_2	1	159.2	158.2
1715_2	1	158.7	157.7
1903	4	161.2	157.2
1905	4	160.7	156.7

4. Materials and methods

4.1 Groundwater samples

Groundwater samples were taken two years (25 months) after injection using a geoprobe (Niras) (Fig. 12a). Samples were taken in 50 cm increments from 159.5 to 155 MASL in the mZVI plot, and from 161 to 158 MASL in the nZVI plot. The distribution of sampling points is displayed in Fig. 13 (mZVI) and 14 (nZVI).

Eh and pH were measured in the field using a Pro DSS Multiparameter Digital Water Quality meter (YSI, USA). Two samples were taken at each depth. The first was filtered through a 0.45 µm filter (Eijkelkamp, Netherlands). The second was filtered through both the same 0.45 µm filter and a second filter that selectively binds dissolved As(V) (Metalsoft, USA) to isolate As(III). All samples were acidified to 1% HNO3 to resuspend Fe before sending for analysis by ALS Scandinavia AB using ICP Atomic Emission Spectroscopy and/or ICP Sector Field Mass Spectrometry.

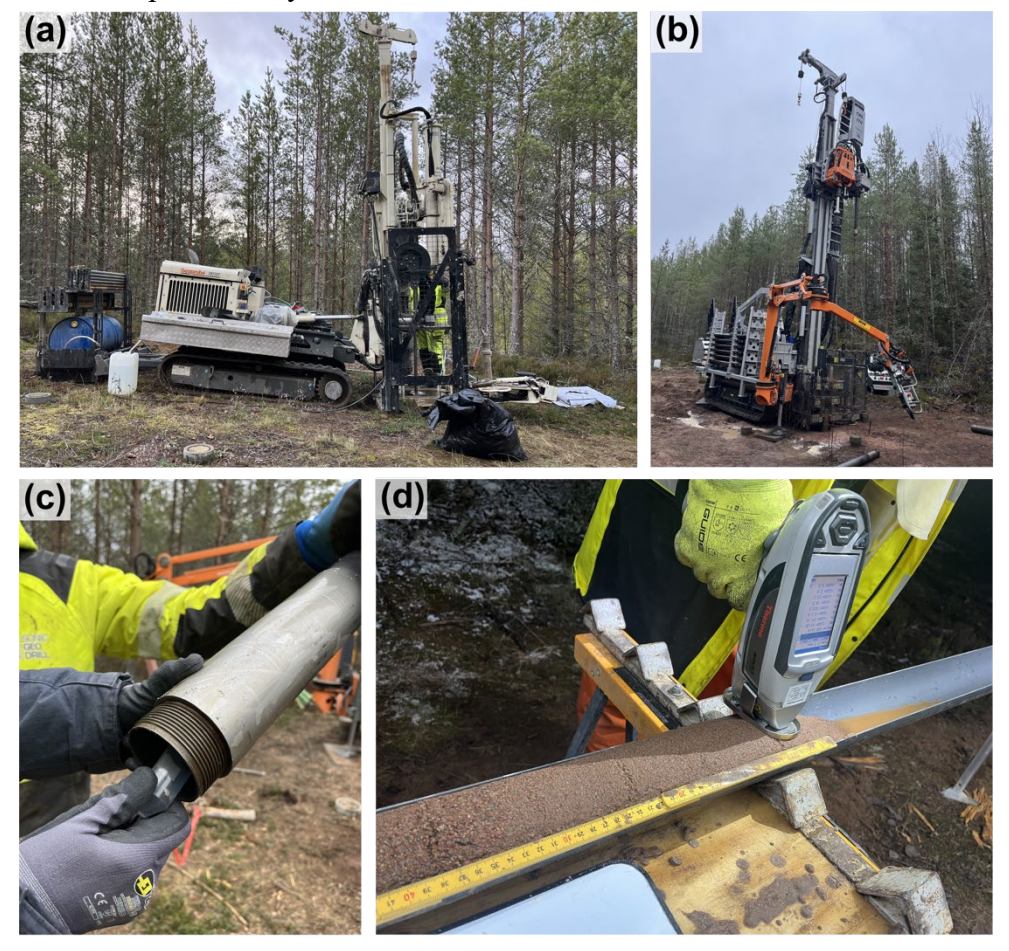


Figure 12. Groundwater and soil sampling images: the geoprobe, for groundwater sampling (a); the sonic drill, for soil sampling (b); an anoxic sample being taken (c), and x-ray fluorescence (XRF) measurements taken directly on a soil core (d).

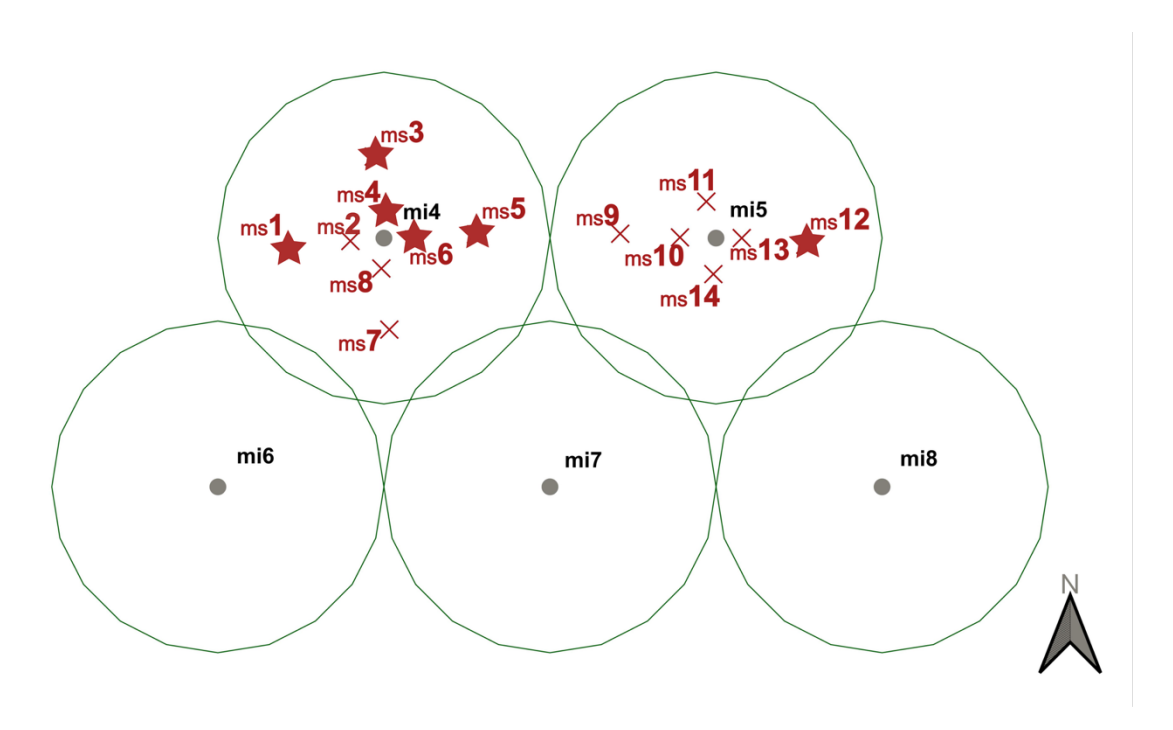


Figure 13. Map of groundwater and soil samples at the mZVI injection site. X's represent points where only a groundwater sample was taken, whereas stars show areas where both a groundwater and soil sample were taken. Green circles have a radius of 1 m.

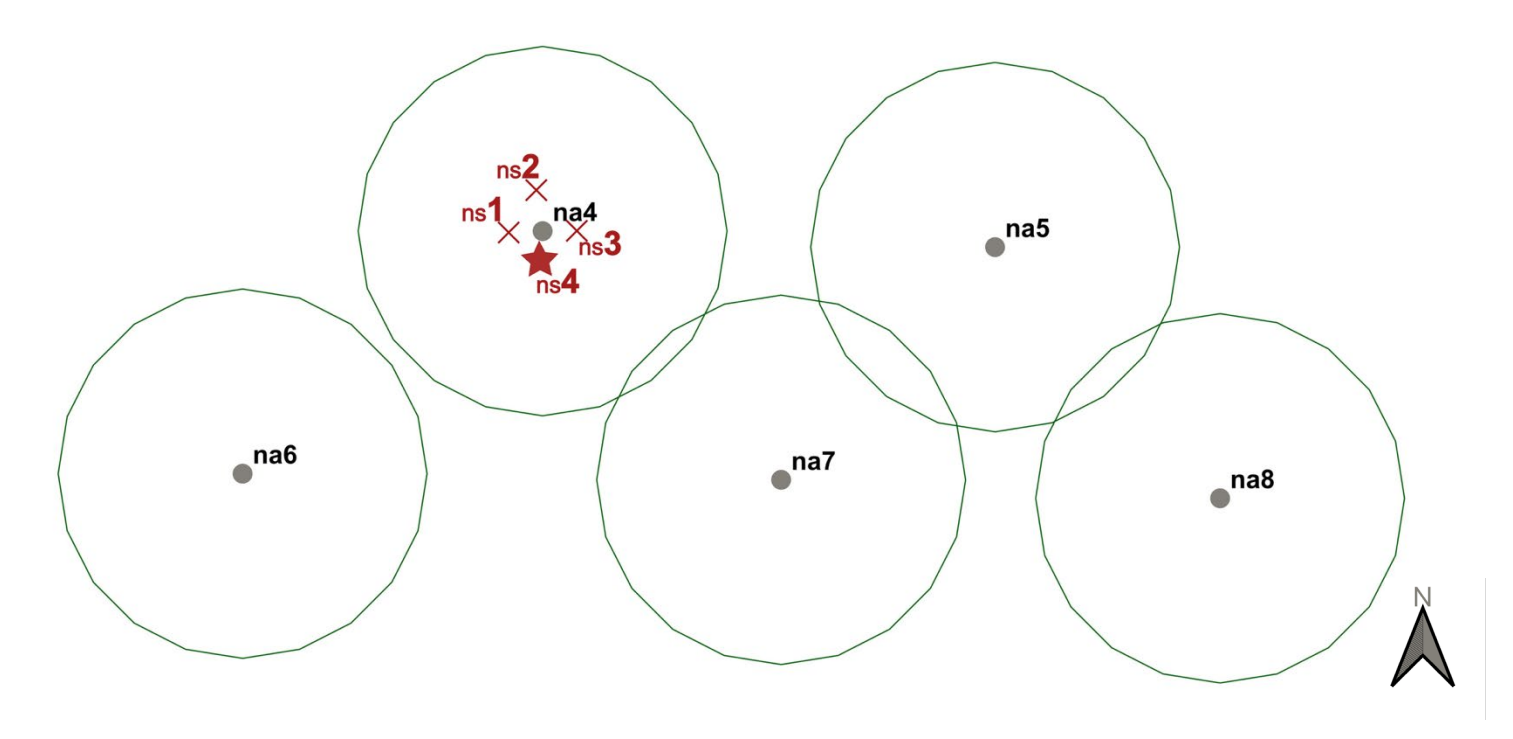


Figure 14. Map of groundwater and soil samples at the nZVI injection site. X's represent points where only a groundwater sample was taken, whereas the star shows the point where both a groundwater and soil sample were taken. Green circles have a radius of 1.5 m.

4.2 Soil samples

Soil cores were collected at points adjacent to groundwater samples using sonic drilling (Sonic Geo Drill) (Fig. 12b). Samples were about 65 mm in diameter. For the mZVI site, a total of 6 points were taken, at 1 m increments from 160 to 154 MASL. Owing to technical issues with the sonic drill, there are gaps in the data for all of these points at depths where soil samples could not be taken. Based on promising groundwater results, one full soil core was taken at the nZVI site the following spring, from 164 to 158 MASL. Sampling locations are shown in Fig. 13 and Fig. 14.

Samples were divided into 50 cm increments, mixed thoroughly by hand and with a handheld mixer, and sent to ALS for analysis of total As and Fe, where they were digested in *aqua regia* before ICP-MS analysis.

X-ray fluorescence (XRF) measurements were taken with a Niton XL3t portable XRF analyzer (Thermo Scientific, USA) in 5–10 cm increments on select intact soil cores (Fig. 12d), as well as on all mixed bulk samples.

Solid samples were also taken from the nZVI core for As and Fe molecular speciation analysis using XAS. Two samples were collected in 50 mL centrifuge tubes directly from the bottom of the soil core every 50 cm (Fig. 12c). Extra samples were taken wherever Fe clumps (dark black sections) were visible after the core was extracted from the drill. Care was taken to maintain anoxic conditions during sampling to conserve As and Fe speciation. Each sample was immediately frozen in dry ice, and later placed in a biaxially oriented polyethylene terephthalate (BoPET) bag with a layer of Al foil (Mylar) with oxygen absorbers. They were then flushed with N₂ gas, sealed with a heat sealer, and again stored in dry ice for transport. Samples were stored at -20°C while awaiting spectroscopy measurements.

4.3 X-ray absorption spectroscopy

K-edge XAS for As and Fe was performed at the Balder beamline at the MAX IV laboratory, Lund, Sweden, to determine As and Fe speciation. Before analysis, anoxic samples were prepared with two different methods. A portion, 8, of samples were freeze-dried (Mechatech, UK) for 48 hours. They were immediately transferred to a N₂-saturated glovebox (Labconco, USA) equipped with catalytic O₂ removal. In the glovebox, the samples were placed in Mylar bags again with oxygen absorbers and sealed with heat before they were transported for spectroscopy analysis. The 7 remaining samples were not freeze-dried, but instead kept in the Mylar bags and thawed at the MAX IV laboratory.

All samples, both fresh and freeze-dried, were handled in an anaerobic chamber (Coy, USA) at MAX IV. Samples were packed on sample holders and analyzed at liquid He temperature (10K) to prevent sample damage by

photoreduction and to increase the signal-to-noise ratio. The beamline used a Si[111] monochromator. The signal was acquired in fluorescence mode using a 7-element SDD detector. For the As K-edge analysis, energy calibration was conducted using a Se foil at the Se K edge at 12658 eV. During the collection of fluorescence data, a Cu 3λ -filter and an Al foil were used to reduce background scatter. After samples were run, a Au foil was used to calibrate the Au L(III) edge at 11919 eV. For each sample, 4 scans at 4 different measurement spots were taken with a 1 x 1 mm X-ray beam. The Fe K-edge analysis was calibrated with an Fe foil at 7112 eV, and 2 scans were collected at 8 measurement spots with a 100 x 100 μ m focused beam. Only fresh samples were used for the Fe analysis as these samples were expected to give the least alteration of the original speciation. Time constraints also led us to omit the freeze-dried samples from the Fe analysis.

Jon-Petter Gustafsson conducted the data treatment for the X-ray absorption near-edge structure (XANES) results, presented in this paper. Data was merged and normalized with Athena, part of the Demeter software suite (Ravel & Newville 2005). Subsequent linear combination fitting (LCF) was conducted using LCF-LinEst code in Visual Minteq (Gustafsson 2022) between 7102 and 7172 eV for Fe and 11854 and 11924 eV for As. LCF-LinEst was also used for uncertainty analyses (Formentini et al. 2024). The realgar standard was kindly provided by Langner et al. 2012, and the arsenopyrite standard was shared by Christian Mikutta (unpublished).

Extended X-ray absorption fine structure (EXAFS) analyses are currently being investigated by Carin Sjöstedt.

As with the other soil samples, after XAS the anoxic samples were sent to ALS for *aqua regia*-assisted digestion for analysis of total Fe and As with an ICP-MS.

4.4 Column experiments with S-MicroZVI

Column experiments were done to assess the mobility of S-MicroZVI® (S-mZVI) from Regenesis, USA as an alternative for future injections. Although both S-nZVI and S-mZVI have an FeS coating that should increase mobility, the S-mZVI particles were considered more suitable than S-nZVI due to their comparatively higher As(III) immobilization (Formentini et al. 2024), and S-nZVI's low mobility in previous column tests (Berggren Kleja et al. 2024). S-mZVI's nominal particle diameter is 2–3µm. It is composed of sulfidized ZVI suspended in a proprietary mixture of 40–50% Glycerol, 30–50% ZVI, and 1–4% Iron(II) Sulfide.

The soil used for the column experiments was collected in 2019 by Sweco, at sample point 1904 (Fig. 11). A soil core was taken 16–18 m below the surface (158–156 MASL) with a Sonic Geo Drill. The sediment material was then thawed and dried in a glove box. More details on the sampling procedure can be found in Nyström 2022.

Experiments were tested at 4 different flow speeds: 1.34, 2.67, 3.52, and 5.50 mL min⁻¹. These speeds are adopted from a field situation with an injection rate of 0.4 L s⁻¹ through a nozzle with an inner diameter of 5 cm and an injection depth span of 2 m (Comba & Braun 2012). As flow velocity decreases hyperbolically with distance from the injection well, the speeds correspond to a distance from the injection point of approximately 0.3, 0.7, 1.1, and 2.7 m respectively.

Column experiments used Diba Omnifit® EZ Chromatography Columns, made with borosilicate glass, with dimensions 2.5 x 10 cm. Filters attached to the columns were removed, as these have been shown to affect the breakthrough curves of nanomaterials (Norrfors et al. 2021). Instead, both ends were lined with 70 µm Nylon mesh filters (Spectrum® Laboratories, Malaysia) that were shown not to interact with nanoparticles.

Columns were packed by alternating between small quantities of soil and AGW to prevent air entrapment. AGW was made to replicate the average ionic composition of the groundwater at the study site (Formentini et al. 2024). The following concentrations were diluted in Ultrapure water (ELGA, USA): 0.2 mM K₂SO₄, 0.450 mM CaCl₂•2H₂O, 0.750 mM NaHCO₃, 0.050 mM KHCO₃, 0.100 mM MgCl₂•6H₂O, 0.015 mM NH₄Cl, and 0.001 mM KH₂PO₄. The solution was then adjusted to pH 6 using diluted HCl. Columns were packed until approximately 10 cm of soil were added.

The column was then flushed at the corresponding flow rate with AGW for 1 to 2 hours, or until the leachate was clear. In order to obtain effective porosity and dispersivity of a soil for modeling breakthrough curves of the study particles, a conservative tracer with a low affinity for most soils, such as NaCl, is often passed through columns. For this purpose, 2 pore volumes of 50 mM NaCl were pumped through each column while measuring conductivity with a signal conditioner (eDAQ, Australia). AGW was then pumped for at least 2 pore volumes, or until conductivity reached a steady state. A fresh S-mZVI suspension of 5 g Fe L⁻¹ was prepared at this point, mixing 2 g of S-mZVI with 200 mL AGW with a high-shear mixer for 1 minute at 8000 sec⁻¹ (InterMed, Denmark). The suspension was passed through the column for 2 pore volumes while collecting samples at respective intervals depending on the flow rate (every 2, 1, 0.75, and 0.5 mins, respectively) using a fraction collector (Gilson, USA). Finally, the column was rinsed with 4 pore volumes of AGW while continuing to collect leachate. The column setup can be found in Fig. 15.

For the first replicate of each flow speed, each leachate (2 mL) was combined with *aqua regia* (8 mL) in 80 mL Teflon digestion tubes (Milestone, Italy) and then digested in a microwave (Ethos Easy, Milestone, Italy). Samples were heated to 1800 W over the course of 20 minutes, then maintained at that temperature for 10 minutes before cooling, following a modified version of the US EPA 2051a

standard procedure for soil samples (US EPA 2007). Samples were subsequently diluted (50 mL) with Ultrapure water before subsequent dilution for measurements using ICP-MS.

This set of replicates showed signs of cross-contamination (Fe residues in the microwave tubes) and poor digestion (ZVI flakes still visible after digestion). In order to minimize cross-contamination, controls (ultrapure water and AGW) were only digested in microwave tubes without visible Fe residue, and tubes with black Fe residue were used for the ZVI control digestions or leachates with high levels of Fe. Nevertheless, contamination remained an issue.

For the second replicates, more precautions were therefore taken to minimize cross-contamination and ensure proper digestion. The microwave tubes in the first set of replicates were cleaned by scrubbing with dish soap and cleaning in the dish washer. For the second set of replicates, additional steps were added: after scrubbing with dish soap and washing in the dish washer, the tubes were cleaned in the microwave's pre-set cleaning cycle with 65% HNO₃ (5 mL) and ultrapure water (5 mL), per manufacturer's instructions. They were again scrubbed and dish-washed before further use. These steps seem to have minimized cross-contamination, as it was not a further issue in the second set of replicates. To improve digestion, column experiments and digestions for the second replicates were executed on the same day (in the first set of replicates, digestions occurred the day following column experiments). Additionally, samples were vortexed (5 sec) after the addition of *aqua regia* and before digestion. These extra steps appeared to be successful as this set of replicates did not show visible evidence of undigested ZVI.

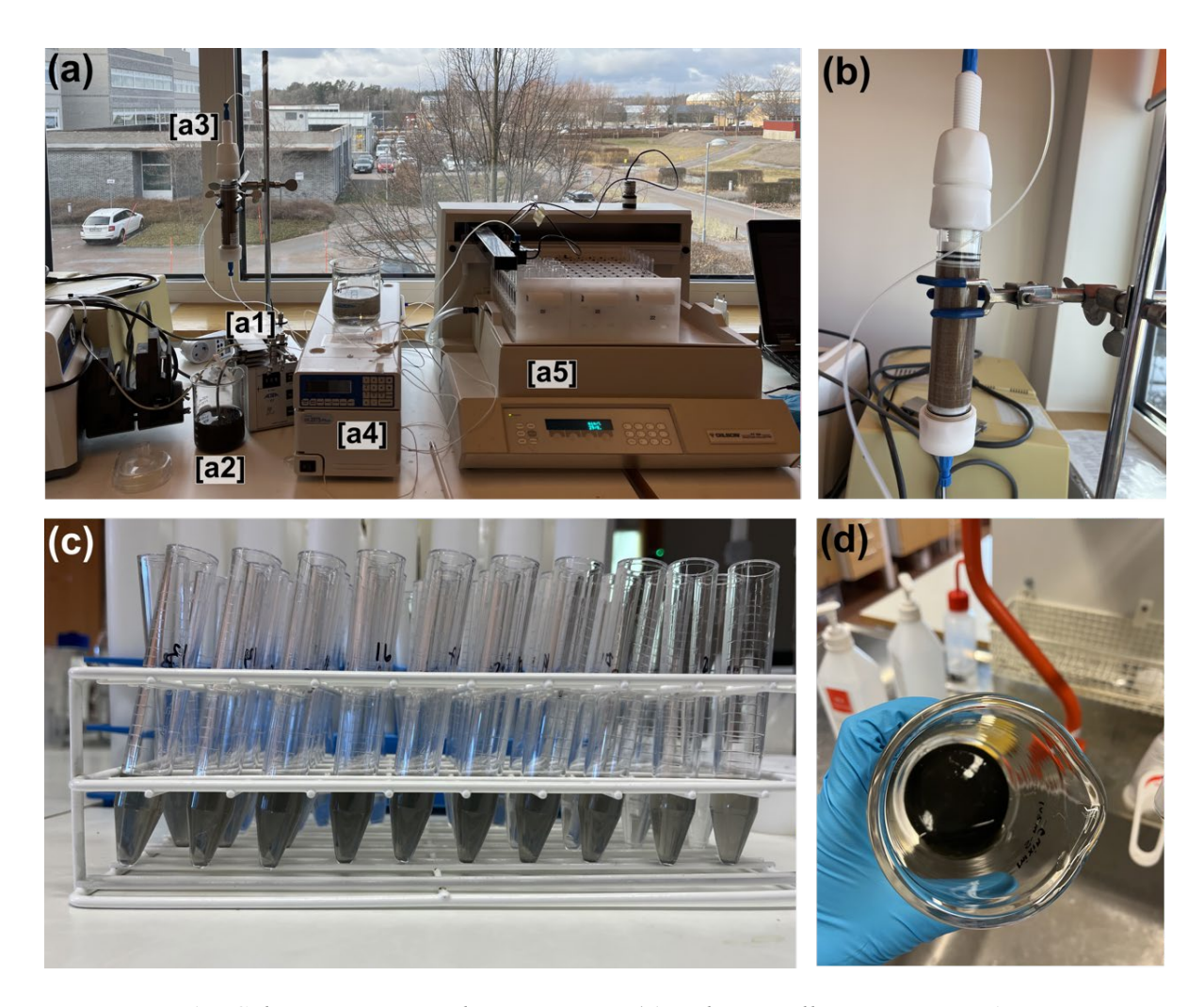


Figure 15. Column experimental set-up. Image (a) is the overall setup: pump [a1], ZVI stock solution [a2], column [a3], conductivity meter [a4], and fraction collector [a5]. Image (b) is a close-up of a packed column, and (c) shows the leachate collected in the fraction collector after 2 pore volumes of ZVI have been pumped through. Image (d) is the ZVI that settled in the bottom of the beaker during the experiment.

4.5 Mobility modeling

Modeling was handled in Hydrus 1D version 4.17.0140.

Inverse modeling was conducted using tracer data to first fit effective porosity (equivalent to volumetric water content under saturated conditions) and dispersivity. These values were then applied to colloid transport inverse modeling, and the attachment rate constant (k) was fitted.

The advection-dispersion equation is used for describing one-dimensional transport of solutes and particles in soils, as well as chemical interactions between particles and collectors. *Advection* is the movement of a solute with liquid;

dispersion is a measure of varying transport velocities of a solute through the soil, depending on the size and distribution of pores.

The primary equation applied here is a colloid transport and fate model that is modified from the advection-dispersion equation for solute transport (Šimůnek et al. 2018):

$$\frac{\partial \theta c}{\partial t} + \rho \frac{\partial s}{\partial t} - \frac{\partial}{\partial x} \left(\theta D \frac{\partial c}{\partial x} \right) + \frac{\partial qc}{\partial x} = 0$$
 (5)

where c is the colloid concentration in the aqueous phase [N_cV⁻³], t is time [T], ρ is the bulk density of the porous medium [M L⁻³], s is the solid phase colloid concentration [N_cM⁻¹], θ is the volumetric water content [V³V⁻³], D is the effective dispersion coefficient, s is the spatial coordinate, with positive upwards [L], and s is the Darcian fluid flux density, here equivalent to the flow rate [VT⁻¹]. Mass transfer from aqueous to solid phase can be described as:

$$\rho \frac{\partial s}{\partial t} = \theta kc \tag{6}$$

where k is the first-order attachment coefficient (T⁻¹).

D, the dispersion coefficient in the liquid phase, is a combination of longitudinal dispersion and diffusion. It is calculated as follows:

$$\theta D = D_L |q| + \theta D_w \tau_w \tag{7}$$

 D_L is the longitudinal dispersivity (L), D_w is the molecular diffusion coefficient in free water [V² T⁻¹], which is 1.01×10^{-3} cm² min⁻¹ for NaCl, and τ_w is a tortuosity factor in the liquid phase [-].

Saturated hydraulic conductivity was calculated using Darcy's law, and saturated conditions were assumed.

Experimental results showed signs of blocking, where the initial attachment of particles to porous media decreases the attachment rate of subsequent particles. Blocking can be added to the mass transfer equation:

$$\rho \frac{\partial s}{\partial t} = \theta k c \psi \tag{8}$$

in which ψ is a colloid retention function [-]. It decreases with increasing colloid mass retention, and describes blocking with the following Langmuarian dynamics equation:

$$\psi = \frac{s_{max} - s}{s_{max}} = 1 - \frac{s}{s_{max}} \tag{9}$$

 s_{max} is the maximum solid-phase concentration [M M⁻¹] and s is the adsorbed solute concentration [-]. In Hydrus-1D modeling, s_{max} was fitted after k. A value range was adapted from S-nZVI values in Veselská et al. 2024 (0.004 to 0.015 kg kg⁻¹).

5. Results

5.1 mZVI treatment plot

5.1.1 Groundwater

Fig. 16 shows total As concentrations, percentage As(III), Eh, and pH for mZVI groundwater samples around injection points mi4 and mi5. Overall, groundwater conditions were not affected by mZVI. Total As was consistent with the pattern before injection, with As peaking between 158.5 and 156 MASL. Peak As concentrations ranged from 1520–2320 μg L⁻¹, with a mean of 1948.6 μg L⁻¹. Samples were dominated by As(III) over As(V), oscillating around 100% As(III) (total mean of 96% As(III)). Point ms2 dropped to 9% at 158.5 MASL. However, as this point and depth did not show any change in pH or Eh, it is likely experimental error. At 158 MASL it overshot As(III) concentrations to 200%, further indicating sampling issues.

As ZVI oxidizes, it should lower the Eh and increase the pH of the groundwater. Compared to results from before the injection, mZVI showed no change to groundwater Eh. It was still decreasing with depth, with a range of -25.94 mV (average) at 159.5 MASL to -174.74 mV (average) at 155 MASL. For comparison, the pre-injection range was between -20 and -200 mV. There was also no change in pH. It increased with depth. The pH range was an average of 6.48 at 159.5 MASL to 7.50 at 155 MASL (the range was 6.1 to 7.4 pre-injection). Fig. 17 displays a stability diagram for As, both at room temperature (as in lab conditions) and at 6°C (the temperature of the aquifer) with groundwater conditions overlayed. With the Eh and pH from these samples, all As falls within the As(III) sector of the stability diagram.

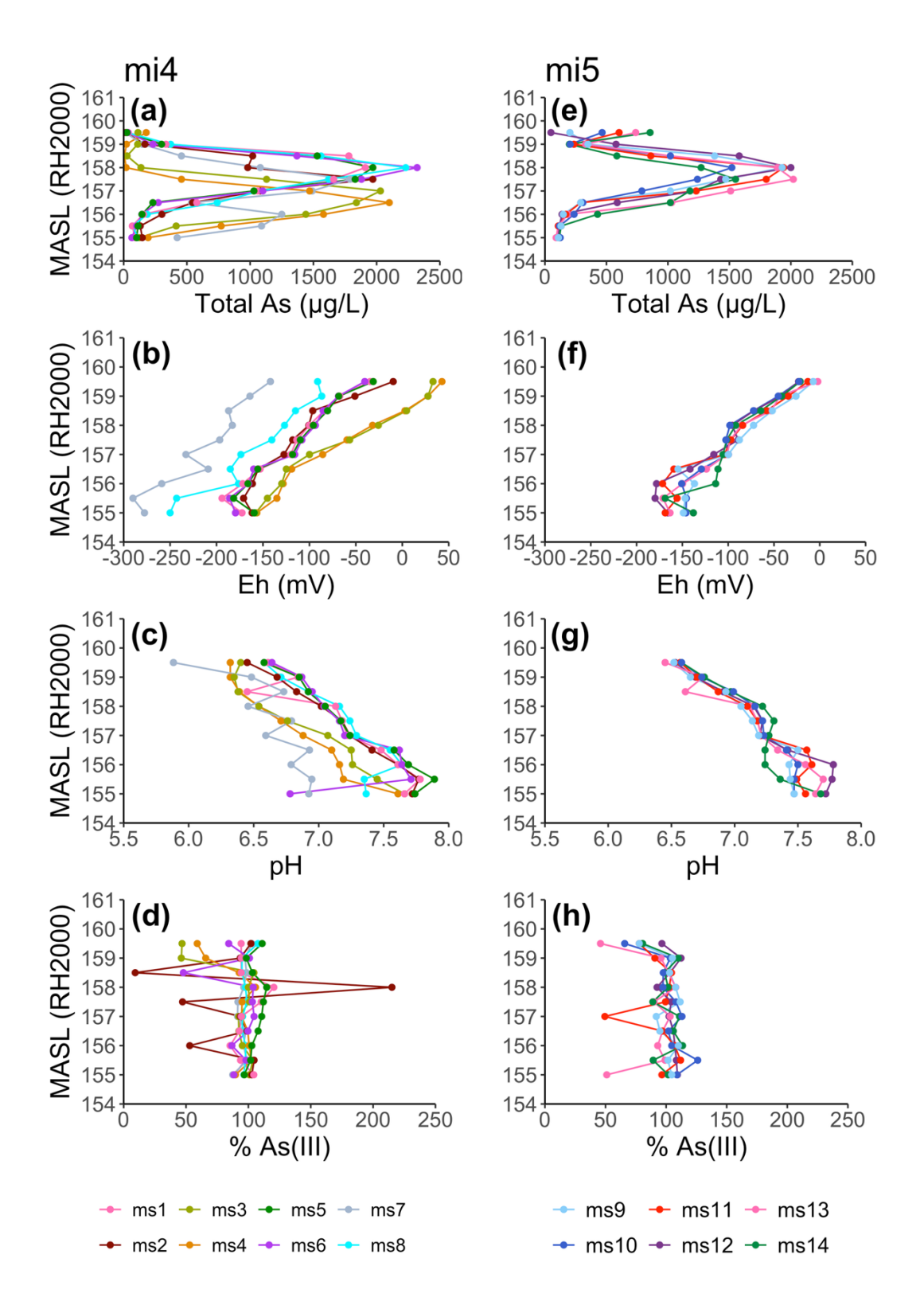


Figure 16. Total aqueous As, Eh, pH, and percentage As(III) in the groundwater near the two most downstream mZVI injection points (mi4 and mi5), 2 years after injection, with depth in meters above sea level (MASL). Map of sample points is in Fig. 13. For comparison, pre-injection data is found in Fig. 9.

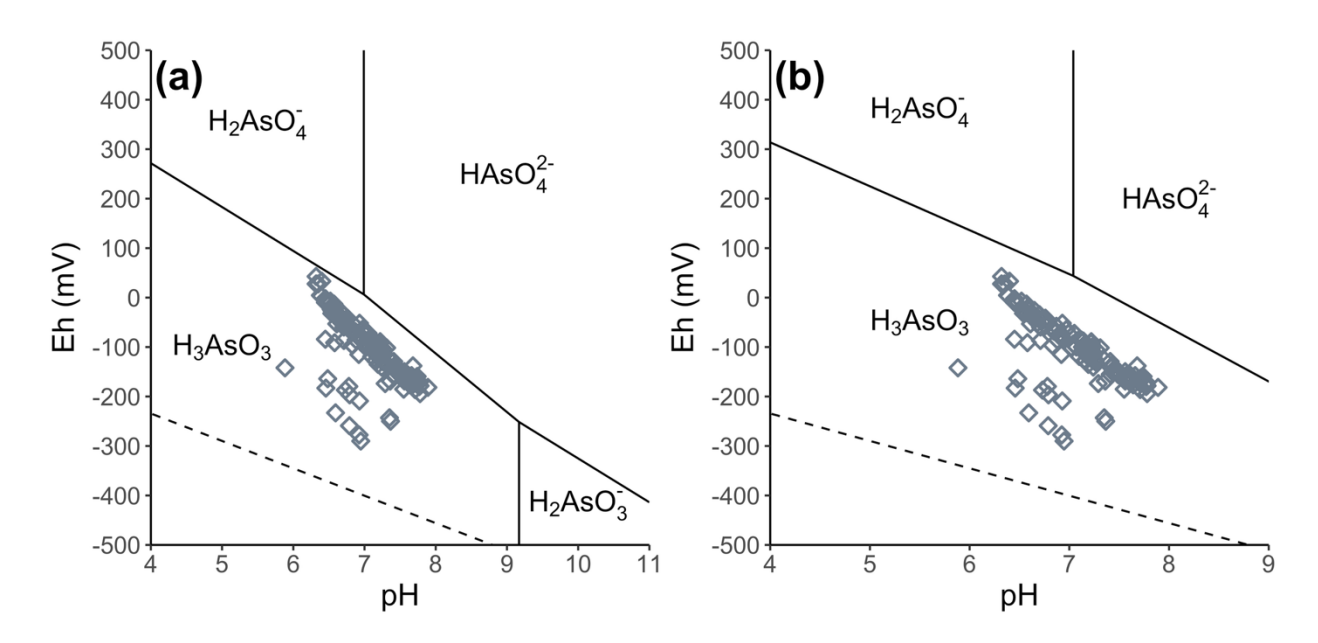


Figure 17. Pourbaix diagram for the distribution of aqueous As as either As(III) or As(V), overlayed with groundwater conditions from mZVI groundwater sampling. Graph (a) displays values at 25 °C—room temperature—and graph (b) at 6 °C, the average annual temperature of the aquifer. Stability lines were calculated using thermodynamic data from the database of Visual MINTEQ, vers. 3.1 (Gustafsson 2013).

5.1.2 Soil samples

Figs. 18–22 show images of mZVI soil profiles alongside their respective solid-phase Fe and As concentrations. There were technical issues with the sonic drill during soil core collection, so there are large gaps in the data. Samples were taken in roughly 50 cm increments, with shorter sections when there was soil loss. Points were graphed as the middle point of the sampled section. Concentrations for Fe for mZVI were highly inconsistent both within and between cores: the overall range was between 4670 and 484,000 mg kg⁻¹. The peaks were not consistent with depth, but they all occurred below 157.5 MASL. Solid-phase As concentrations were quite low relative to groundwater concentrations, up to 20.8 mg kg⁻¹.

Most points did not show a correlation between solid-phase Fe and As, except points ms3 and ms4. Point ms3 (Fig. 19) had 2 peaks, one at 156.2 MASL (484,000 mg kg⁻¹ Fe and 17.9 mg kg⁻¹ As), and one at 154.65 MASL (414,000 mg kg⁻¹ Fe and 14.10 mg kg⁻¹ As). Point ms4 (Fig. 20) had one peak, at 154.8 MASL (84,900 mg kg⁻¹ Fe and 8.23 mg kg⁻¹ As), and a lower one at 153.25 MASL (54,200 mg kg⁻¹ Fe and 3.97 mg kg⁻¹ As). Neither point showed any impact on Eh, pH, total As, or As speciation in the groundwater.

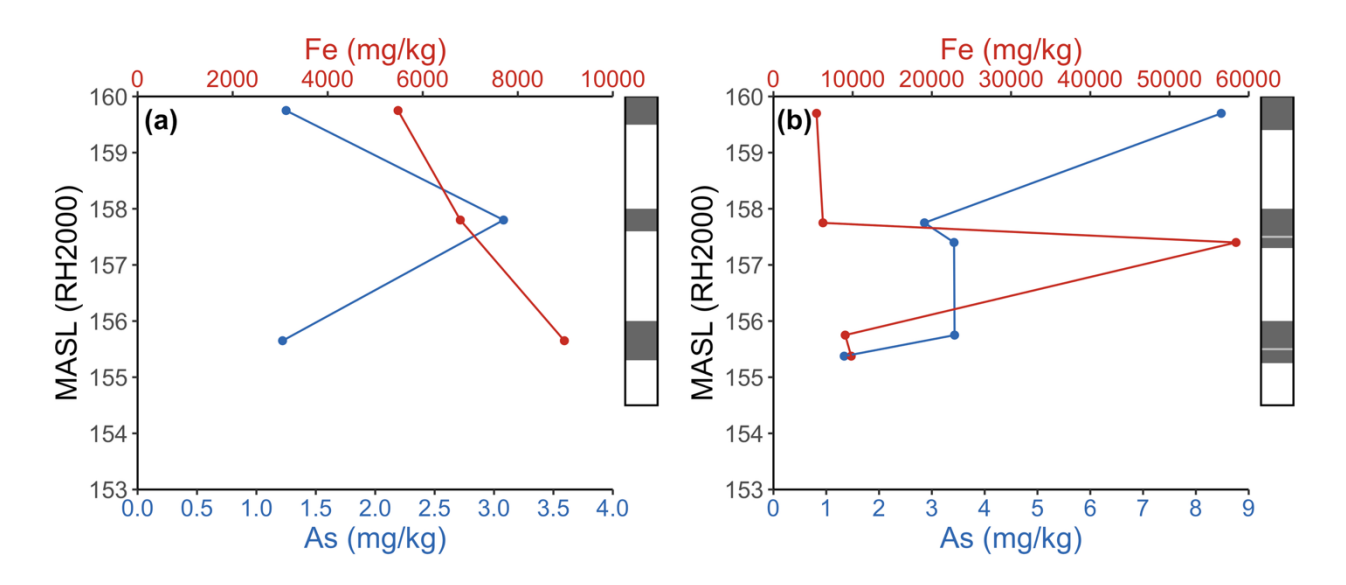
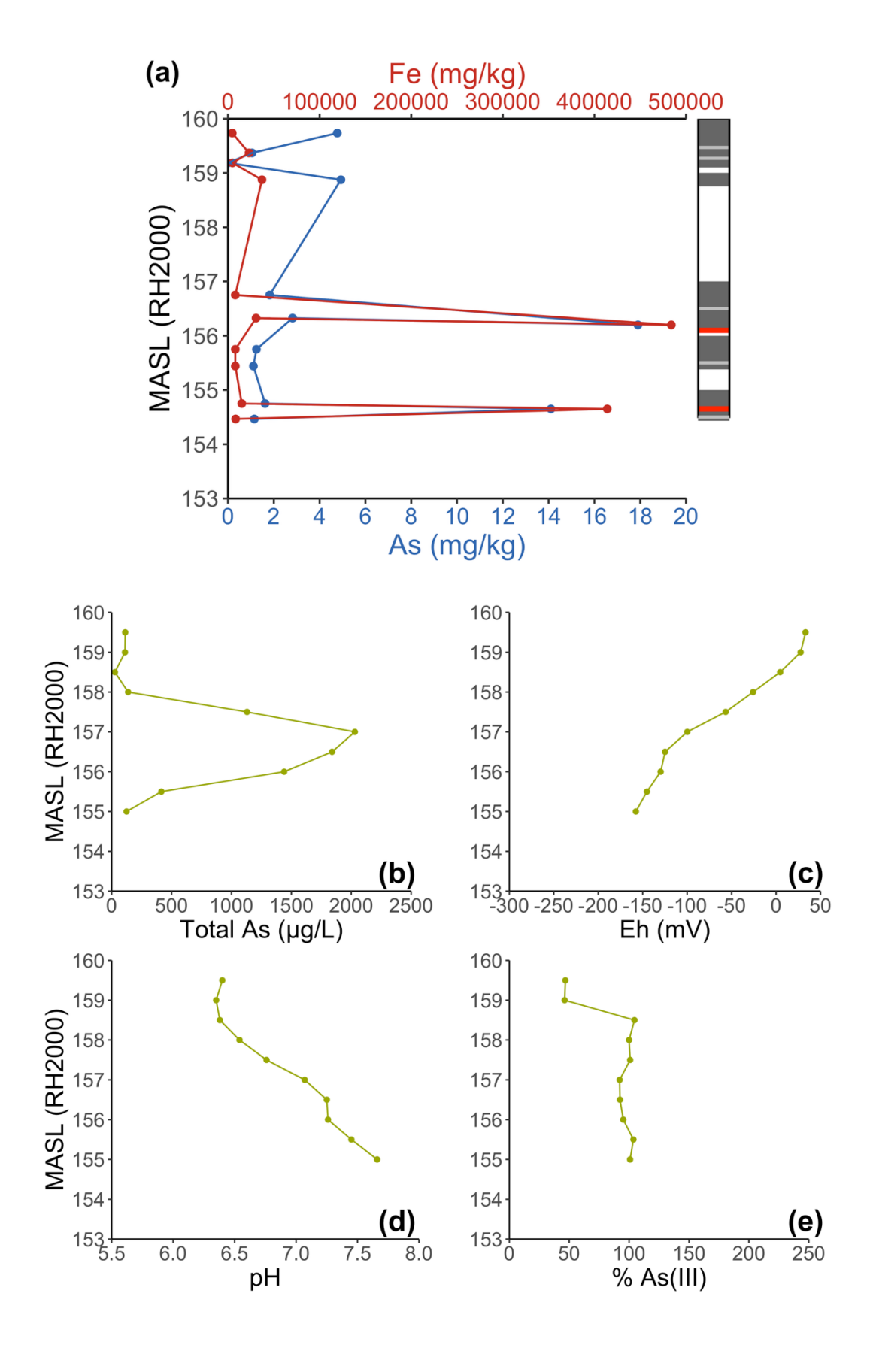


Figure 18. Solid-phase Fe and As concentrations for mZVI soil profiles ms1 (a) and ms12 (b). Depth is in meters above sea level (MASL). Boxes to the right of each graph represent succesfully collected samples in dark gray, and attempted sample collection as a black box. No images were taken for these samples.



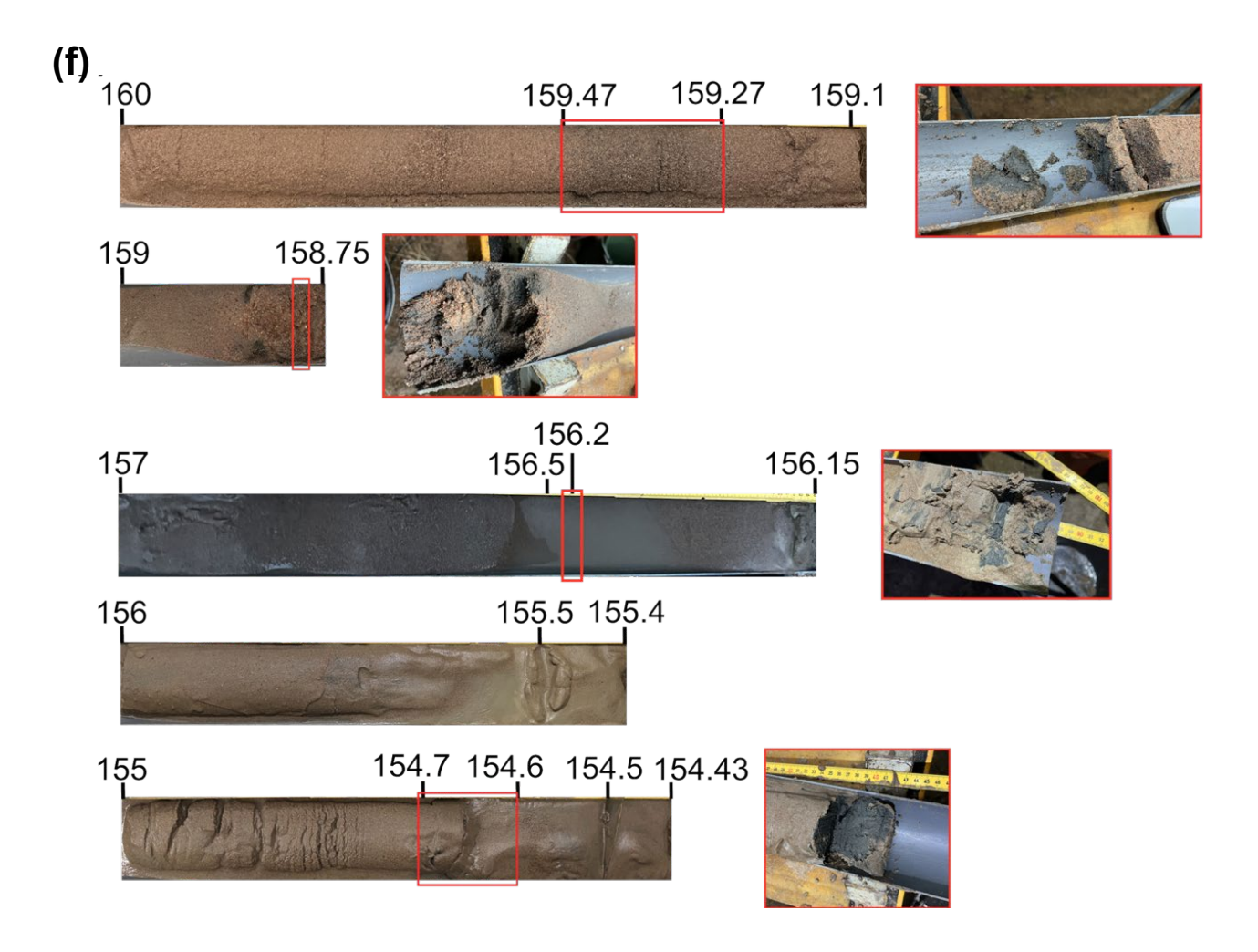
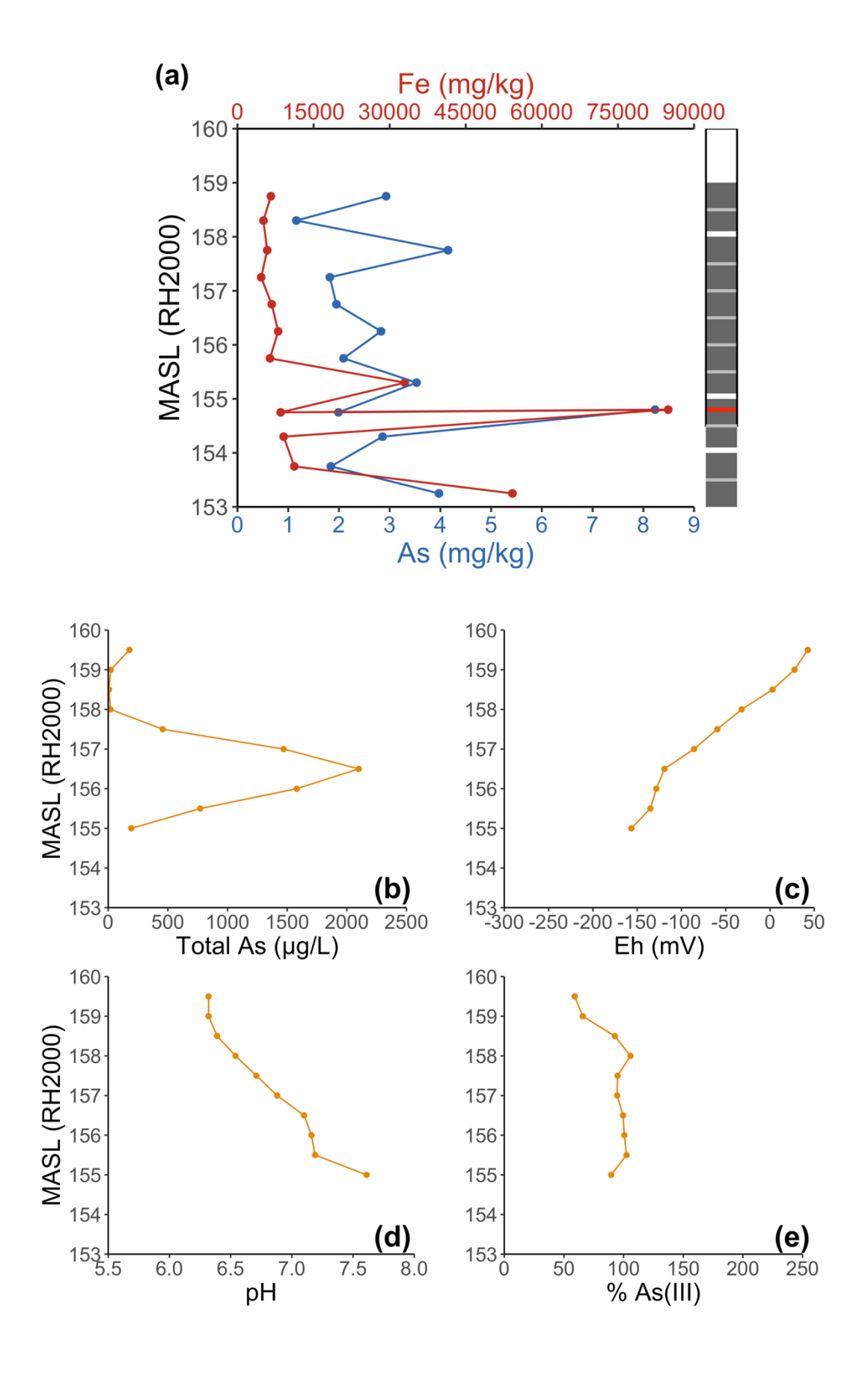


Figure 19. Soil profile for mZVI sampling point ms3 Fe and As results alongside groundwater data and images. Graph (a) shows solid-phase Fe and As concentrations. The box to the right of the graph represents succesfully collected samples in dark gray, and attempted sample collection as a black box; red lines are samples taken separately from the larger 50 cm section due to visual presence of a dark Fe clump. The last sample extracted more soil than expected, and runs deeper than the attempted sample depth. Groundwater results corresponding to the soil sample point for total aqueous As (b), Eh (c), pH (d), and % As(III) (e) are also shown for comparison. Images of successful cores are represented with depths in meters above sea level (MASL) in (f). Red boxes correspond to zoomed-in photos to the right of the main image.



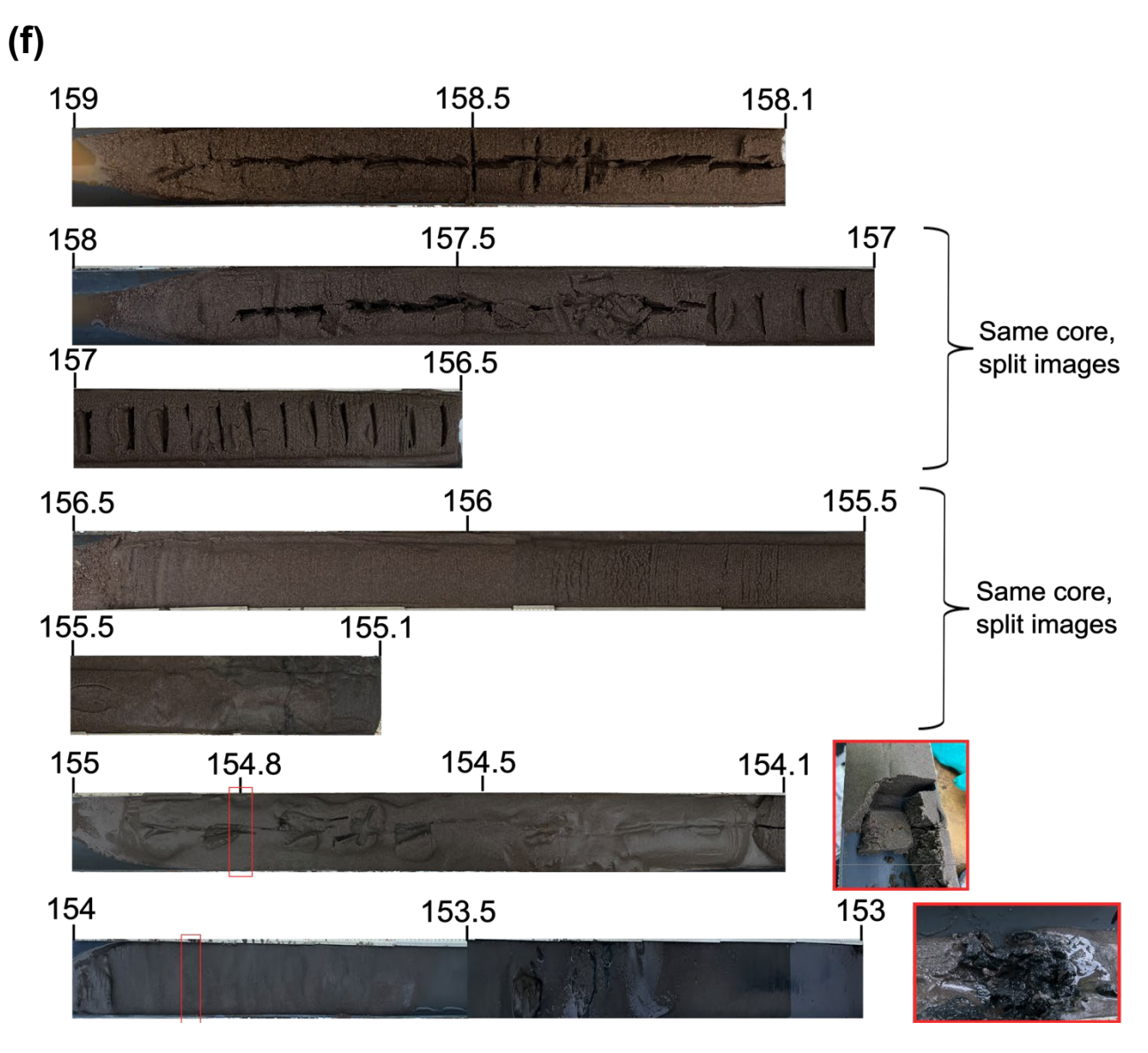


Figure 20. Soil profile for mZVI sampling point ms4 Fe and As results alongside groundwater data and images. Graph (a) shows solid-phase Fe and As concentrations. The box to the right of the graph represents succesfully collected samples in dark gray, and attempted sample collection as a black box; the red line is a sample taken separately from the larger 50 cm section due to visual presence of a dark Fe clump. The last sample extracted more soil than expected, and runs deeper than the attempted sample depth. Groundwater results corresponding to the soil sample point for total aqueous As (b), Eh (c), pH (d), and % As(III) (e) are also shown for comparison. Images of successful cores are represented with depths in meters above sea level (MASL) in (f). Red boxes correspond to zoomed-in photos to the right of the main image.

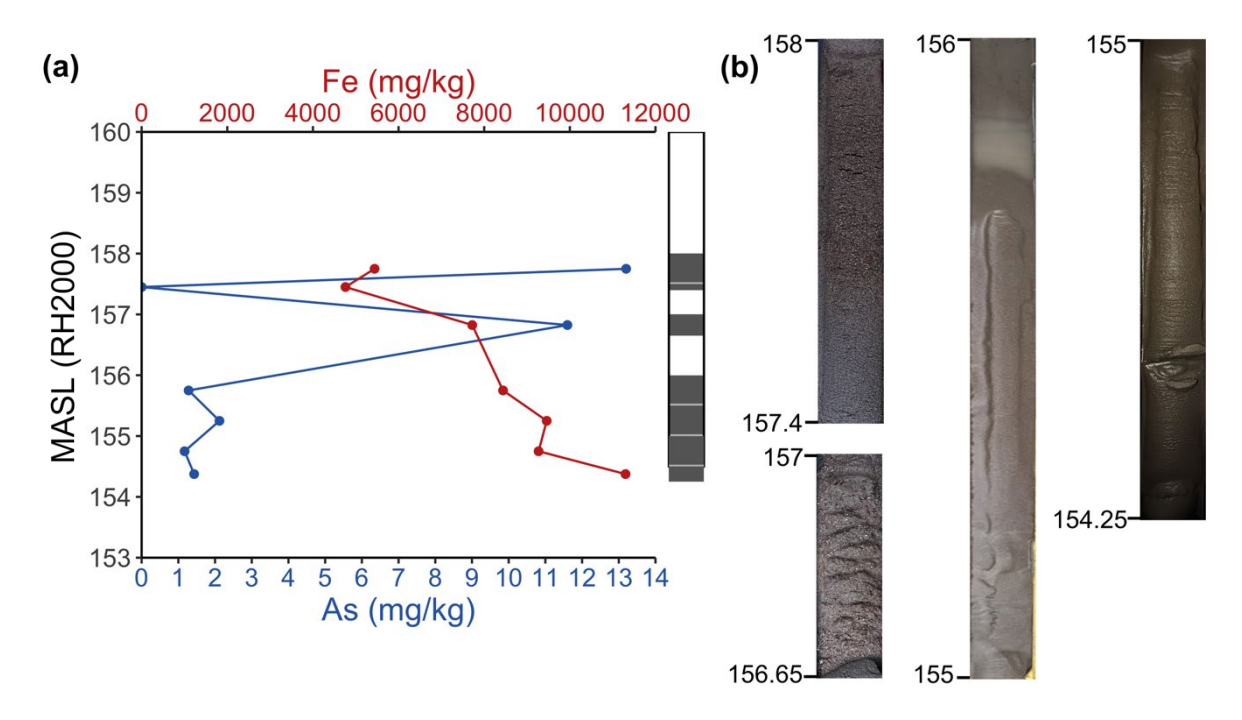


Figure 21. Soil profile for mZVI sampling point ms5 Fe and As results alongside images. Solid-phase Fe and As concentrations (a) and photos of successful samples with depth in meters above sea level (MASL) (b) are shown. The box to the right of the graph represents successfully collected samples in dark gray, and attempted sample collection as a black box. The last sample extracted more soil than expected, and runs deeper than the attempted sample depth.

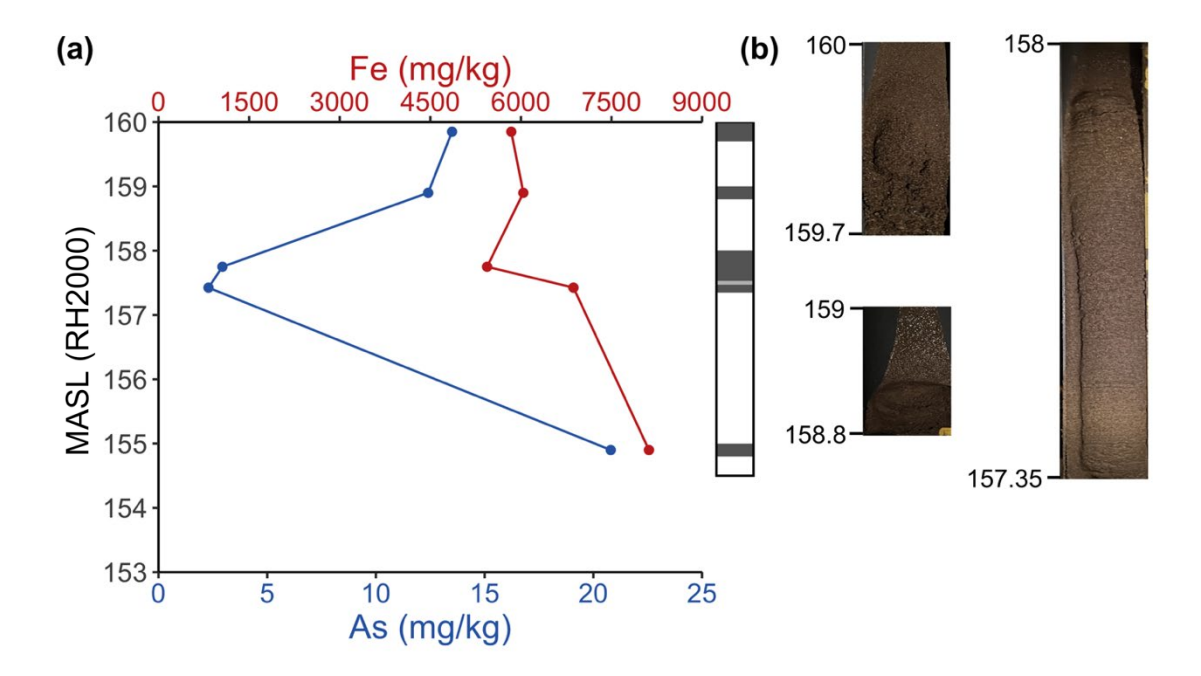


Figure 22. Soil profile for mZVI sampling point ms6 Fe and As results alongside images.. Solid-phase Fe and As concentrations (a) and photos of successful samples with depths in meters above sea level (MASL) (b) are shown. Box to the right of the graph represents successfully collected sa ples in dark gray, and attempted sample collection as a black box.

5.1.3 X-ray fluorescence measurements

XRF measurements were taken on-site to determine their reliability compared to lab analyses. For the mZVI points, only Fe was measured as As levels were below the limit of detection.

Measurements were taken directly on the soil core after extraction for points ms3 and ms4 of the mZVI plot, where Fe clumps were visible. Peaks in Fe content somewhat matched lab results. For point ms3 (Fig. 23a), there were 2 XRF peaks around 154.5 MASL, similar to the depth of an Fe peak in lab results. However, the largest peak from lab results was at 156.2 MASL; there was no corresponding peak from XRF results. Additionally, the XRF measurements showed a large peak at 159.4 MASL, where there was no high Fe content from lab results. The range was 20 times lower in XRF measurements than lab analyses (1700 mg kg⁻¹ compared to 25,000 mg kg⁻¹).

For point ms4 (Fig. 23b), there were again inconsistencies with Fe peaks. At around 153.5 MASL, 2 major peaks occurred, matching lab results. Here, the value was much higher than the lab results: 321,000 mg kg⁻¹, compared to a lab value of 54,200 mg kg⁻¹. However, the highest Fe content from lab results occurred at 154.8 MASL, where there was no corresponding Fe peak in the XRF measurements.

XRF measurements were also taken on all bagged samples that were later sent to ALS for lab analysis (Fig. 24). For the mZVI samples, most results matched lab sample Fe patterns reasonably well, with the exception of point ms5. However, ranges were much lower for XRF measurements than lab results.

Although XRF could give a rough indication of high Fe and As values, results were overall heterogeneous and unreliable.

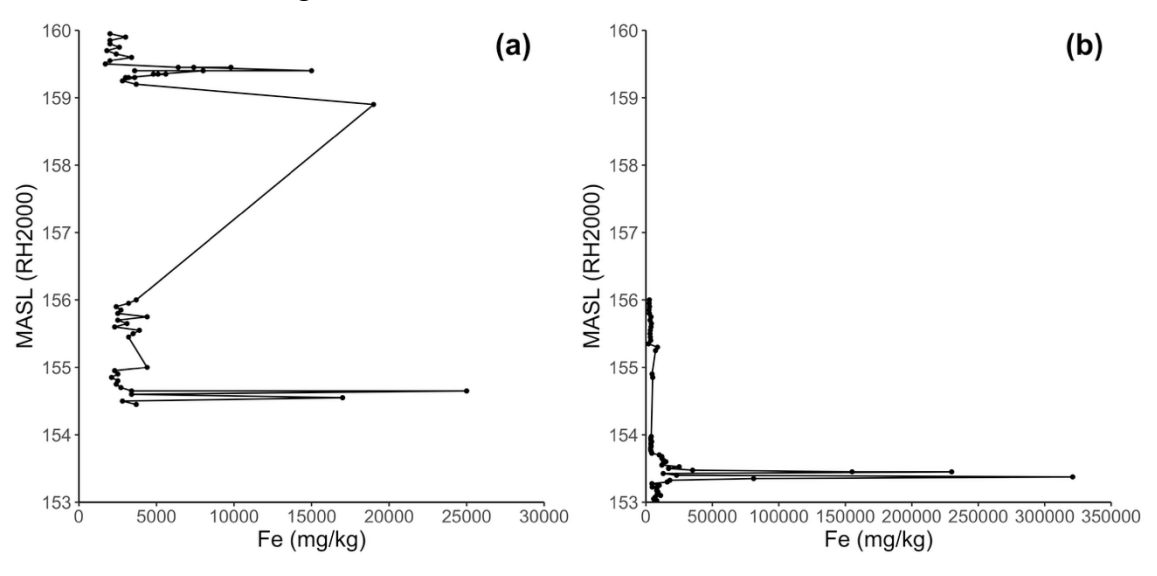


Figure 23. XRF measurements for solid-phase Fe for soil profiles ms3 (a) and ms4 (b) at the mZVI injection site. Depth is in meters above sea level (MASL). Profile ms3 is shown in more detail in Fig. 19 and ms4 in Fig. 20.

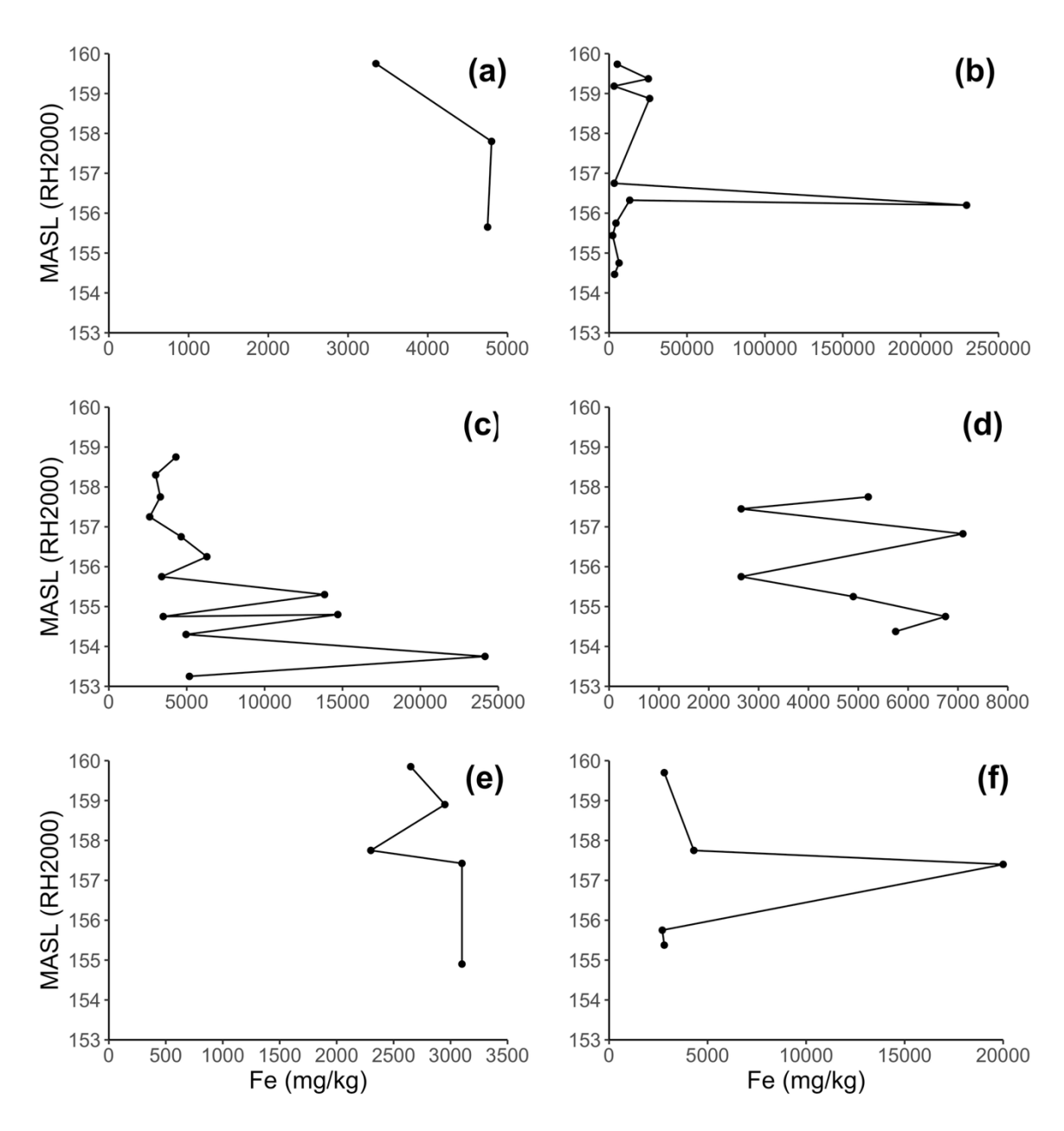


Figure 24. XRF measurements taken on mixed bulk samples for solid-phase Fe at all mZVI soil profiles. Two measurements were taken on each bag; an average of both is shown. Graphs (a-f) correspond to profiles ms1, ms3, ms4, ms5, ms6, and ms12, respectively. Depth is in meters above sea level (MASL).

5.2 nZVI treatment site

5.2.1 Groundwater

For nZVI, injection showed limited impact on As and groundwater conditions (Fig. 25). For 3 of the 4 sampling points, total As levels were consistent with the pattern before injection. The peak was between 161 and 159 MASL, with a range of $3240-4340 \mu g L^{-1}$. For ns4, however, there was a drop in total As at

160.5 MASL, from 1170 μ g L⁻¹ at 161 MASL to 689 μ g L⁻¹ at 160.5 MASL. It rose again to 1380 μ g L⁻¹ at 160 MASL. The range of percentage As(III) varied more than for mZVI. Excluding ns4, the range of As(III) was from 49% to 100%. Points ns1, ns2, and ns3 all show a drop in As(III) at 159 MASL to 50–60%. Point ns4 had a drop to 53% at 159.5 MASL.

Before injection, Eh near the nZVI injections showed a clear increase with depth. After injection, however, there was no clear pattern. The Eh ranged from -41.0 mV at 161 MASL to -16.6 mV at 158.5 MASL. Pre-injection, it ranged from 1.33 to -174.6 mV. Point ns4 showed a drop in Eh at upper levels (161–159.5 MASL), to a low of -273.1 mV at 161 MASL, consistent with the depth for the drop in total As. It did not, however, correspond with the depth at which percentage As(III) dropped. The pattern for pH also did not match pre-injection conditions and was at a slightly lower range than before. Barring point ns4, the range was an average of pH 6.62 at 161 MASL to pH 6.55 at 158.5 MASL. Previously, the pH went up to 7.28. As with mZVI, these Eh and pH values correspond with As(III) dominating in the groundwater (Fig. 26).

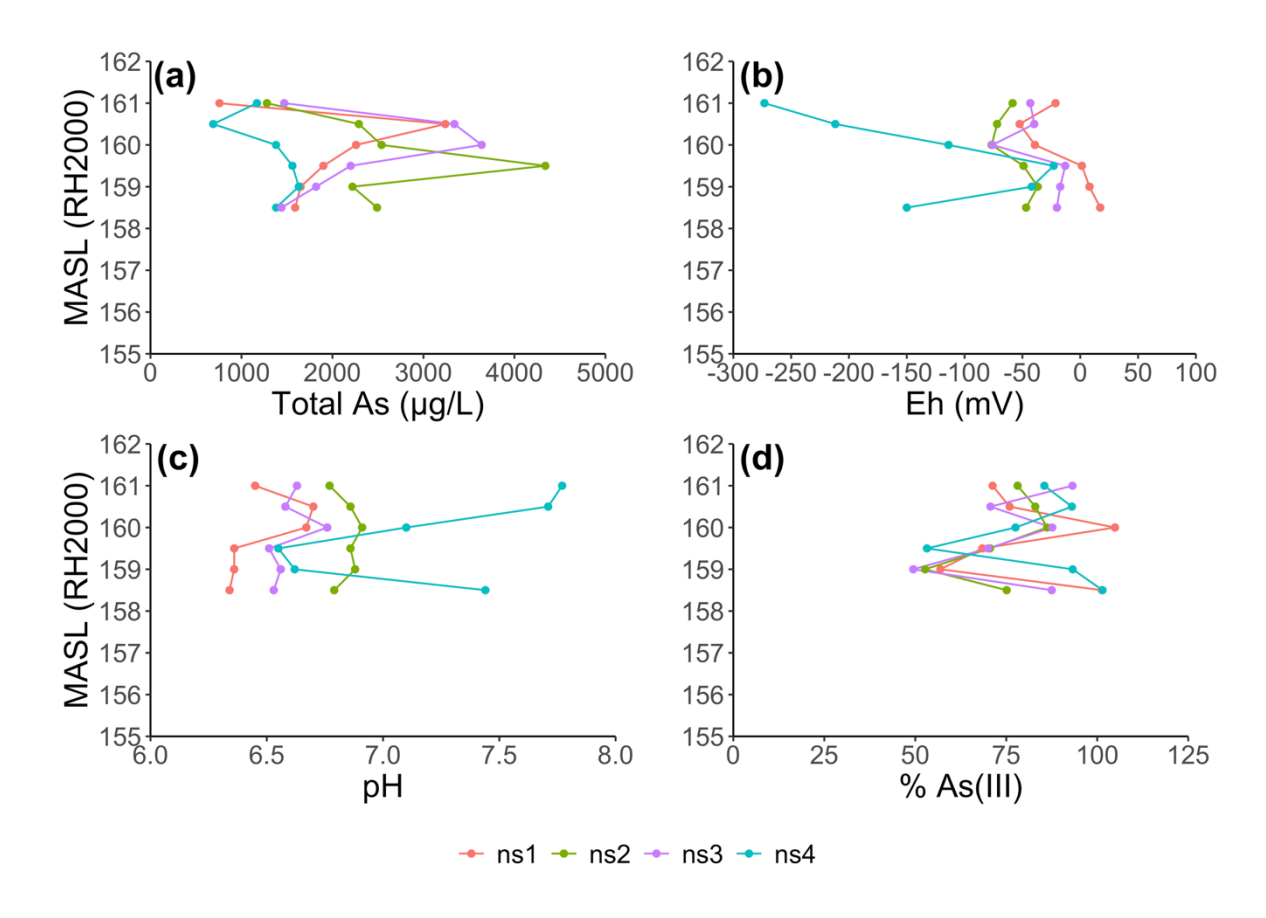


Figure 25. Total aqueous As (a), Eh (b), pH (c), and percentage As(III) (d) in the groundwater near nZVI injection point na4. Depth is in meters above sea level (MASL). Map of sample points is in Fig. 14. For comparison, pre-injection data is found in Fig. 9.

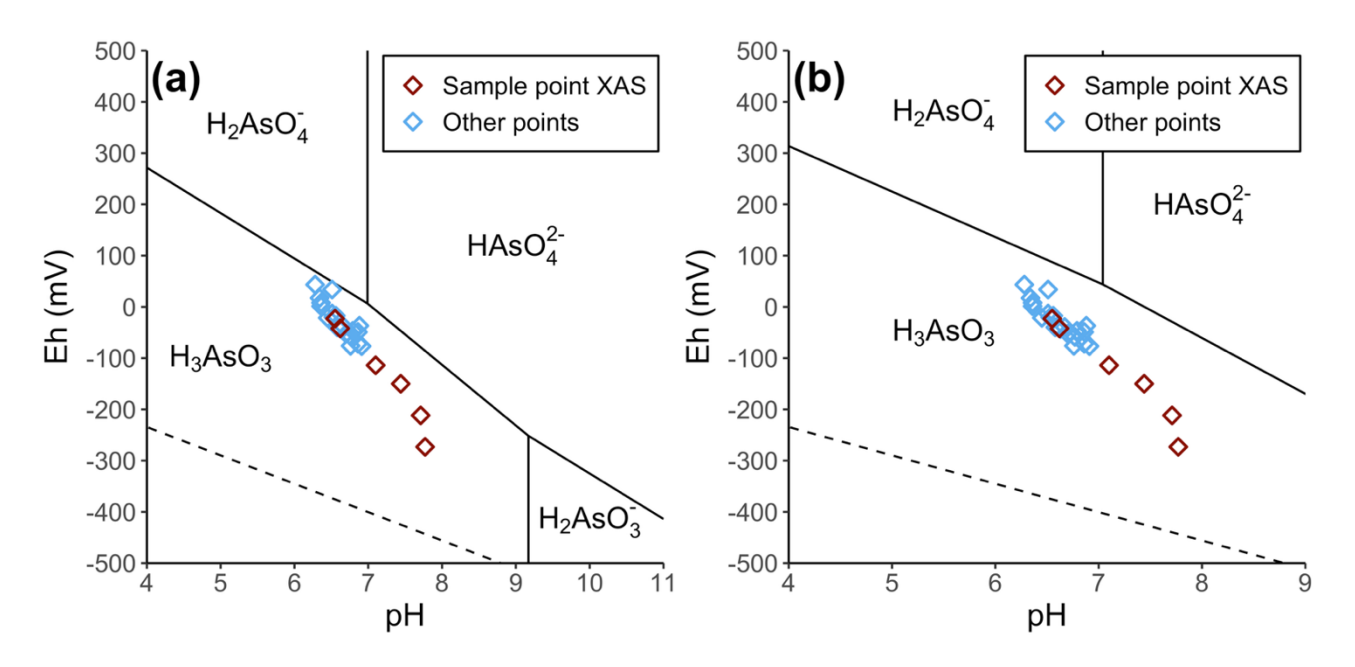
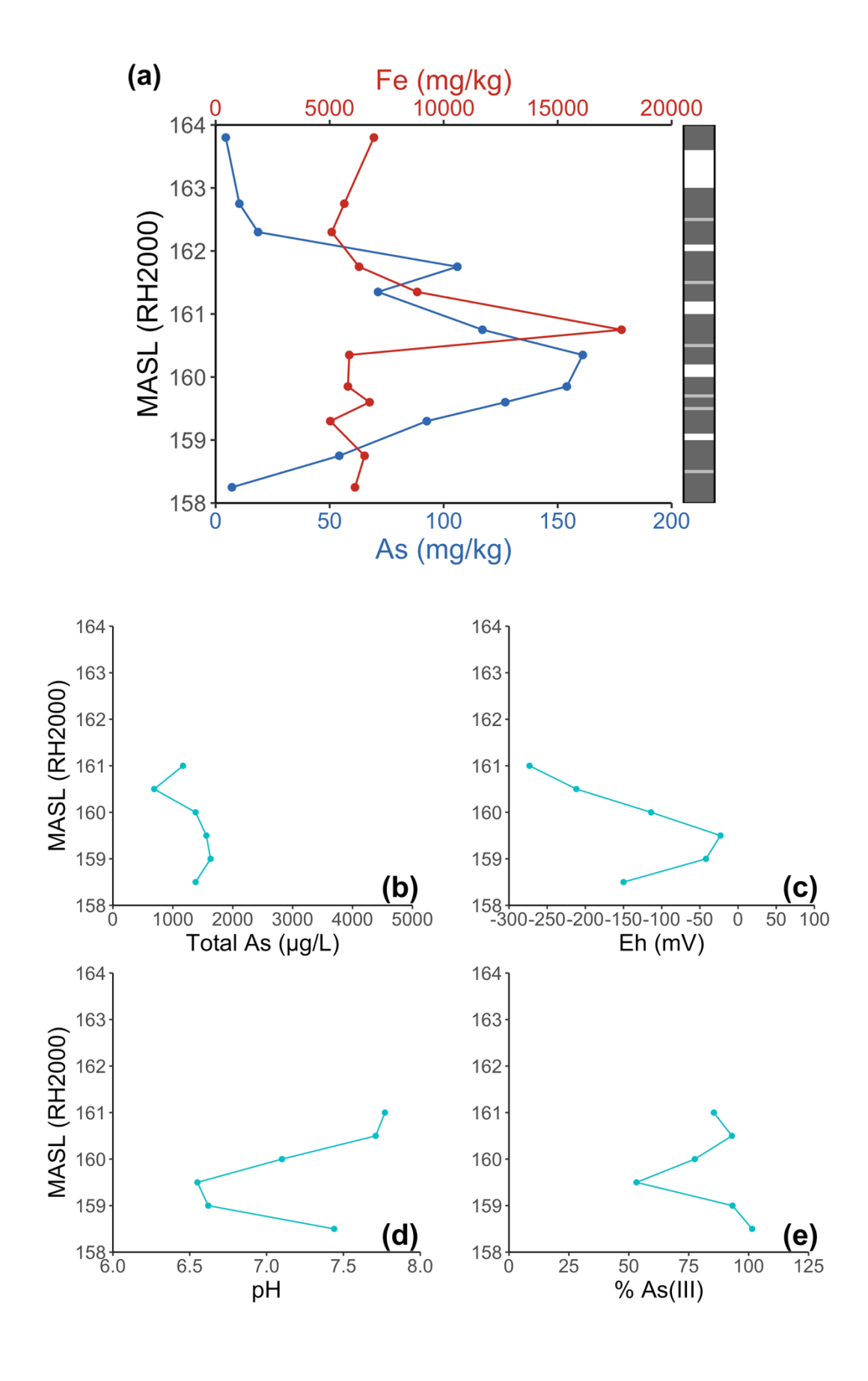


Figure 26. Pourbaix diagram for the distribution of aqueous As as either As(III) or As(V), overlayed with groundwater conditions from nZVI groundwater sampling. Red points represent groundwater samples that correspond to the soil profile (used for XAS). Graph (a) displays values at 25 °C—room temperature—and graph (b) at 6 °C, the average annual temperature of the aquifer. Stability lines were calculated using thermodynamic data from the database of Visual MINTEQ, vers. 3.1 (Gustafsson 2013).

5.2.2 Soil samples

After examining groundwater results, one soil core was taken at the nZVI site (Fig. 27), adjacent to sampling point ns4 where the groundwater conditions were impacted (Fig. 25). Solid-phase Fe ranged from 5040 to 17800 mg kg⁻¹, with a sharp peak between 161 and 160.5 MASL. Solid-phase As concentrations ranged from 4.42 mg kg⁻¹ at 161 MASL to a peak of 117 mg kg⁻¹ between 160.5 and 160.2 MASL. This peak corresponded with high levels of As in the groundwater. There was no correlation between solid-phase Fe and As.



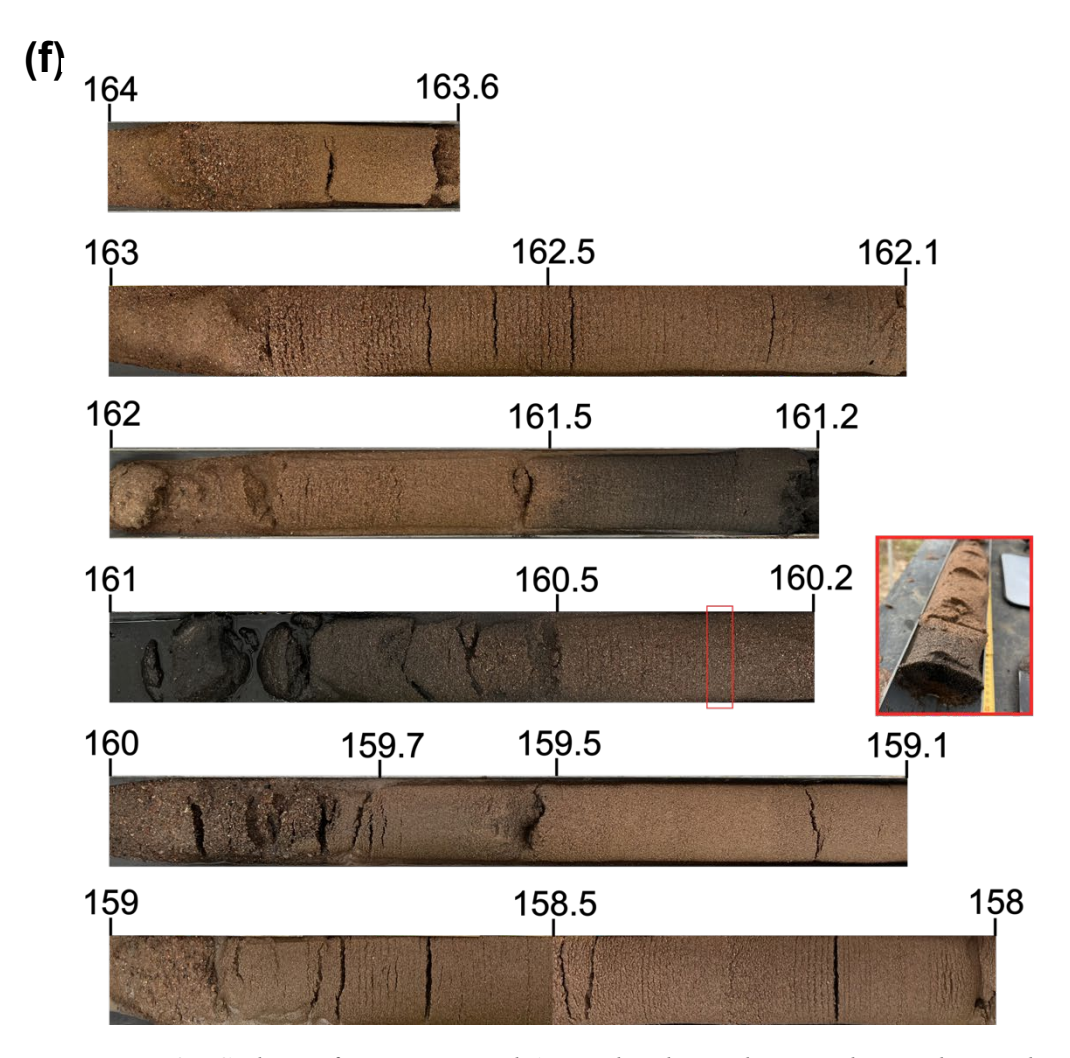


Figure 27. Soil core for nZVI Fe and As results alongside groundwater data and images. Graph (a) shows solid-phase Fe and As concentrations. The box to the right of the graph represents successfully collected samples in dark gray, and attempted sample collection as a black box. Groundwater results corresponding to the soil sample point for total aqueous As (b), Eh (c), pH (d), and % As(III) (e) are also shown for comparison. Images of successful cores with depths in meters above sea level (MASL) are represented in (f). The red box corresponds to a zoomed-in photo to the right of the main image.

5.2.3 X-ray fluorescence measurements

Because As levels were higher in the nZVI test zone than the mZVI one, here XRF measurements were documented for both Fe and As. For XRF measurements taken directly on the profile (Fig. 28), the Fe peak matched the lab one well: it occurred at 160.9 MASL, and the value was similar (19,100 mg kg⁻¹ for XRF; 17,800 mg kg⁻¹ in the lab). For As, the highest value occurred 1 m lower than in the lab results, but the value was also similar: 134 mg kg⁻¹, around 30 mg kg⁻¹ lower than the peak in the lab analysis.

Between the mZVI and nZVI data, XRF measurements taken directly on the core were heterogeneous and unreliable. The discrepancy between XRF and lab results likely arose from XRF's "information depth:" for Fe, 99% of the sample value is measured in the first 0.5 mm of the sample; for As, it is within the first mm (Laperche & Lemière 2020). If, for example, an Fe clump begins below 0.5 mm, XRF results will not reflect the increased Fe concentration. XRF is therefore more reliable in homogenous samples, and inapplicable in heterogeneous samples such as the ones taken directly on the soil cores in this study.

For the bagged nZVI samples (Fig. 29), Fe and As patterns were similar to the ones taken on the soil core. As with the mZVI results, Fe and As concentrations were low, but here not by a large amount (5600 mg kg⁻¹ lower for the highest Fe value, and 52 mg kg⁻¹ lower for the highest As value).

In the bagged samples, XRF measurements showed a strong correlation with ALS measurements for both Fe (Fig. 30) and As (Fig. 31). However, concentrations were very different. This correlation confirms the hypothesis that heterogeneity in the samples was the main cause of the discrepencies from samples taken directly on the core—bagged samples were homogenized.

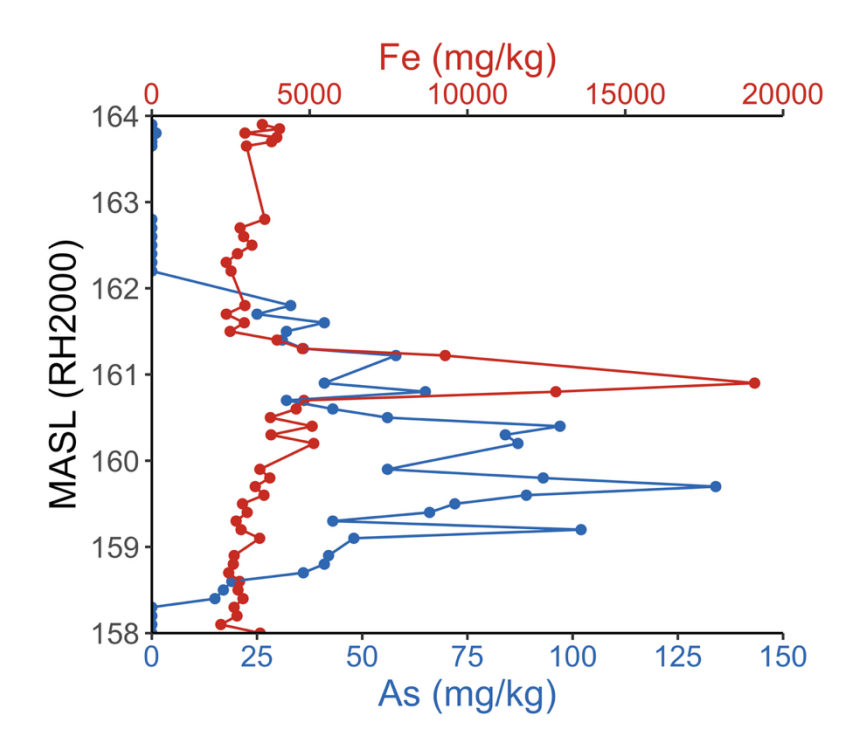


Figure 28. XRF measurements taken directly on the nZVI soil profile for solid-phase Fe and As. Depth is in meters above sea level (MASL).

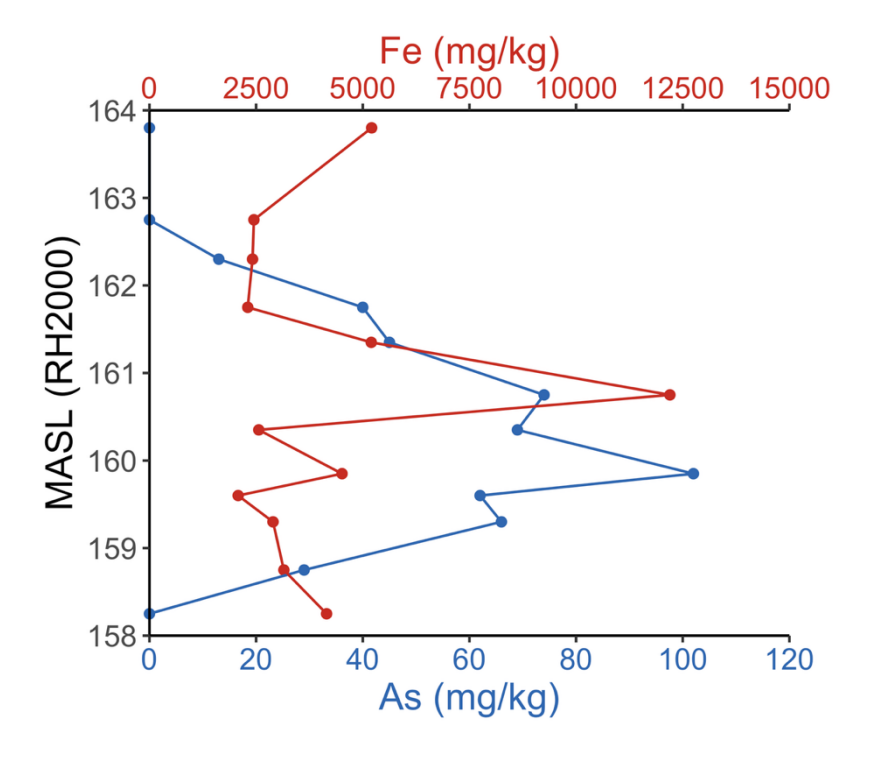


Figure 29. XRF measurements taken on mixed bulk samples for solid-phase Fe and As for the nZVI soil profile. Depth is in meters above sea level (MASL). Two measurements were taken on each bag; an average of both is shown.

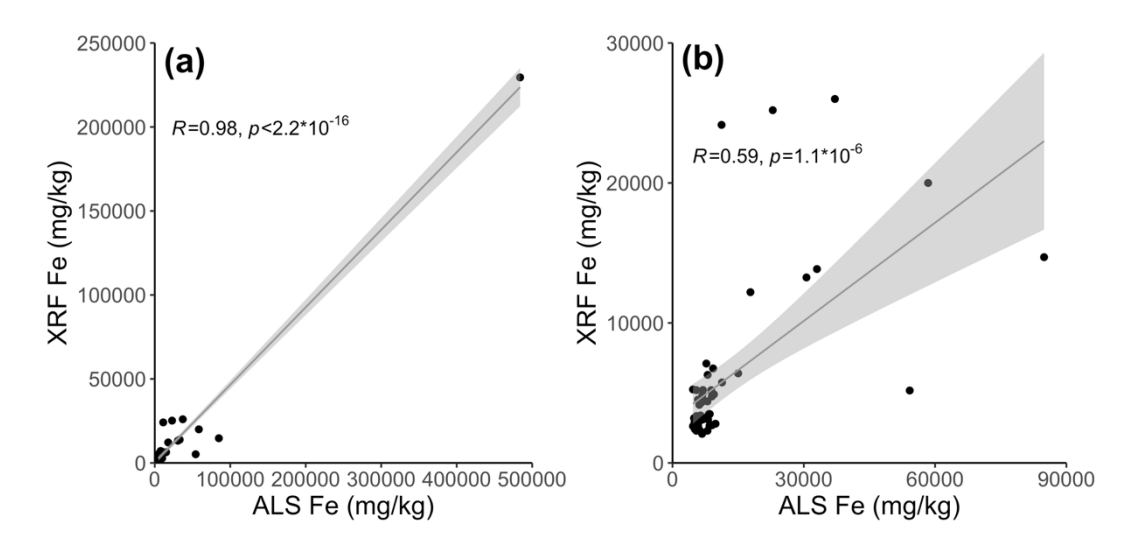


Figure 30. Correlation between ALS solid-phase Fe results and XRF solid-phase Fe measurements. Graph (a) shows all points, and graph (b) omits the high-value outlier. Both mZVI and nZVI measurements are depicted.

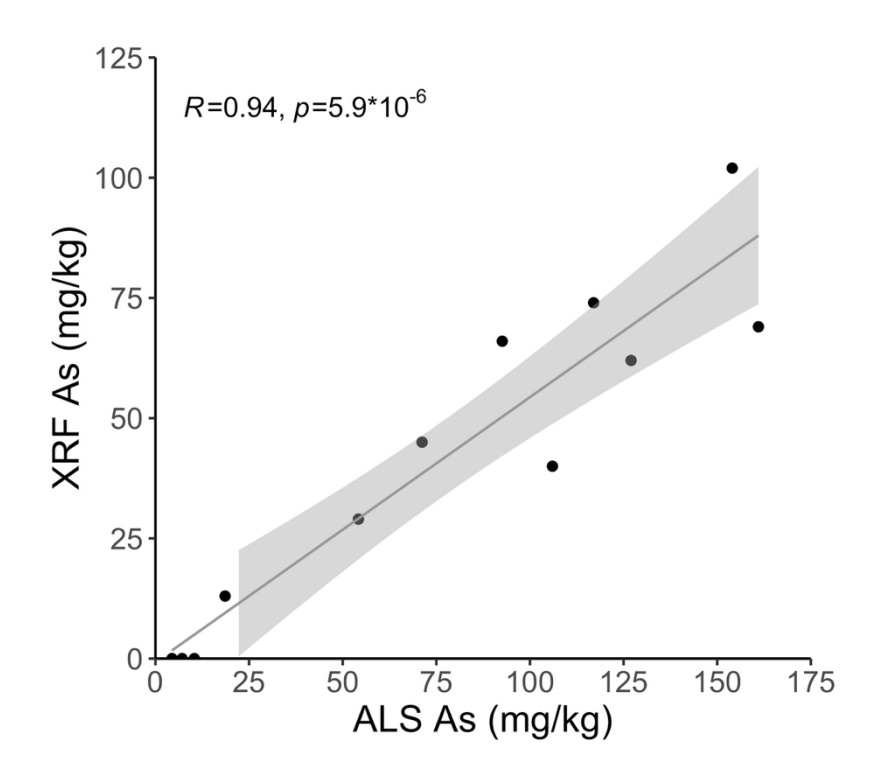


Figure 31. Correlation between ALS solid-phase As results and XRF solid-phase As measurements. Only nZVI values are shown, as As levels were below the detection limit for XRF at the mZVI site.

5.2.4 X-ray absorption spectroscopy

XANES measurements (only taken on the nZVI soil core) for As found As(V) bound to protoimogolite (PIM) and ferrihydrite (Fh), As(III) bound to PIM and Fh, As₂S₃ (orpiment), monothioarsenate (MTAs^V), As₄S₄ (realgar), and AsFeS (arsenopyrite) (Fig. 32, Fig. 33). PIM and Fh have similar white line intensities and are consequently not reliably separable with XAS. Therefore, combining the values of their fractional distributions represents a total percentage of Fe(III) minerals. These Fe(III) minerals could be either naturally occurring or produced by ZVI oxidation. Solid-phase As was primarily found as As(V) bound to these Fe(III) (hydr)oxides. Arsenopyrite was only found between 160 and 160.5 MASL, and orpiment at 158.5 MASL (Fig. 33).

According to Cao et al. 2023, there is a non-negligible level of S at this site (average 17 mg L⁻¹). When this concentration of S, along with Fe, is added to a stability diagram, nZVI groundwater conditions dictate the presence of orpiment and realgar (Fig. 36b). A similar As stability diagram is shown for mZVI (Fig. 35b), although it cannot be confirmed as XAS measurements were not taken. Arsenopyrite, however, is only found at a very high pH and low Eh (outside the range of Fig. 36b), and MTAs^V does not appear on the stability diagram.

Freeze-drying showed no clear effect on As speciation: total As(V) bound to PIM and Fh was not markedly different to total As(III) bound to these minerals with duplicate samples (Fig. 33).

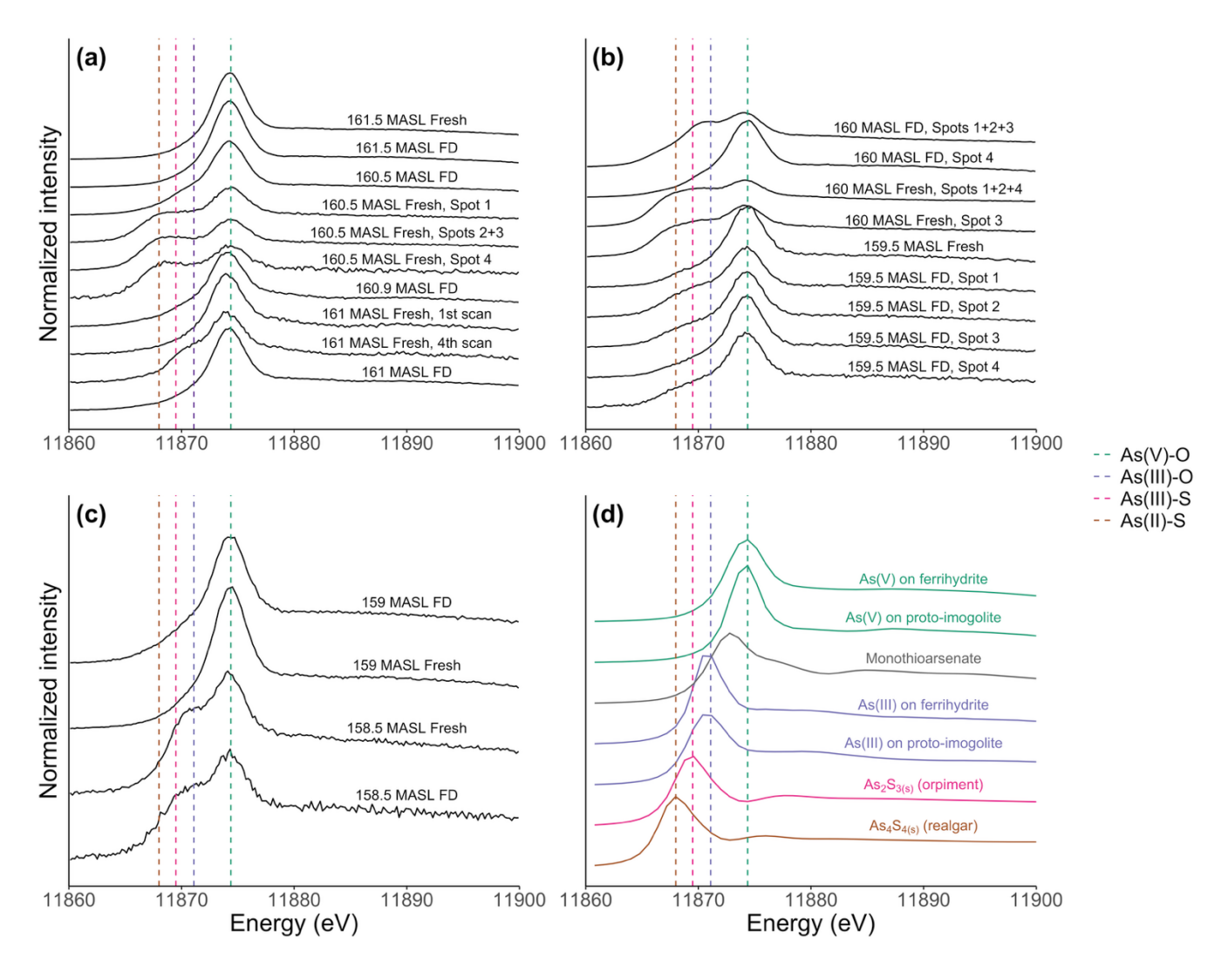


Figure 32. Normalized As K-edge XANES spectra for anoxic nZVI samples. Graphs (a,b,c) show results, by depth and sample, and (d) includes standards for reference. Relevant reference lines are included in each graph. Analysis conducted by Jon-Petter Gustafsson.

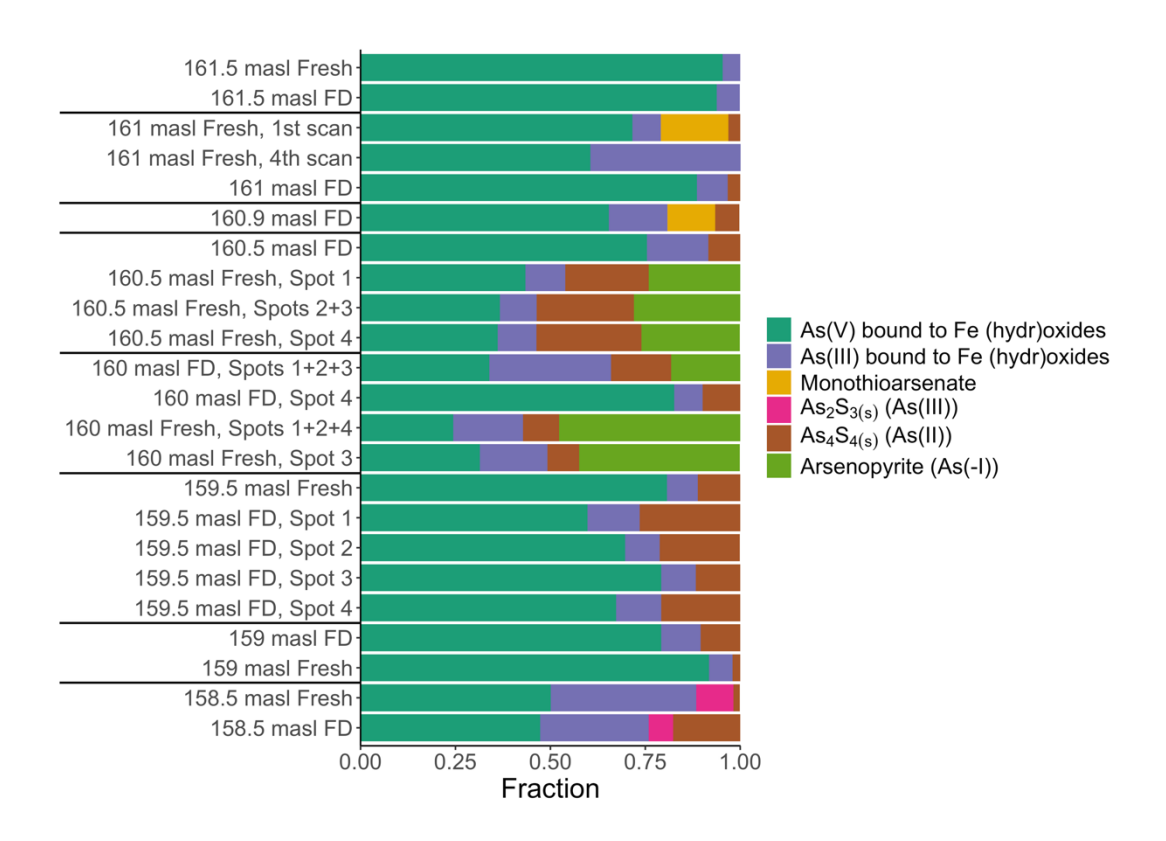


Figure 33. Fractional distribution of As species from XANES analyses, by depth in meters above sea level (MASL). LCF analysis conducted by Jon-Petter Gustafsson.

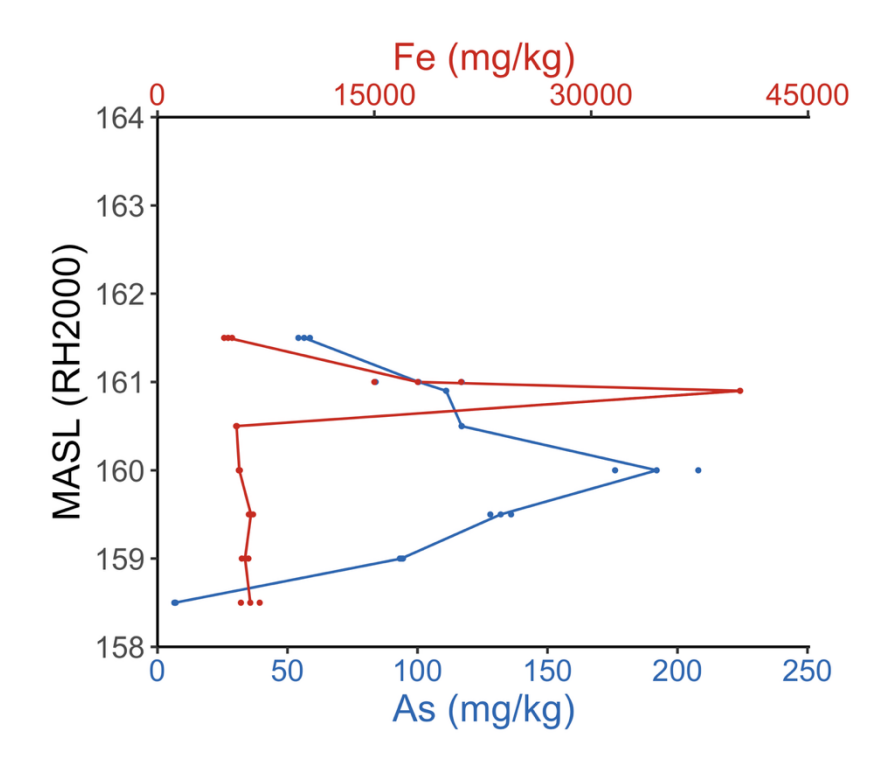


Figure 34. Fe and As solid-phase concentrations from anoxic samples used for XAS. Depth is in meters above sea level (MASL). Usually, 2 samples were taken per depth—both samples are plotted along with their average. The line connects the averages.

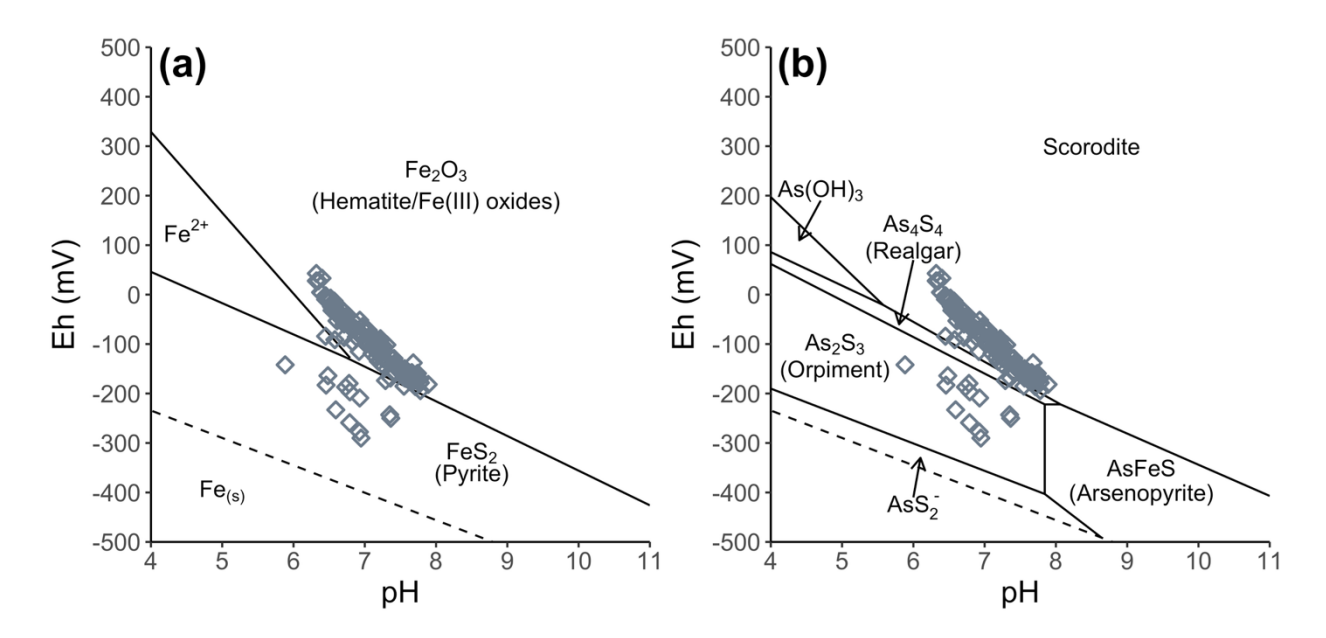


Figure 35. Pourbaix diagrams for Fe (a) and As (b) in the presence of S and As or Fe, respectively. Groundwater conditions for mZVI from groundwater sampling are overlayed. Stability is modeled at 6°C. Soluble Fe and As content are averages from mZVI groundwater samples (8.21 mg L^{-1} and 741.13 mg L^{-1} , respectively). Concentration of S is an average of the whole study site (17 mg L^{-1}), from Cao et al. 2023. Diagrams made in Geochemist's Workbench vers. 18 (Bethke 2022).

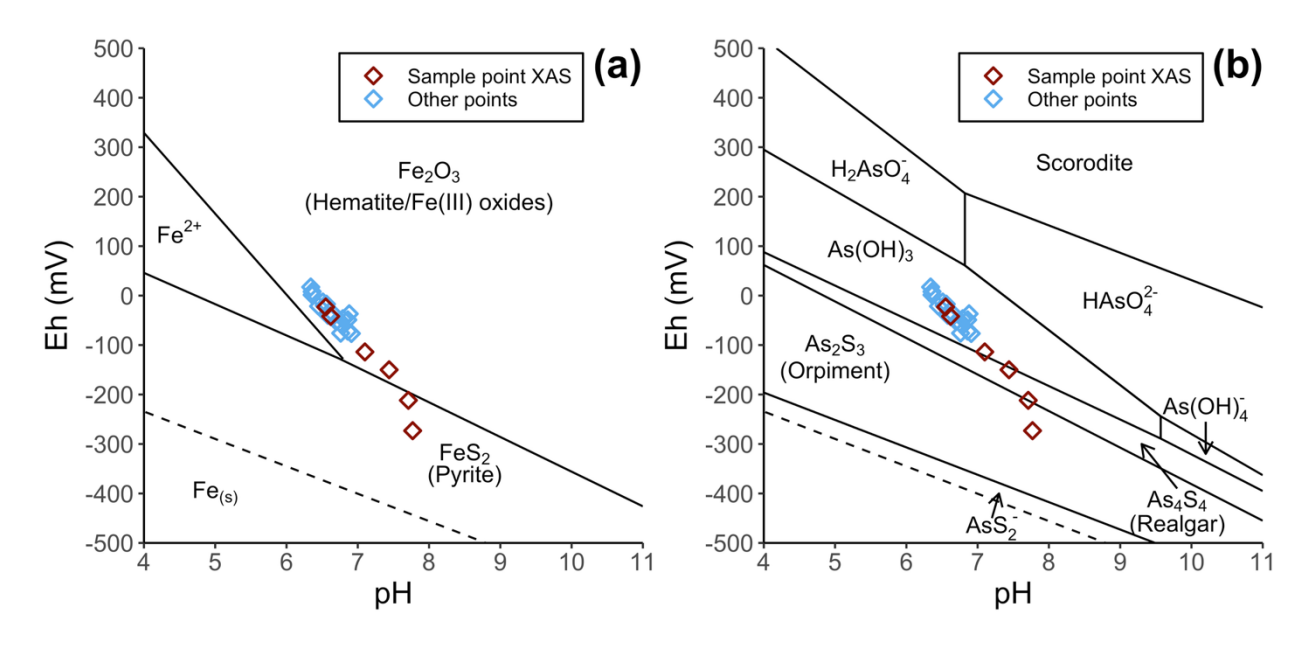


Figure 36. Pourbaix diagrams for Fe (a) and As (b) in the presence of S and As or Fe, respectively. Groundwater conditions for nZVI from groundwater sampling are overlayed. Red points represent groundwater samples that correspond to the soil profile (used for XAS). Stability is modeled at 6°C. Soluble Fe and As content are averages from nZVI groundwater samples (7.7 mg L^{-1} and 1857 mg L^{-1} , respectively). Concentration of S is an average of the whole study site (17 mg L^{-1} , from Cao et al. 2023. Diagrams made in Geochemist's Workbench vers. 18 (Bethke 2022).

XANES analyses for Fe showed a presence of Fe(III) (hydr)oxides, Fe(III)-organic, biotite, Fe(0), FeS, and FeS₂ (pyrite) (Fig. 37). Biotite, a naturally occurring Fe(II) mineral, was present in all but one sample, indicating high levels of Fe minerals naturally present at the site. Compared to other standards, biotite has a clear post-edge feature, making it very reliable for linear combination fitting (LCF). Fe(0) is a result of unoxidized ZVI, showing that ZVI did not fully oxidize after 2 years in the field. The highest fraction of Fe(0) is at 161 MASL, where there was the highest concentration of nZVI. Here, approximately 35% of the Fe content was Fe(0). Fe(0) was also found in deeper layers, ranging from 1.7% to 22.9% present in a sample, regardless of the presence of visible nZVI.

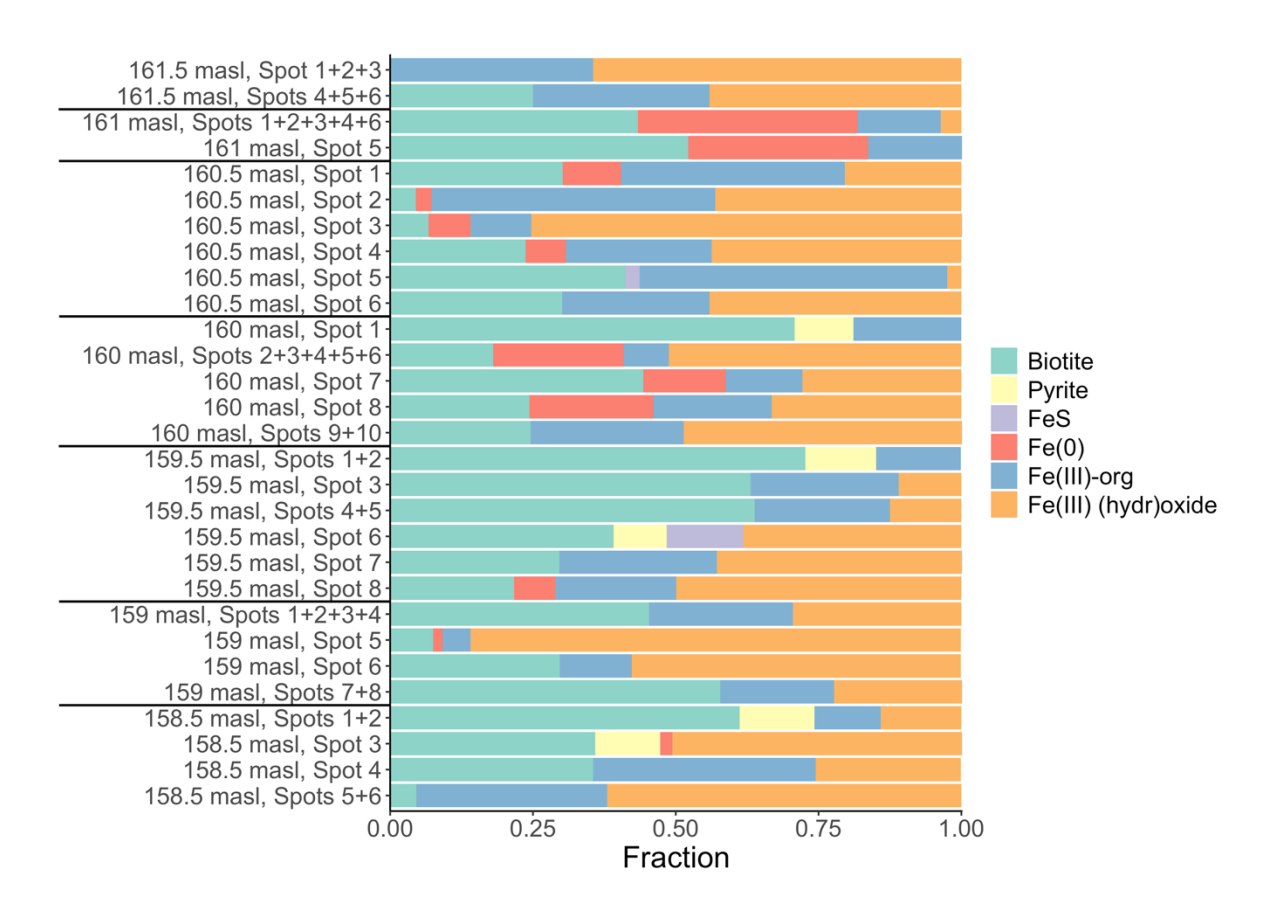


Figure 37. Fractional distribution of Fe species from XANES analyses, by depth in meters above sea level (MASL). LCF analysis conducted by Jon-Petter Gustafsson.

An Fe stability diagram with As and S concentrations factored in shows that Fe should be found as Fe(III) oxides, Fe²⁺, and pyrite for both mZVI (Fig. 35a) and nZVI (Fig. 36a).

An inverse correlation between fraction of biotite and total Fe can sometimes be used to show presence of ZVI: as total Fe increases, the biotite fraction decreases, showing the ZVI is dominating the total Fe distribution. Here, however, there was no correlation between biotite and total Fe (Appendix, Fig. 1).

Anoxic samples used in XAS were later sent to ALS for analysis of Fe and As concentrations (Fig. 34). The total Fe in these samples ranged from 5490 to 15,000 mg kg⁻¹, with a sharp increase in Fe at 161 MASL, as expected based on visible presence of black Fe and results from the larger soil core samples. Range of As concentrations were also similar in anoxic samples compared to bagged ones, although the highest peak was 50 cm below the bulk samples. The As ranged from 6.48 mg kg⁻¹ at 158.5 MASL to 208 mg kg⁻¹ at 160 MASL.

5.3 Column transport experiments with S-MicroZVI

For each flow speed, two replicates were conducted for column experiments. The first replicate showed evidence of cross-contamination between samples—there were clear remnants of Fe in the microwave tubes after digestion, despite best cleaning efforts (Appendix, Fig. 2). This contamination led to unexpected spikes in Fe for some of the resulting breakthrough curves (Appendix, Fig. 3). Additionally, digestion was not reliable, as flakes of undigested ZVI were sometimes visible after digestion in the microwave (Appendix, Fig. 2d), and the standard deviation of the difference between expected and measured Fe stock concentrations (C₀ expected – C₀ measured) after digestion was very high (the average was 830.76 mg L^{-1} with a standard deviation of ± 907.18 mg L^{-1}) (Appendix, Table 1). Some difference between expected and measured C₀ is expected, as the expected value was calculated based on the expected percentage Fe directly in the ZVI product (here, 40%), but the actual percentage after manufacturing likely varies. However, as all samples were taken from the same bottle of S-mZVI, the variation between samples should be minimal if digestion was successful. The recovery rate measured in the leachate fluctuated between 0.55 and 1.1%, with no clear pattern with flow speed. As these results show high levels of uncertainty, they are reported in the Appendix (Appendix, Table 2).

Information on recovery, porosity, dispersivity, and attachment coefficient for the second replicates, fitted by Hydrus 1D, are shown in Table 3. Overall, recoveries for the second set of replicates were very low, between 0.71 and 2.67%. As with the first set of replicates, there was no pattern related to flow speed. Bulk density, effective porosity, and dispersivity were fairly consistent across samples, averaging 1.88 (± 0.022) g cm⁻³, 35% (± 2.1), and 0.235 (± 0.055) cm, respectively. These consistent parameters indicate that there are no experimental artefacts from packing. Dispersivity for the 2.67 mL min⁻¹ sample was lower than the rest, at 0.16. Bulk density and effective porosity for this sample were consistent with the rest, so the change in dispersivity is likely from experimental error during the tracer test. Attachment rate (k) increased linearly with flow speed (Fig. 38), a result which is in line with previous column experiments on nZVI (Berggren Kleja et al. 2024). Digestion was overall more consistent than with the first set of replicates (Appendix, Table 1): for 3 of the 4

flow speeds, the average difference between expected and measured C_0 averaged 905.13 (± 71.1) mg L^{-1} of Fe. For the 2.67 mL min⁻¹ sample, however, the difference was much higher: 3695.77 mL min⁻¹. Whereas for the other samples the stock solution was pipetted into the microwave tubes directly after high-sheer mixing, the stock solution for this sample was taken 5 minutes after mixing due to experimental error. The S-mZVI had likely settled to the bottom of the beaker and changed the concentration of Fe pipetted from the stock solution. An average of the three other measured C_0 values was therefore used for modeling this sample.

Table 3. Numerical results for the second replicate of column experiments. Effective porosity, dispersivity, attachment coefficient, and S_{max} are all fitted by the Hydrus-1D model.

Flow speed (mL/min)	Bulk density (g/cm ³)	Recovery (%)	Effective porosity (%)	Dispersivity (cm)	Attachment coefficient (k) (min ⁻¹)	S _{max}
1.34	1.863	1.38	36	0.228	0.380	0.015
2.67	1.906	0.71	37	0.161	0.892	0.01
3.52	1.859	1.58	33	0.266	1.11	0.015
5.5	1.883	0.79	33	0.286	2.11	0.016
Average	1.878	1.12	35	0.235	1.123	0.014
Std. dev.	0.022	-	2.1	0.055	-	-

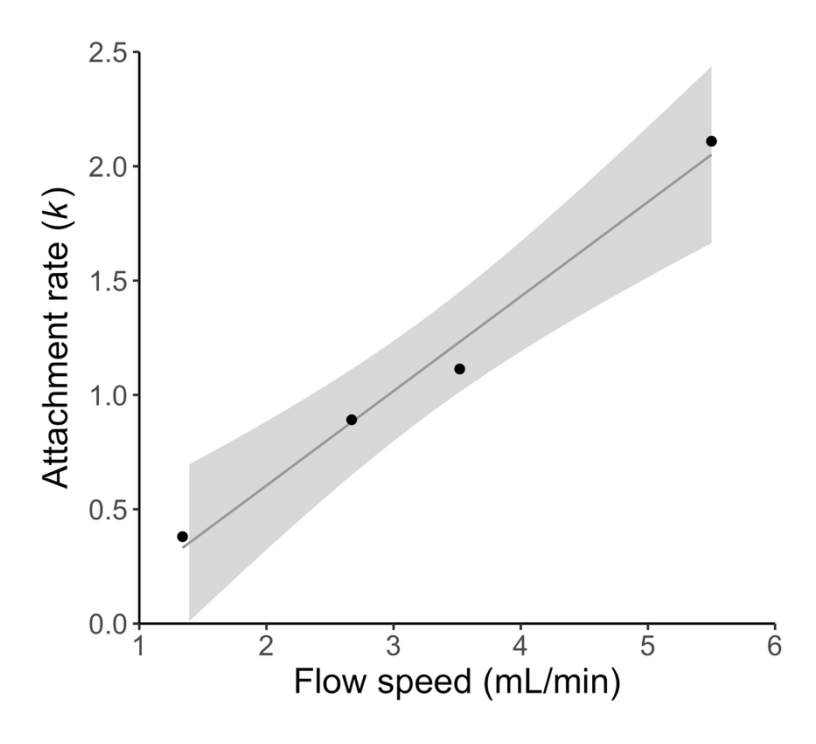


Figure 38. Attachment rate (k) at varying flow speeds. Results are only shown for the second batch of column experiments.

Breakthrough curves by Hydrus 1D for the tracer experiments were a good fit—the C/C_0 reached 0.5 at 1 PV, as expected, the peak was flat for 2 PV's where $C/C_0 = 1$, and there was minimal tailing (Appendix, Fig. 4). These results indicate reliable effective porosity and dispersivity values by the Hydrus model. However, breakthrough curves for the S-mZVI particles did not match well, as the arrival times in the model were earlier than the experimental values, and the overall peak shapes did not fit (Fig. 39a–d). Ideally, at 1 pore volume, the curve should have a C/C_0 value of 0.5. The experimental curves, though, were delayed, and did not reach 0.5 C/C_0 until much later. The k values achieved in this model, therefore, were not suitable for describing S-mZVI's behavior.

When blocking was included in the model, the shapes of the modeled curves matched better than without blocking (Fig. 39e–h) and S_{max} values were on the higher end of the given range (between 0.01 and 0.016 kg kg⁻¹) (Table 3), indicating a high influence from blocking on particle transport. Modeled curves, however, still showed breakthrough peaks much earlier than with observed values, possibly as a result of miscalculated dead time or exclusion of more complicated parameters (e.g. aggregation or deposition) in the model.

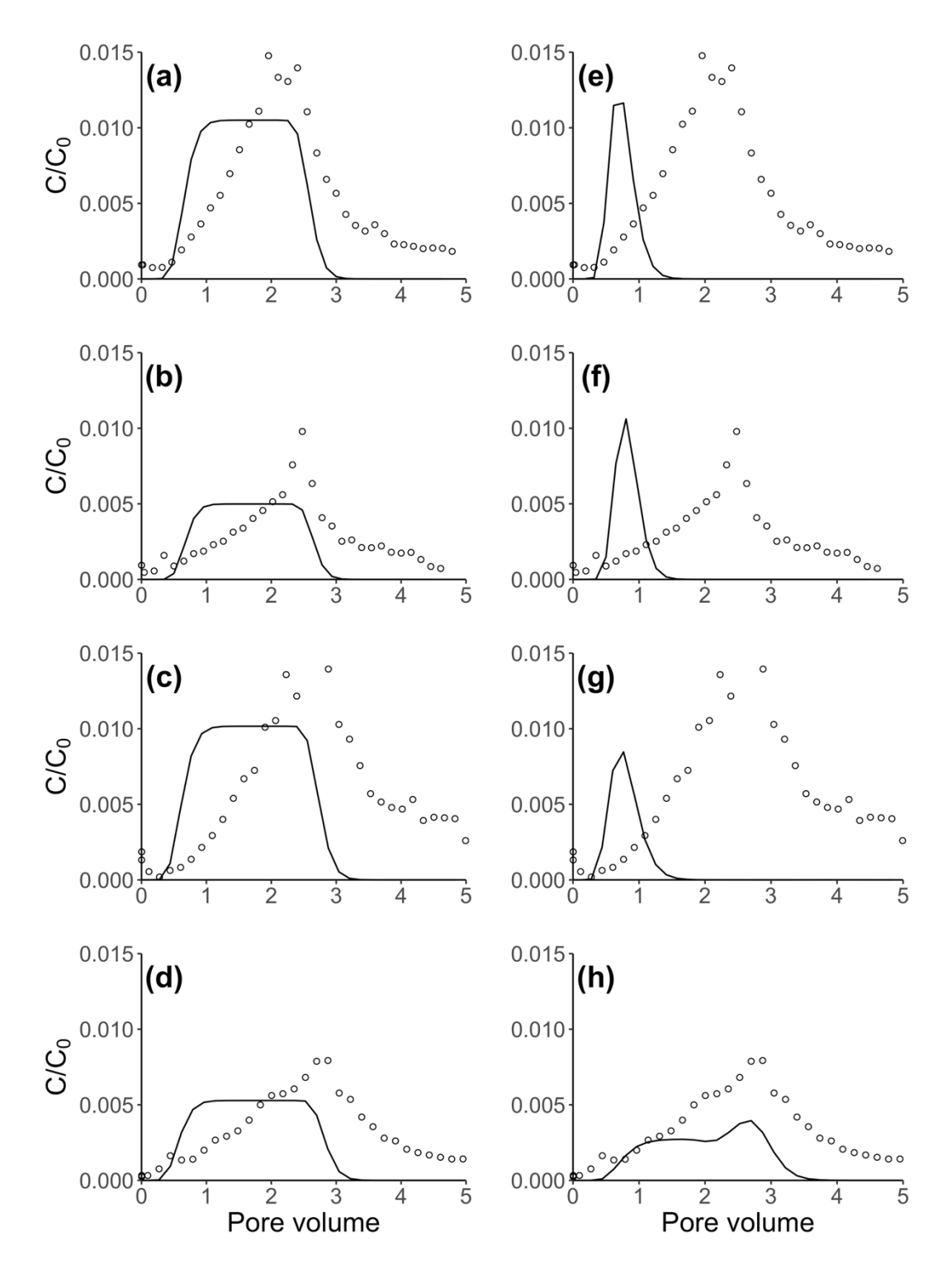


Figure 39. Breakthrough curves at varying flow speeds, both excluding blocking (a-d) and including blocking (e-h). From top to bottom, flow speeds are: 1.34, 2.67, 3.52, and 5.50 mL min⁻¹. Open circles are experimental values and continuous lines are modeled values.

6. Discussion

6.1 mZVI injection site

The mZVI plot showed strong evidence of narrow distribution and clumping. Clumps of Fe in soil profiles ms3 (Fig. 19) and ms4 (Fig. 20) provide visual evidence of heterogeneous distribution, and Fe peaks in lab analyses also indicate high ZVI aggregation. There is no control soil sample from before the injection, so it is difficult to say if the Fe concentrations in the other profiles were particularly high or a result of naturally occurring Fe. However, there was no visual evidence of mZVI; coupled with the lack of an effect on groundwater conditions, it is likely that mZVI did not spread to these sample points.

The main concern with colloid aggregation is the limited surface area for As binding. Unlike many other contaminants, As requires direct contact with ZVI for immobilization. It is therefore important to ensure that groundwater, contaminated with As, comes into direct contact with ZVI binding sites. As aggregation increases, the specific surface of ZVI decreases, limiting its immobilization potential. Heterogeneity also affects the diffusion of As to the ZVI surface, an important step for binding. For adsorption to occur, As must diffuse close to the ZVI particle surface: as groundwater flows through, a depletion zone is created near the ZVI, such that the concentration of As near the ZVI particles is smaller than the As concentration in the groundwater; As can then diffuse to the ZVI and bind. In a homogeneous distribution, the travel distance for As is, on average, shorter than in the presence of heterogeneously distributed ZVI. When ZVI is poorly distributed, the diffusion distance from As to ZVI binding sites is longer, so diffusion is slower, adsorption is slower, and overall immobilization decreases.

Points ms3 and ms4 showed a clear correlation in solid-phase Fe and As concentrations (Fig. 19, Fig. 20). These patterns were likely a result of a microenvironment created when mZVI was first injected, such that groundwater conditions changed sufficiently to bind some As to the outer surface of the aggregate. Because a low surface area was available, a small amount of As bound (a maximum of 18 mg kg⁻¹ for point ms3, compared to a mean groundwater concentration in the area of 1949 µg L⁻¹). As time passed, change in groundwater chemistry was not maintained, and groundwater flowing through returned to previous conditions. This hypothesis is further supported by the initial drop in As concentrations in well 1715_2, near points ms3 and ms4, the year after injection, only for it to increase again in 2024 (Fig. 11c). The chemistry, therefore, worked somewhat efficiently at first, but aggregation was a strong limiting factor, and there was overall only a very local effect on As concentrations in the groundwater.

Aggregation was likely primarily caused by high injection pressures. At high pressures, a fracturing injection can occur, where the injection pressure exceeds the porous medium's critical pressure, creating a non-uniform distribution of the product (Luna et al. 2015). The creation of preferential flow paths can be identified by a peak in the pressure record followed by a decrease to an (almost) constant value during injection (Velimirovic et al. 2014). The injection of mZVI occurred at very high pressures (up to 30 bar outflow) (Berggren Kleja et al. 2024). Pressures were especially high at lower depths, where high concentrations of Fe were later identified. Although a detailed injection pressure record over time was not recorded, drops in pressure to stable values were observed by on-site technicians (Sweco 2023, unpublished). Other field implementations of mZVI have had similar issues with high-pressure injections (Velimirovic et al. 2014; Flores Orozco et al. 2015; Luna et al. 2015). These studies, however, do not discuss aggregation effects, and mZVI was still effective in contaminant remediation. It is important to note, however, that the contaminants examined in these studies, unlike As, do not require direct contact with ZVI for effective remediation (instead, changing groundwater conditions are the dominating remediation pathway).

Other factors can also lead to aggregation. Low hydraulic conductivity, for example, can cause fracturing during injection (Luna et al. 2015). This site has quite low hydraulic conductivity values (for a sand sediment) at greater depths (up to a low of 4 m d⁻¹ at depth) (Cao et al. 2023) and could be a cause of fracturing at the mZVI site. Mechanical straining can also be an issue if the size of the Fe particles is greater than 0.8-1% of the grain size of the aquifer material (Luna et al. 2015). Even at shallow depths, mZVI (44 μ m) is larger than 1% of even the larger aquifer grain sizes: the average grain size in the upper layers of the mound (171–169.5 MASL) is an average of 500 μ m in diameter.

6.2 nZVI injection site

Unlike mZVI, nZVI did not have serious issues with clumping. Although there are peaks in total solid-phase Fe (Fig. 27a), and a clear high-Fe zone, Fe within that section was mixed with sediment (Fig. 27f), and therefore not an aggregate.

As nZVI was injected in the source zone, the correlation between solid-phase As and Fe is irrelevant. In the mZVI site, fresh water is constantly passing through the area; in the source zone, however, there is no influx of contaminated water. Instead, barring new contamination, the As profile stays roughly the same over time. The effects of nZVI can therefore be observed moreso through groundwater chemistry and binding mechanisms than through solid-phase As and Fe concentrations.

It is difficult to extrapolate why there were no groundwater chemistry changes for nZVI sampling points ns1, ns2, and ns3, where a soil sample was not taken. The point where a sample was taken, however, was well-distributed enough to have an impact on groundwater chemistry: where solid-phase Fe peaked, pH increased and Eh decreased in the groundwater (Fig. 27). Additionally, overall, total As concentrations were lower at this point than the three others (Fig. 25a), indicating that nZVI at this point had a significant impact on As immobilization.

Despite the lack of aggregation, nZVI was not necessarily well-distributed: it was more successfully spread in the upper layers of the aquifer, where hydraulic conductivity was higher, rather than lower layers where As concentrations were high and hydraulic conductivity was low. This limited distribution created a localized effect on groundwater conditions. The effect was therefore not visible across monitoring wells, as most monitoring wells had filter sections—where total aqueous As could be measured—below the nZVI section (they were installed here as these were the areas where groundwater As concentrations were highest). Of the wells monitored after injection, 1903 was the only one in the vicinity of the sampling site with a filter within the depth of the nZVI: the filter was installed from 161.2 to 157.2 MASL (Table 2), and the high nZVI concentration was found between 161 and 160.5 MASL (Fig. 27). As nZVI's effects were only concentrated in these shallow layers, other wells did not see any change in total As.

The limited distribution of nZVI could have been caused by a variety of factors. First, although nZVI was injected at much lower pressures than mZVI (up to 6 bar) (Berggren Kleja et al. 2024), pressure drops were nevertheless observed (Sweco 2023, unpublished). Additionally, Optimal Imaging Profiler (OIP) images showed the creation of 4–5 mm preferential flow channels after injection, indicating at least a small degree of fracturing (Sweco 2023, unpublished). However, it is most likely that this preferential distribution is a result of decreased hydraulic conductivity with depth. Pneumatic injection has been shown to improve nZVI mobility in the field compared to direct injection (Su et al. 2013). A different injection technique, therefore, could be used at this site for future studies, in order to reduce likelihood of preferential paths. Outside of hydraulic conductivity, nZVI could have poor mobility due to attachment between particles and sand grains, as was demonstrated by nZVI's irreversible attachment in previous column tests (Berggren Kleja et al. 2024).

Both batch and column tests in the lab did not reflect distribution problems observed in the field. Batch tests occur in an aqueous solution and are constantly shaken. Compared to field conditions, there is significantly less interaction between colloids themselves and between colloids and collector particles—aggregation is therefore not typically observed. Berggren Kleja et al. 2024's column tests studying nZVI mobility showed promising preliminary results.

However, the high pressures used in the field were not applied in the column tests, and the columns were densely packed and homogeneous, minimizing the possibility of preferential flow. Additionally, aggregation typically does not occur fast enough to be observed in column experiments; the influence of aggregation and settling on prediction of nZVI sticking efficiency in models increases with increased injection period (Kocur et al. 2013). As these column experiments were conducted over just a few hours, particles did not have time to settle and aggregate. Most importantly, changing hydraulic conductivity with depth was not reflected in the column experiments.

6.3 ZVI reaction mechanisms in the field compared to the lab

6.3.1 Differing groundwater conditions

Groundwater conditions, such as redox potential, pH, and ionic strength, affect the interactions between ZVI and As. Here, groundwater conditions in the field were more reducing than in the lab. Previous measurements at this site found that redox potential at the study site ranged from -270 to 260 mV, varying both spatially and temporally (Cao et al. 2023). Groundwater samples from this study, therefore, were not out of the ordinary, but were on the lower end of the range (-290 to 42.7 mV, with a median of -102.5 mV). In contrast, previous batch tests by Formentini et al. 2024 were conducted at an Eh of around 0 mV before adding ZVI, based on redox potential of the groundwater at the soil sampling point taken for lab experiments. Having such a low Eh in the field hinders the oxidation of As(III) to As(V). As a result of reducing conditions, As speciation dominated as As(III) in all groundwater samples taken in this current study (Fig. 17, Fig. 26), and As(V) was not formed to bind to ZVI and immobilize. Goethite and lepidocrocite have been shown to bind As(III) without oxidation (Manning et al. 2002), but XAS results did not show evidence of these minerals, and they were likely rare.

In this study, the median pH was 7.1, within the pH range of previous measurements at this site (5.7 to 7.3) (Cao et al. 2023). Formentini et al. 2024 accounted for pH buffering in the second half of their study, lowering it to pH 7. Eh buffering, however, was not considered.

Heterogeneity in groundwater conditions can dictate varying concentrations of As in the groundwater across a site, as changes in, for example, Eh and pH affect As adsorption to minerals and organic matter (OM) in the soil. The Eh and pH of this site appear to be quite heterogeneous. A possible explanation for these fluctuations is the distribution of OM and Fe (hydr)oxides. The site is characterized by a high presence of OM, which is naturally heterogeneously distributed, both due to heterogeneity of the OM input and heterogeneous

distribution of particulate OM based on pore size distribution. Therefore, higher levels of OM in some areas will create highly localized reducing conditions where OM is present. Additionally, in podzols (the dominating soil type at this site), dissolved OM is transferred vertically during soil formation, from the OM-rich surface horizon down to lower depths. As a result, OM can also be enriched in the lower spodic horizon. Additionally, Al³⁺ and Fe³⁺ ions are also highly concentrated in podzols. When, under less reducing conditions, OM comes into contact with these ions, they can form complexes that further affect groundwater conditions depending on local mineralogy. Under anoxic conditions, Fe³⁺ can be reduced to Fe²⁺, aided by OM (Appendix, Equation 1) (Driessen et al. 2001):

$$CH_2O + 4Fe(OH)_3 + 7H^+ \rightleftharpoons 4Fe^{2+} + HCO_3^- + 10H_2O$$
 (10)

where CH₂O represents OM. (In more reducing conditions, this reaction would occur with goethtite (FeOOH) rather than ferrihydrite as shown above (Cao et al. 2023).) The reduction and oxidation of Fe³⁺ and Fe²⁺ buffers both pH and Eh, creating areas with higher pH and Eh than expected based solely on the presence of OM. The variable distribution of OM and Al and Fe at this site therefore leads to large spatial and temporal pH and Eh variations.

6.3.2 XAS binding mechanisms

Overall, solid-phase As was found primarily as As(V) bound to Fe(III) (hydr)oxides outside of the high-concentration nZVI zone (Fig. 33). At the depth where fraction of As(III) levels dropped in the groundwater samples (159.5 MASL), As(V) bound to Fe(III) hydroxides still dominated. Fe (hydr)oxides are ZVI corrosion products, so it it is unclear if this drop occurred due to presence of ZVI or naturally high levels of Fe (hydr)oxides, as there was no control for background Fe levels. Indeed, the control sample, with no ZVI, in batch tests showed As(V) bound to Fe (hydr)oxides in the solid phase and As(III) prevailing in the solution phase (Formentini et al. 2024).

Concentrations of biotite, a naturally occurring mineral that is not a ZVI corrosion product, were high across sampling depths (Fig. 37), indicating high background levels of Fe in the soil. Additionally, the lack of a correlation between fraction of biotite and total Fe in XAS results (Appendix, Fig. 1) causes difficulties extrapolating where nZVI corrosion products are present over naturally occurring Fe minerals. If the fraction of biotite and total Fe showed a negative correlation, it would indicate that nZVI corrosion products are dominating the total Fe present in the sample. This issue likely arose from small beam size, and thus high spatial resolution, as is evident from different speciation between spots even within the same beam sample. The purpose of using a small

beam size was to give an indication of binding mechanisms on a particle scale, rather than overall distribution of Fe mineralogy and speciation. This decision means, however, that it is difficult to correlate Fe concentrations with fractions of different minerals. As a result, XAS results were very heterogeneous and could not give an indication of the presence of nZVI, or its corrosion products, in the bulk sample. Although the presence of nZVI corrosion products cannot be determined, these results still give an indication of As binding mechanisms.

Unlike Formentini et al. 2024's lab studies, field results showed that reducing conditions and S played important roles in As binding mechanisms. XAS analyses showed the presence of MTAs^V, As₄S_{4(s)} (As(II)), and AsFeS (arsenopyrite) (As(-I)). The average S concentration at this site is 17 mg L⁻¹ (Cao et al. 2023), large enough to affect expected As speciation in stability diagrams (Fig. 35b, 36b). Although MTAs^V does not appear in the stability diagram, it has been found to play an important role in As cycling when S and Fe or Al are present; it can even negatively impact As(V) sorption on minerals (Shan et al. 2021). Presence of S can also lead to more reduced forms of As than As(III). Under oxidizing conditions, S dominates as S⁶⁺ in SO₄²⁻; under reducing conditions, S occurs as S²⁻ in the form of HS⁻ and H₂S. S²⁻ can react with As(III) to create the even more reduced forms of As seen in the XAS results. For example, arsenopyrite can form from HS⁻ and H₃AsO₃ via:

$$H_3AsO_3 + 2H^+ + Fe^{2+} + HS^- + 3e^- \rightleftharpoons 3H_2O + FeAsS$$
 (11)

These findings are supported by previous studies, where S²⁻ has been found to react with both Fe and As, removing As from solution. For example, 10% of nZVI, in the presence of S²⁻, has been found to convert to FeS within 24 hours under anoxic conditions (Fan et al. 2013). Under low-temperature, reducing conditions, S²⁻ can also remove dissolved As from solution by forming realgar-like AsS. In the presence of Fe, arsenopyrite can also form. Precipitation rate, however, is important: if precipitation rates are too fast, only FeS will form, removing S from solution without affecting dissolved As concentrations (O'Day et al. 2004).

According to both Fe and As stability diagrams in the presence of S (Fig. 36), pyrite, realgar, and orpiment should dominate at this point, mostly matching XAS results. As these are all solid minerals, they would remove As from solution (with the exception of pyrite). According to XAS results, arsenopyrite was also present. In fact, arsenopyrite concentrations were especially high in samples taken at 160.5–160 MASL (Fig. 33), coinciding with the drop in total As in the groundwater (160.5 MASL) (Fig. 27b), indicating that this mechanism could be a significant removal pathway for dissolved As. At these points, ZVI modified groundwater conditions (pH increased and Eh decreased), although weaker than at

shallower depths. It is therefore possible that the effect on total As is not solely attributed to ZVI, and other factors, such as local mineralogy or presence of organic matter, could have contributed to changing As concentrations at this depth. According to the stability diagram, however, arsenopyrite should only be present at very high pH and low Eh values (outside of the range of Fig. 36b). It is possible that arsenopyrite was created as an effect of conditions at the nZVI surface, where groundwater changes occurred on a very local scale that was not reflected in the bulk solution—after all, XAS results from this point were heterogeneous, and some showed no presence of arsenopyrite. If arsenopyrite presence is very local, it is thus not a particularly important process for As immobilization. Fluctuating concentrations of As could also explain arsenopyrite presence, as they significantly alter the stability diagrams. For example, As levels were much lower at the mZVI injection site than the source zone where nZVI was injected; as a result, the As stability diagram, in the presence of similar S and Fe concentrations as nZVI, is quite different (Fig. 35b). Here, arsenopyrite would not be an unlikely mineral present. However, this effect also implies that arsenopyrite is not a strong long-term immobilization factor, as fluctuating concentrations would cause dissolution of the mineral and the release of As back into the groundwater. It is also, again, hard to say if these binding mechanisms were from ZVI or naturally occurring minerals. However, because ZVI was likely the cause of the changing groundwater conditions at this depth that could lead to arsenopyrite or realgar formation (through a drop in Eh), these results provide further proof that ZVI had an effect on As removal from groundwater, although the mechanism in question differed from lab results. It is also important to note that LCF results for arsenopyrite were quite unreliable compared to other measurements. If arsenopyrite is removed from the LCF fits, realgar dominates as a binding mechanism. Nevertheless, a high presence of realgar essentially provides the same results—S played an important role in immobilizing As, and As speciation was more reducing than expected based on lab results.

Quite a high proportion of unoxidized nZVI, as Fe(0), was found throughout the soil profile (Fig. 37; Appendix, Table 4), especially in areas where there was visible nZVI in the soil cores and peaks in total solid-phase Fe (Fig. 27a). It is possible that much of the mZVI had not oxidized by this point—it has a low surface area to volume ratio, and 36% of mZVI remained as Fe(0) after 30 days of shaking in batch tests (Table 1). The addition of guar gum can also initially hinder mZVI's reactivity, although it can be quickly degraded by soil microbes and overall has a limited effect on mZVI oxidation (Velimirovic et al. 2012, 2014). Additionally, aggregates in the mZVI soil samples would have restricted the inner part of the clumps' exposure to water, preventing oxidation. However, nZVI is highly reactive—in batch tests, only 4% of unoxidized nZVI remained after 30

days even under anoxic conditions (Table 1). After 2 years in the field, it is somewhat surprising that nZVI had not fully oxidized.

If field conditions were more reducing and/or at a lower pH, the presence of Fe(0) could be explained by thermodynamic stability. Groundwater conditions at this site, however, do not lie close to the presence of metallic Fe on a stability diagram (Fig. 36a)—groundwater conditions are therefore not a contributing factor.

Low temperatures could have been a limiting factor. Lab experiments were all conducted at 25°C. This aquifer, however, is at roughly 6°C on average. Low temperatures could have slowed down nZVI corrosion, constraining its immobilization potential. Kim & Cha 2021 examined ZVI corrosion in anoxic conditions under three temperatures: 25°C, 10°C, and 3.5°C, and found that colder temperatures led to lower concentrations of ZVI corrosion products. At 10°C, 35% of the 25°C value of nZVI remained, and at 3.5°C it dropped to 25% of the 25°C value. At the same time, difference between temperatures substantially decreased in the presence of bacteria compared to abiotic conditions (nZVI at 10°C was 77% of the 25°C value, and 3.5°C was 62% of the 25°C value). On top of slow corrosion, low temperature leads to more favorable conditions for As(III) over As(V) in groundwater (Fig. 17, Fig. 25). Indeed, As removal by ZVI has been shown to greatly decrease at 20°C compared to 40°C (Tyrovola et al. 2006).

6.4 S-microZVI recovery and mobility

Low recovery rates, of <2%, in the leachates were observed for all flow speeds (Table 3), demonstrating limited mobility of S-mZVI, therefore indicating a poor distribution in the field. For comparison, column experiments of nZVI, which later showed limited field mobility, had recovery rates of over 3% for all flow speeds (Berggren Kleja et al. 2024). Low recovery of S-mZVI could partly be due to experimental error. Despite high-sheer mixing right before injection, S-mZVI sedimented quickly in the mixed solution. As a result, the concentration of S-mZVI pumped through the column could have decreased over time. Sedimentation was visibly observed when cleaning the ZVI stock beaker (Fig. 15d), and there were discrepancies in detected Fe concentrations for the ZVI stock based on sampling time—the sample that was taken 5 minutes after preparation showed a much lower Fe concentration than those taken directly after preparation. As the ZVI solution was injected for a duration of longer than 5 minutes at all flow speeds, sedimentation could have had an impact on the intended injected S-mZVI concentration. Because of sedimentation, the location of the pump tube in the beaker could also have had an impact—if it was placed lower, more S-mZVI would have been injected into the column.

Hydrus modeling indicated irreversible attachment of S-mZVI particles: as with nZVI in Berggren Kleja et al. 2024, S-mZVI's k values increased linearly with flow rate (Fig. 38). Under unfavorable conditions, as were present here, the k value is expected to decrease with increasing flow rate, as a higher flow rate means that colloid particles are more likely to detach from surfaces (Li et al. 2005). The opposite is true, however, if particles attach irreversibly (Zhang et al. 2018). The increase of k values with flow rate therefore suggests that S-mZVI behavior should be modeled as irreversibly attaching particles. No consistent pattern in recovery or breakthrough curves, as well as poor model-experimental fit, however, indicates that simple irreversible attachment models were not capable of accurately assessing k values; other factors need to be included for more precise results.

Breakthrough curves showed evidence of heavy blocking (Fig. 39), demonstrated by a gradual rise in the breakthrough curve rather than a simple plateau, where there is a lower deposition rate with increased number of attached particles (Saiers et al. 1994). This pattern appears because, when blocking occurs, the initial attachment of colloids on porous media negatively affects the attachment of further colloids (Phenrat et al. 2019). S-mZVI breakthrough curves did not show a plateau at all, and instead had a gradual rise followed by a steep drop. Breakthrough curve asymmetry and blocking have been seen before with nanoparticles (Chowdhury et al. 2011; Kasel et al. 2013; Sun et al. 2015) and with nZVI, both sulfidized and uncoated (Berggren Kleja et al. 2024; Veselská et al. 2024). Heavy blocking could prove to be advantageous for distribution in the field, as particles injected initially can bind to the colloid and help subsequent particles spread farther in the aquifer. In fact, it has been found that increasing the concentration of injected nanomaterials that are subject to blocking lowers the particle retention rate on colloids, leading to higher recovery and mobility—a higher particle concentration leads to attachment sites filling more quickly upon injection, decreasing the overall retention rate as subsequent particles pass through the porous medium (Sun et al. 2015). It is therefore important to consider blocking when examining S-mZVI's potential in the field, as blocking could greatly improve distribution when S-mZVI is injected on a much larger scale than in the lab.

Although adding blocking improved the model fit, the overall model fit was still poor (Fig. 39e–d). Blocking leads to second-order colloid deposition kinetics (Saiers et al. 1994), but Hydrus-1D can only model first-order deposition (Šimůnek et al. 2018), likely for the sake of simplicity. Without second-order deposition, the *k*-values obtained in this study are likely overly simplified. Miscalculated dead time could also be a factor in poor experimental fit, as it leads to a shift in the experimental curve—here it could be overestimated, as the experimental curve is shifted to the right.

7. Conclusion

Groundwater and soil samples, along with follow-up x-ray absorption spectroscopy measurements, were collected to analyze the limited effectiveness of ZVI injections 2 years prior on As groundwater levels. Although results showed that mZVI chemistry worked somewhat on a very local scale, aggregation, from high injection pressures and fracturing, was the primary limiting factor in lack of As immobilization. In comparison, nZVI was not aggregated, therefore showing some effect on groundwater chemistry. However, it was limited to upper layers of the aquifer as distribution was not homogeneous enough to have a large-scale impact. These results confirmed our hypothesis that distribution was the primary limiting factor in the injections' impact. However, field conditions also played a role. Firstly, more reducing conditions in the field compared to the lab led to increased As(III) dominance over As(V), reducing the ability of As to bind to ZVI. Anoxic conditions also favored S-mediated immobilization mechanisms, which had not been observed in the lab. Finally, high levels of nZVI were found as uncorroded Fe(0), possibly from the low temperature of the aquifer.

Overall, we do not recommend the use of mZVI or nZVI at this site. mZVI was practically completely ineffective. And, although more effective, nZVI would need to be applied at higher concentrations and with better distribution—nZVI is expensive and technically difficult to distribute, especially at lower depths in this aquifer, making it a poor choice as a remediation strategy. Additionally, as Fe(0) remained, even after 2 years in the field, there is no knowledge of whether changes in groundwater conditions would prevail after full ZVI oxidation.

There were several key limitations in field and XAS work in this study. First, there was a lack of soil samples, both at the mZVI site and, more importantly, at the nZVI site, due to mechanical issues and time restrictions. For mZVI soil samples, mechanical issues also led to gaps in data within soil samples. Additionally, there were no pre-injection soil samples, making post-injection analysis of solid-phase Fe and As difficult. Finally, an XAS mapping technique (e.g. a hard x-ray microprobe) could have led to more comprehensive XAS results, rather than bulk sampling, due to the heterogeneity of the samples.

Column experiments with S-mZVI showed very low recovery, indicating a rejection of our hypothesis that it would be more mobile than the injected forms of ZVI. Nevertheless, S-mZVI could still be mobile in the field. First, the sediment in the column experiments was more compact than in the field, limiting S-mZVI movement. Additionally, column experiments only examined vertical distribution, not radial distribution; radial movement would contribute to increased S-mZVI mobility. Finally, blocking could be beneficial for distribution. Despite the heterogeneous distribution of previous injections, S-mZVI could still prove to be a successful remediation strategy at this site.

References

- Ahn, J.-Y., Kim, C., Jun, S.-C. & Hwang, I. (2021). Field-scale investigation of nanoscale zero-valent iron (NZVI) injection parameters for enhanced delivery of NZVI particles to groundwater. *Water Research*, 202, 117402. https://doi.org/10.1016/j.watres.2021.117402
- Augustsson, A., Sörme, L., Karlsson, A. & Amneklev, J. (2017). Persistent Hazardous Waste and the Quest Toward a Circular Economy: The Example of Arsenic in Chromated Copper Arsenate—Treated Wood. *Journal of Industrial Ecology*, 21 (3), 689–699. https://doi.org/10.1111/jiec.12516
- Bang, S., Johnson, M.D., Korfiatis, G.P. & Meng, X. (2005a). Chemical reactions between arsenic and zero-valent iron in water. *Water Research*, 39 (5), 763–770. https://doi.org/10.1016/j.watres.2004.12.022
- Bang, S., Korfiatis, G. & Meng, X. (2005b). Removal of arsenic from water by zero-valent iron. *Journal of Hazardous Materials*, 121 (1–3), 61–67. https://doi.org/10.1016/j.jhazmat.2005.01.030
- Berggren Kleja, D., Cornelis, G., Formentini, T.A., Gustafsson, J.P., Jarsjö, J., Cao, F., Hallgren, P., Englöv, P., Christensen, A.G., Lilbæk, G. & Prinds Hedegaard, L. (2024). *Utveckling och test och av nanojärn för in situbehandling av arsenikförorenat anaerobt grundvatten, Resultat från laboratorie- och pilotskaleförsök*. (Tuffo 1.1-1905-0340). Statens geotekniska institut, SGI.
- Bethke, C.M. (2022). *Geochemical and Biogeochemical Reaction Modeling*. Cambridge University Press.
- Bianco, C., Tosco, T. & Sethi, R. (2018). *Micro- and Nanoparticles transport filtration and clogging Model Suite*. Politecninco di Torino. https://areeweb.polito.it/ricerca/groundwater/software/mnms/
- Cao, F., Kleja, D.B., Tiberg, C. & Jarsjö, J. (2023). Large-scale arsenic mobilization from legacy sources in anoxic aquifers: Multiple methods and multi-decadal perspectives. *Science of The Total Environment*, 892, 164565. https://doi.org/10.1016/j.scitotenv.2023.164565
- Castaño, A., Prosenkov, A., Baragaño, Ď., Otaegui, N., Sastre, H., Rodríguez-Valdés, E., Gallego, J.L.R. & Peláez, A.I. (2021). Effects of in situ Remediation With Nanoscale Zero Valence Iron on the Physicochemical Conditions and Bacterial Communities of Groundwater Contaminated With Arsenic. *Frontiers in Microbiology*, 12, 643589. https://doi.org/10.3389/fmicb.2021.643589
- Chen, H. & Qian, L. (2024). Performance of field demonstration nanoscale zerovalent iron in groundwater remediation: A review. *Science of The Total Environment*, 912, 169268. https://doi.org/10.1016/j.scitotenv.2023.169268
- Chowdhury, I., Hong, Y., Honda, R.J. & Walker, S.L. (2011). Mechanisms of TiO2 nanoparticle transport in porous media: Role of solution chemistry, nanoparticle concentration, and flowrate. *Journal of Colloid and Interface Science*, 360 (2), 548–555. https://doi.org/10.1016/j.jcis.2011.04.111
- Comba, S. & Braun, J. (2012). A new physical model based on cascading column experiments to reproduce the radial flow and transport of micro-iron particles. *Journal of Contaminant Hydrology*, 140–141, 1–11. https://doi.org/10.1016/j.jconhyd.2012.07.003
- Comba, S., Di Molfetta, A. & Sethi, R. (2011). A Comparison Between Field Applications of Nano-, Micro-, and Millimetric Zero-Valent Iron for the Remediation of Contaminated Aquifers. *Water, Air, & Soil Pollution*, 215 (1–4), 595–607. https://doi.org/10.1007/s11270-010-0502-1

- Dalla Vecchia, E., Coisson, M., Appino, C., Vinai, F. & Sethi, R. (2009).

 Magnetic Characterization and Interaction Modeling of Zerovalent Iron
 Nanoparticles for the Remediation of Contaminated Aquifers. *Journal of Nanoscience and Nanotechnology*, 9 (5), 3210–3218.

 https://doi.org/10.1166/jnn.2009.047
- Dixit, S. & Hering, J.G. (2003). Comparison of Arsenic(V) and Arsenic(III) Sorption onto Iron Oxide Minerals: Implications for Arsenic Mobility. *Environmental Science & Technology*, 37 (18), 4182–4189. https://doi.org/10.1021/es030309t
- Driessen, P.M., International Soil Reference and Information Centre, & FAO (eds) (2001). *Lecture notes on the major soils of the world*. Food and Agriculture Organization of the United Nations. (World soil resources reports; 94)
- Elimelech, M., Gregory, J. & Jia, X. (2013). *Particle Deposition and Aggregation: Measurement, Modelling and Simulation*. Butterworth-Heinemann.
- Ersenkal, D.A., Ziylan, A., Ince, N.H., Acar, H.Y., Demirer, M. & Copty, N.K. (2011). Impact of dilution on the transport of poly(acrylic acid) supported magnetite nanoparticles in porous media. *Journal of Contaminant Hydrology*, 126 (3–4), 248–257. https://doi.org/10.1016/j.jconhyd.2011.09.005
- European Economic Community (EEC) (2003). relating to restrictions on the marketing and use of arsenic (tenth adaptation to technical progress to Council Directive 76/769/EEC). 9–11. https://eurlex.europa.eu/eli/dir/2003/2/oj/eng [2025-07-11]
- Fan, D., Anitori, R.P., Tebo, B.M., Tratnyek, P.G., Lezama Pacheco, J.S., Kukkadapu, R.K., Engelhard, M.H., Bowden, M.E., Kovarik, L. & Arey, B.W. (2013). Reductive Sequestration of Pertechnetate (⁹⁹ TcO₄⁻) by Nano Zerovalent Iron (nZVI) Transformed by Abiotic Sulfide. *Environmental Science & Technology*, 47 (10), 5302–5310. https://doi.org/10.1021/es304829z
- Farrell, J., Wang, J., O'Day, P. & Conklin, M. (2001). Electrochemical and Spectroscopic Study of Arsenate Removal from Water Using Zero-Valent Iron Media. *Environmental Science & Technology*, 35 (10), 2026–2032. https://doi.org/10.1021/es0016710
- Flores Orozco, A., Velimirovic, M., Tosco, T., Kemna, A., Sapion, H., Klaas, N., Sethi, R. & Bastiaens, L. (2015). Monitoring the Injection of Microscale Zerovalent Iron Particles for Groundwater Remediation by Means of Complex Electrical Conductivity Imaging. *Environmental Science & Technology*, 49 (9), 5593–5600. https://doi.org/10.1021/acs.est.5b00208
- Formentini, T.A., Cornelis, G., Gustafsson, J.P., Leicht, K., Tiberg, C., Planer-Friedrich, B., Durant, N., Fan, D. & Kleja, D.B. (2024). Immobilizing arsenic in contaminated anoxic aquifer sediment using sulfidated and uncoated zero-valent iron (ZVI). *Journal of Hazardous Materials*, 462, 132743. https://doi.org/10.1016/j.jhazmat.2023.132743
- Fu, F., Dionysiou, D.D. & Liu, H. (2014). The use of zero-valent iron for groundwater remediation and wastewater treatment: A review. *Journal of Hazardous Materials*, 267, 194–205. https://doi.org/10.1016/j.jhazmat.2013.12.062
- Gastone, F., Tosco, T. & Sethi, R. (2014). Green stabilization of microscale iron particles using guar gum: Bulk rheology, sedimentation rate and enzymatic degradation. *Journal of Colloid and Interface Science*, 421, 33–43. https://doi.org/10.1016/j.jcis.2014.01.021
- Gong, L., Shi, S., Lv, N., Xu, W., Ye, Z., Gao, B., O'Carroll, D.M. & He, F. (2020). Sulfidation enhances stability and mobility of carboxymethyl

- cellulose stabilized nanoscale zero-valent iron in saturated porous media. *Science of The Total Environment*, 718, 137427. https://doi.org/10.1016/j.scitotenv.2020.137427
- Gustafsson, J.P. (2013). Visual Minteg (3.1). https://vminteq.com/
- Gustafsson, J.P. (2022). LCF-Linest, version 1.1. *Visual MINTEQ*. https://vminteq.com/lcf-linest/ [2025-09-04]
- Gustafsson, J.P., Jacks, G., Simonsson, M. & Nilsson, I. (2007). Soil and water chemistry. KTH, Department of Land and Water Resources Engineering.
- Harbaugh, A.W. (2005). MODFLOW-2005: the U.S. Geological Survey modular ground-water model--the ground-water flow process. (6-A16). https://pubs.usgs.gov/publication/tm6A16 [2025-06-19]
- He, F., Zhao, D. & Paul, C. (2010). Field assessment of carboxymethyl cellulose stabilized iron nanoparticles for in situ destruction of chlorinated solvents in source zones. *Water Research*, 44 (7), 2360–2370. https://doi.org/10.1016/j.watres.2009.12.041
- Hydutsky, B.W., Mack, E.J., Beckerman, B.B., Skluzacek, J.M. & Mallouk, T.E. (2007). Optimization of Nano- and Microiron Transport through Sand Columns Using Polyelectrolyte Mixtures. *Environmental Science & Technology*, 41 (18), 6418–6424. https://doi.org/10.1021/es0704075
- International Union of Pure and Applied Chemistry (IUPAC) (2003). Definitions, Terminology, and Symbols in Colloid and Surface Chemistry. *Chemistry International -- Newsmagazine for IUPAC*, 25 (1). https://doi.org/10.1515/ci.2003.25.1.18c
- Johnson, Ř.L., Nurmi, J.T., O'Brien Johnson, G.S., Fan, D., O'Brien Johnson, R.L., Shi, Z., Salter-Blanc, A.J., Tratnyek, P.G. & Lowry, G.V. (2013). Field-Scale Transport and Transformation of Carboxymethylcellulose-Stabilized Nano Zero-Valent Iron. *Environmental Science & Technology*, 47 (3), 1573–1580. https://doi.org/10.1021/es304564q
 Kanel, S.R., Grenèche, J.-M. & Choi, H. (2006). Arsenic(V) Removal from
- Kanel, S.R., Grenèche, J.-M. & Choi, H. (2006). Arsenic(V) Removal from Groundwater Using Nano Scale Zero-Valent Iron as a Colloidal Reactive Barrier Material. *Environmental Science & Technology*, 40 (6), 2045– 2050. https://doi.org/10.1021/es0520924
- Kanel, S.R., Manning, B., Charlet, L. & Choi, H. (2005). Removal of Arsenic(III) from Groundwater by Nanoscale Zero-Valent Iron. *Environmental Science & Technology*, 39 (5), 1291–1298. https://doi.org/10.1021/es048991u
- Karimian, N., Johnston, S.G. & Burton, E.D. (2018). Iron and sulfur cycling in acid sulfate soil wetlands under dynamic redox conditions: A review. *Chemosphere*, 197, 803–816. https://doi.org/10.1016/j.chemosphere.2018.01.096
- Kasel, D., Bradford, S.A., Šimůnek, J., Heggen, M., Vereecken, H. & Klumpp, E. (2013). Transport and retention of multi-walled carbon nanotubes in saturated porous media: Effects of input concentration and grain size. *Water Research*, 47 (2), 933–944. https://doi.org/10.1016/j.watres.2012.11.019
- Kim, I. & Cha, D.K. (2021). Effect of low temperature on abiotic and biotic nitrate reduction by zero-valent Iron. *Science of The Total Environment*, 754, 142410. https://doi.org/10.1016/j.scitotenv.2020.142410
- Köber, R., Hollert, H., Hornbruch, G., Jekel, M., Kamptner, A., Klaas, N., Maes, H., Mangold, K.-M., Martac, E., Matheis, A., Paar, H., Schäffer, A., Schell, H., Schiwy, A., Schmidt, K.R., Strutz, T.J., Thümmler, S., Tiehm, A. & Braun, J. (2014). Nanoscale zero-valent iron flakes for groundwater treatment. *Environmental Earth Sciences*, 72 (9), 3339–3352. https://doi.org/10.1007/s12665-014-3239-0
- Kocar, B.D., Borch, T. & Fendorf, S. (2010). Arsenic repartitioning during biogenic sulfidization and transformation of ferrihydrite. *Geochimica et*

- Cosmochimica Acta, 74 (3), 980–994. https://doi.org/10.1016/j.gca.2009.10.023
- Kocur, C.M., Chowdhury, A.I., Sakulchaicharoen, N., Boparai, H.K., Weber, K.P., Sharma, P., Krol, M.M., Austrins, L., Peace, C., Sleep, B.E. & O'Carroll, D.M. (2014). Characterization of nZVI Mobility in a Field Scale Test. *Environmental Science & Technology*, 48 (5), 2862–2869. https://doi.org/10.1021/es4044209
- Kocur, C.M., O'Carroll, D.M. & Sleep, B.E. (2013). Impact of nZVI stability on mobility in porous media. *Journal of Contaminant Hydrology*, 145, 17–25. https://doi.org/10.1016/j.jconhyd.2012.11.001
- Kosmulski, M. (2004). pH-dependent surface charging and points of zero charge II. Update. *Journal of Colloid and Interface Science*, 275 (1), 214–224. https://doi.org/10.1016/j.jcis.2004.02.029
- Kumar, N., Auffan, M., Gattacceca, J., Rose, J., Olivi, L., Borschneck, D., Kvapil, P., Jublot, M., Kaifas, D., Malleret, L., Doumenq, P. & Bottero, J.-Y. (2014). Molecular Insights of Oxidation Process of Iron Nanoparticles: Spectroscopic, Magnetic, and Microscopic Evidence. *Environmental Science & Technology*, 48 (23), 13888–13894. https://doi.org/10.1021/es503154q
- Kwon, E., Zhang, H., Wang, Z., Jhangri, G.S., Lu, X., Fok, N., Gabos, S., Li, X.-F. & Le, X.C. (2004). Arsenic on the Hands of Children after Playing in Playgrounds. *Environmental Health Perspectives*, 112 (14), 1375–1380. https://doi.org/10.1289/ehp.7197
- Lackovic, J.A., Nikolaidis, N.P. & Dobbs, G.M. (2000). Inorganic Arsenic Removal by Zero-Valent Iron. *Environmental Engineering Science*, 17 (1), 29–39. https://doi.org/10.1089/ees.2000.17.29
- Langner, P., Mikutta, C. & Kretzschmar, R. (2012). Arsenic sequestration by organic sulphur in peat. *Nature Geoscience*, 5 (1), 66–73. https://doi.org/10.1038/ngeo1329
- Laperche, V. & Lemière, B. (2020). Possible Pitfalls in the Analysis of Minerals and Loose Materials by Portable XRF, and How to Overcome Them. *Minerals*, 11 (1), 33. https://doi.org/10.3390/min11010033
- Li, X., Zhang, P., Lin, C.L. & Johnson, W.P. (2005). Role of Hydrodynamic Drag on Microsphere Deposition and Re-entrainment in Porous Media under Unfavorable Conditions. *Environmental Science & Technology*, 39 (11), 4012–4020. https://doi.org/10.1021/es048814t
- Liao, X., Li, Y., Miranda-Avilés, R., Zha, X., Anguiano, J.H.H., Moncada Sánchez, C.D., Puy-Alquiza, M.J., González, V.P. & Garzon, L.F.R. (2022). In situ remediation and ex situ treatment practices of arsenic-contaminated soil: An overview on recent advances. *Journal of Hazardous Materials Advances*, 8, 100157. https://doi.org/10.1016/j.hazadv.2022.100157
- Lien, H.-L. & Wilkin, R.T. (2005). High-level arsenite removal from groundwater by zero-valent iron. *Chemosphere*, 59 (3), 377–386. https://doi.org/10.1016/j.chemosphere.2004.10.055
- Lindau, L. (1977). Emissions of arsenic in Sweden and their reduction. Environmental Health Perspectives, 19, 25–20
- Livsmedelsverket (2025). *Arsenik. Livsmedelsverket*. https://www.livsmedelsverket.se/livsmedel-och-innehall/oonskade-amnen/metaller1/arsenik [2025-06-16]
- Luna, M., Gastone, F., Tosco, T., Sethi, R., Velimirovic, M., Gemoets, J., Muyshondt, R., Sapion, H., Klaas, N. & Bastiaens, L. (2015). Pressure-controlled injection of guar gum stabilized microscale zerovalent iron for groundwater remediation. *Journal of Contaminant Hydrology*, 181, 46–58. https://doi.org/10.1016/j.jconhyd.2015.04.007

- Lv, D., Zhou, J., Cao, Z., Xu, J., Liu, Y., Li, Y., Yang, K., Lou, Z., Lou, L. & Xu, X. (2019). Mechanism and influence factors of chromium(VI) removal by sulfide-modified nanoscale zerovalent iron. *Chemosphere*, 224, 306–315. https://doi.org/10.1016/j.chemosphere.2019.02.109
- Manning, B.A., Hunt, M.L., Amrhein, C. & Yarmoff, J.A. (2002). Arsenic(III) and Arsenic(V) Reactions with Zerovalent Iron Corrosion Products. *Environmental Science & Technology*, 36 (24), 5455–5461. https://doi.org/10.1021/es0206846
- Mohammed Abdul, K.S., Jayasinghe, S.S., Chandana, E.P.S., Jayasumana, C. & De Silva, P.M.C.S. (2015). Arsenic and human health effects: A review. *Environmental Toxicology and Pharmacology*, 40 (3), 828–846. https://doi.org/10.1016/j.etap.2015.09.016
- Moon, K., Guallar, E. & Navas-Acien, A. (2012). Arsenic Exposure and Cardiovascular Disease: An Updated Systematic Review. *Current Atherosclerosis Reports*, 14 (6), 542–555. https://doi.org/10.1007/s11883-012-0280-x
- National Academies of Sciences (NAS), Engineering, and Medicine (1977).

 Arsenic: Medical and Biological Effects of Environmental Pollutants. In:

 Arsenic: Medical and Biological Effects of Environmental Pollutants. The National Academies Press. https://doi.org/10.17226/9003
- Ng, J.C., Wang, J. & Shraim, A. (2003). A global health problem caused by arsenic from natural sources. *Chemosphere*, 52 (9), 1353–1359. https://doi.org/10.1016/S0045-6535(03)00470-3
- Norrfors, K.K., Micić, V., Borovinskaya, O., Von Der Kammer, F., Hofmann, T. & Cornelis, G. (2021). A critical evaluation of short columns for estimating the attachment efficiency of engineered nanomaterials in natural soils. *Environmental Science: Nano*, 8 (6), 1801–1814. https://doi.org/10.1039/D0EN01089H
- Nyström, S. (2022). Long-term Effect of Metallic Iron Sorbents on Arsenic Mobility in an Anoxic Aquifer—An assessment based on long-term column experiments. Swedish University of Agricultural Sciences.
- O'Day, P.A., Vlassopoulos, D., Root, R. & Rivera, N. (2004). The influence of sulfur and iron on dissolved arsenic concentrations in the shallow subsurface under changing redox conditions. *Proceedings of the National Academy of Sciences*, 101 (38), 13703–13708. https://doi.org/10.1073/pnas.0402775101
- Otaegi, N. & Cagigal, E. (2017). NanoRem Pilot Site–Nitrastur, Spain: remediation of arsenic in groundwater using nanoscale zero-valent iron. NanoRem. http://www.na norem.eu/
- Petosa, A.R., Jaisi, D.P., Quevedo, I.R., Elimelech, M. & Tufenkji, N. (2010). Aggregation and Deposition of Engineered Nanomaterials in Aquatic Environments: Role of Physicochemical Interactions. *Environmental Science & Technology*, 44 (17), 6532–6549. https://doi.org/10.1021/es100598h
- Phenrat, T., Babakhani, P., Bridge, J., Doong, R. & Lowry, G.V. (2019).

 Mechanistic, Mechanistic-Based Empirical, and Continuum-Based
 Concepts and Models for the Transport of Polyelectrolyte-Modified
 Nanoscale Zerovalent Iron (NZVI) in Saturated Porous Media. In:

 Nanoscale Zerovalent Iron Particles for Environmental Restoration: From
 Fundamental Science to Field Scale Engineering Applications. Springer
 International Publishing. 235–292. https://doi.org/10.1007/978-3-319-95340-3
- Phenrat, T., Saleh, N., Sirk, K., Tilton, R.D. & Lowry, G.V. (2007). Aggregation and Sedimentation of Aqueous Nanoscale Zerovalent Iron Dispersions.

- *Environmental Science & Technology*, 41 (1), 284–290. https://doi.org/10.1021/es061349a
- Podgorski, J. & Berg, M. (2020). Global threat of arsenic in groundwater. *Science*, 368 (6493), 845–850. https://doi.org/10.1126/science.aba1510
- Ponder, S.M., Darab, J.G. & Mallouk, T.E. (2000). Remediation of Cr(VI) and Pb(II) Aqueous Solutions Using Supported, Nanoscale Zero-valent Iron. *Environmental Science & Technology*, 34 (12), 2564–2569. https://doi.org/10.1021/es9911420
- Randall, S.R., Sherman, D.M. & Ragnarsdottir, K.V. (2000). Sorption of As(V) on green rust (Fe4(II)Fe2(III)(OH)12SO4 z 3H2O) and lepidocrocite (g-FeOOH): Surface complexes from EXAFS spectroscopy. *Geochimica et Cosmochimica Acta*, 65 (7), 1015–1023. https://doi.org/10.1016/S0016-7037(00)00593-7
- Ravel, B. & Newville, M. (2005). Athena, Artemis, Hephaestus: data analysis for X-ray absorption spectroscopy using IFEFFIT. *Journal of Synchrotron Radiation*, 12, 537–541. https://doi.org/10.1107/S0909049505012719
- Saiers, J.E., Hornberger, G.M. & Liang, L. (1994). First- and second-order kinetics approaches for modeling the transport of colloidal particles in porous media. *Water Resources Research*, 30 (9), 2499–2506. https://doi.org/10.1029/94WR01046
- Schrick, B., Hydutsky, B.W., Blough, J.L. & Mallouk, T.E. (2004). Delivery Vehicles for Zerovalent Metal Nanoparticles in Soil and Groundwater. *Chemistry of Materials*, 16 (11), 2187–2193. https://doi.org/10.1021/cm0218108
- Shan, H., Zhang, J., Peng, S., Zhan, H. & Liao, D. (2021). Sorption of Monothioarsenate to the Natural Sediments and Its Competition with Arsenite and Arsenate. *International Journal of Environmental Research and Public Health*, 18 (23), 12839. https://doi.org/10.3390/ijerph182312839
- Shi, Z., Fan, D., Johnson, R.L., Tratnyek, P.G., Nurmi, J.T., Wu, Y. & Williams, K.H. (2015). Methods for characterizing the fate and effects of nano zerovalent iron during groundwater remediation. *Journal of Contaminant Hydrology*, 181, 17–35. https://doi.org/10.1016/j.jconhyd.2015.03.004
- Simunek, J., Diederik, J., Langergraber, G., Bradford, S.A., Sejna, M. & van Genuchten, M. (2013). Numerical Modeling of Contaminant Transport Using HYDRUS and its Specialized Modules. *Journal of the Indian Institute of Science*, 93 (2). https://escholarship.org/uc/item/15h5w3jr
- Šimůnek, J., Šejna, M., Saito, H., Sakai, M. & van Genuchten, M.T. (2018). The HYDRUS-1D Software Package for Simulating the One-Dimensional Movement of Water, Heat, and Multiple Solutes in Variably-Saturated Media. Department of Environmental Sciences, University of California Riverside.
- Singh, P., Pal, P., Mondal, P., Saravanan, G., Nagababu, P., Majumdar, S., Labhsetwar, N. & Bhowmick, S. (2021). Kinetics and mechanism of arsenic removal using sulfide-modified nanoscale zerovalent iron. *Chemical Engineering Journal*, 412, 128667. https://doi.org/10.1016/j.cej.2021.128667
- Song, Shikun., Su, Yiming., Adeleye, A.S., Zhang, Yalei. & Zhou, Xuefei. (2017). Optimal design and characterization of sulfide-modified nanoscale zerovalent iron for diclofenac removal. *Applied Catalysis B: Environmental*, 201, 211–220. https://doi.org/10.1016/j.apcatb.2016.07.055
- Su, C. & Puls, R.W. (2001). Arsenate and Arsenite Removal by Zerovalent Iron: Kinetics, Redox Transformation, and Implications for in Situ Groundwater

- Remediation. *Environmental Science & Technology*, 35 (7), 1487–1492. https://doi.org/10.1021/es001607i
- Su, C., Puls, R.W., Krug, T.A., Watling, M.T., O'Hara, S.K., Quinn, J.W. & Ruiz, N.E. (2013). Travel distance and transformation of injected emulsified zerovalent iron nanoparticles in the subsurface during two and half years. *Water Research*, 47 (12), 4095–4106. https://doi.org/10.1016/j.watres.2012.12.042
- Su, Y., Adeleye, A.S., Keller, A.A., Huang, Y., Dai, C., Zhou, X. & Zhang, Y. (2015). Magnetic sulfide-modified nanoscale zerovalent iron (S-nZVI) for dissolved metal ion removal. *Water Research*, 74, 47–57. https://doi.org/10.1016/j.watres.2015.02.004
- Su, Y., Jassby, D., Zhang, Y., Keller, A.A. & Adeleye, A.S. (2020). Comparison of the colloidal stability, mobility, and performance of nanoscale zerovalent iron and sulfidated derivatives. *Journal of Hazardous Materials*, 396, 122691. https://doi.org/10.1016/j.jhazmat.2020.122691
- Su, Y., Lowry, G.V., Jassby, D. & Zhang, Y. (2019). Sulfide-Modified NZVI (SNZVI): Synthesis, Characterization, and Reactivity. In: Phenrat, T. & Lowry, G. (eds) Nanoscale Zerovalent Iron Particles for Environmental Restoration: From Fundamental Science to Field Scale Engineering Applications. Springer International Publishing. 359–386. https://doi.org/10.1007/978-3-319-95340-3_9
 Sun, Y., Gao, B., Bradford, S.A., Wu, L., Chen, H., Shi, X. & Wu, J. (2015).
- Sun, Y., Gao, B., Bradford, S.A., Wu, L., Chen, H., Shi, X. & Wu, J. (2015). Transport, retention, and size perturbation of graphene oxide in saturated porous media: Effects of input concentration and grain size. *Water Research*, 68, 24–33. https://doi.org/10.1016/j.watres.2014.09.025
- Sweco Environment AB & Telia Net Fastigheter AB (2019). Miljöutredning Etapp 2. Utredning rörande föroreningsförhållandena vid den f.d. impregneringsanläggningen i Hjältevad genomförd i samarbete med Statens Geotekniska Institut och Institutionen för Naturgeografi vid Stockholms Universitet.
- Sweco Sverige AB (2025). Årsrapport: Rapport Avseende Grundvattenprovtagning vid den F.D. Impregneringsanläggningen i Hjältevad
- Tiraferri, A., Chen, K.L., Sethi, R. & Elimelech, M. (2008). Reduced aggregation and sedimentation of zero-valent iron nanoparticles in the presence of guar gum. *Journal of Colloid and Interface Science*, 324 (1–2), 71–79. https://doi.org/10.1016/j.jcis.2008.04.064
- Truex, M. j., Vermeul, V. r., Mendoza, D. p., Fritz, B. g., Mackley, R. d., Oostrom, M., Wietsma, T. w. & Macbeth, T. w. (2011). Injection of Zero-Valent Iron into an Unconfined Aquifer Using Shear-Thinning Fluids. *Groundwater Monitoring & Remediation*, 31 (1), 50–58. https://doi.org/10.1111/j.1745-6592.2010.01319.x
- Tuček, J., Prucek, R., Kolařík, J., Zoppellaro, G., Petr, M., Filip, J., Sharma, V.K. & Zbořil, R. (2017). Zero-Valent Iron Nanoparticles Reduce Arsenites and Arsenates to As(0) Firmly Embedded in Core–Shell Superstructure: Challenging Strategy of Arsenic Treatment under Anoxic Conditions. *ACS Sustainable Chemistry & Engineering*, 5 (4), 3027–3038. https://doi.org/10.1021/acssuschemeng.6b02698
- Tyrovola, K., Nikolaidis, N.P., Veranis, N., Kallithrakas-Kontos, N. & Koulouridakis, P.E. (2006). Arsenic removal from geothermal waters with zero-valent iron—Effect of temperature, phosphate and nitrate. *Water Research*, 40 (12), 2375–2386. https://doi.org/10.1016/j.watres.2006.04.006
- Velimirovic, M., Chen, H., Simons, Q. & Bastiaens, L. (2012). Reactivity recovery of guar gum coupled mZVI by means of enzymatic breakdown

- and rinsing. *Journal of Contaminant Hydrology*, 142–143, 1–10. https://doi.org/10.1016/j.jconhyd.2012.09.003
- Velimirovic, M., Tosco, T., Uyttebroek, M., Luna, M., Gastone, F., De Boer, C., Klaas, N., Sapion, H., Eisenmann, H., Larsson, P.-O., Braun, J., Sethi, R. & Bastiaens, L. (2014). Field assessment of guar gum stabilized microscale zerovalent iron particles for in-situ remediation of 1,1,1-trichloroethane. *Journal of Contaminant Hydrology*, 164, 88–99. https://doi.org/10.1016/j.jconhyd.2014.05.009
- Veselská, V., Magherini, L., Bianco, C., Šembera, J., Parma, P., Víchová, V., Sethi, R. & Filip, J. (2024). Unveiling trends in migration of iron-based nanoparticles in saturated porous media. *Journal of Environmental Management*, 370, 122552. https://doi.org/10.1016/j.jenvman.2024.122552
- Wei, Y.-T., Wu, S.-C., Chou, C.-M., Che, C.-H., Tsai, S.-M. & Lien, H.-L. (2010). Influence of nanoscale zero-valent iron on geochemical properties of groundwater and vinyl chloride degradation: A field case study. *Water Research*, 44 (1), 131–140. https://doi.org/10.1016/j.watres.2009.09.012
- Wilkin, R.T., Acree, S.D., Beak, D.G., Ross, R.R., Lee, T.R. & Paul, C.J. (2008). Field Application of a Permeable Reactive Barrier for Treatment of Arsenic in Ground Water. (EPA 600/R-08/093). U.S. Environmental Protection Agency.
- World Health Organization (2001). Arsenic and Arsenic Compounds. 2nd ed. World Health Organization. (Environmental Health Criteria)
- Wu, D., Peng, S., Yan, K., Shao, B., Feng, Y. & Zhang, Y. (2018). Enhanced As(III) Sequestration Using Sulfide-Modified Nano-Scale Zero-Valent Iron with a Characteristic Core–Shell Structure: Sulfidation and As Distribution. ACS Sustainable Chemistry & Engineering, 6 (3), 3039–3048. https://doi.org/10.1021/acssuschemeng.7b02787
- Yan, W., Vasic, R., Frenkel, A.I. & Koel, B.E. (2012). Intraparticle Reduction of Arsenite (As(III)) by Nanoscale Zerovalent Iron (nZVI) Investigated with In Situ X-ray Absorption Spectroscopy. *Environmental Science & Technology*, 46 (13), 7018–7026. https://doi.org/10.1021/es2039695
- Zhang, C., Yan, A., Wang, G., Jin, C., Chen, Y. & Shen, C. (2018). Impact of Flow Velocity on Transport of Graphene Oxide Nanoparticles in Saturated Porous Media. *Vadose Zone Journal*, 17 (1), 180019. https://doi.org/10.2136/vzj2018.01.0019
- https://doi.org/10.2136/vzj2018.01.0019
 Zhao, J., Su, A., Tian, P., Tang, X., Collins, R.N. & He, F. (2021). Arsenic (III) removal by mechanochemically sulfidated microscale zero valent iron under anoxic and oxic conditions. *Water Research*, 198, 117132. https://doi.org/10.1016/j.watres.2021.117132

Appendix

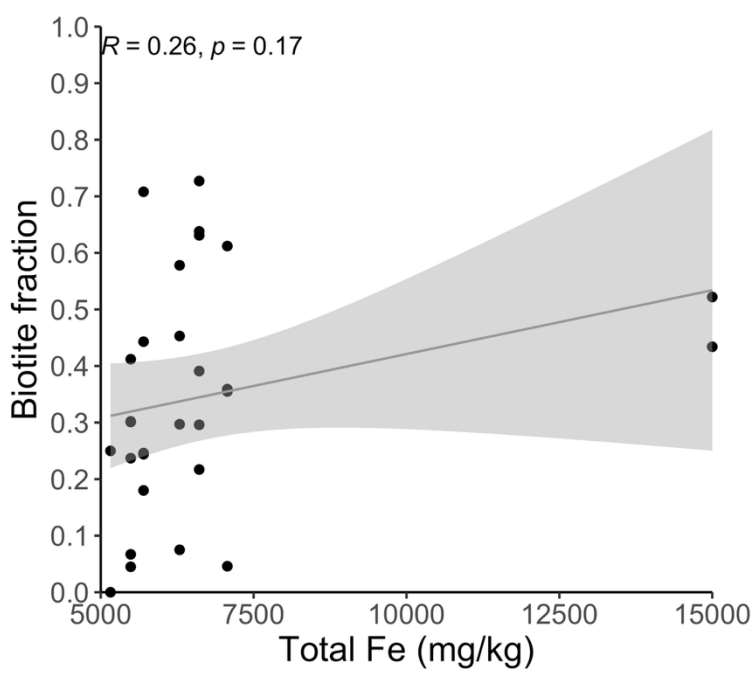


Figure 1. Total solid-phase Fe found in XAS samples sent for analysis at ALS compared to fraction of biotite in each sample.

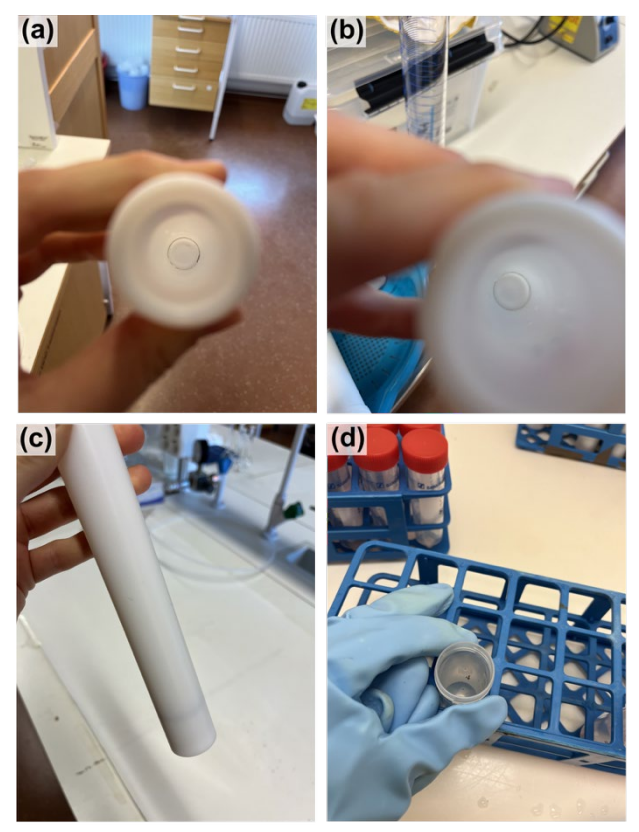


Figure 2. Contamination and poor digestion from batch 1 column tests. Images (a-c) show contamination in two microwave tubes, after scrubbing and dish washing (a and c are the same tube). Image (d) shows presence of ZVI flakes after digestion.

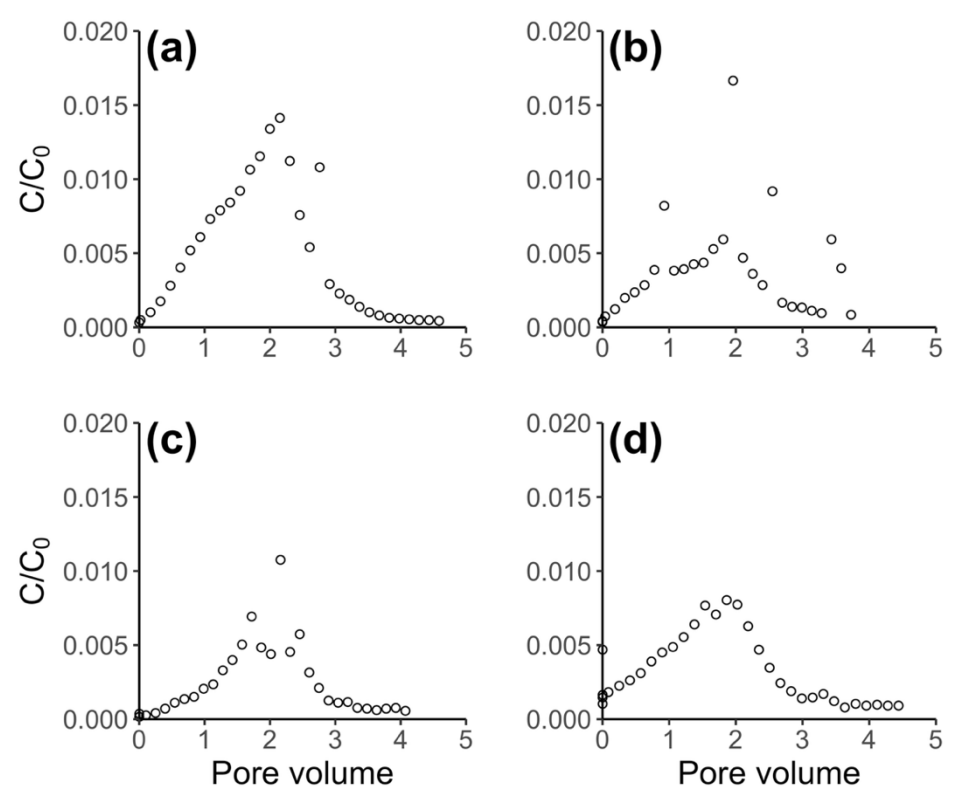


Figure 3. Observed breakthrough curves for first batch of column experiments. Graphs (a-d) correspond to 1.34, 2.69, 3.55, and 5.48 mL min⁻¹, respectively.

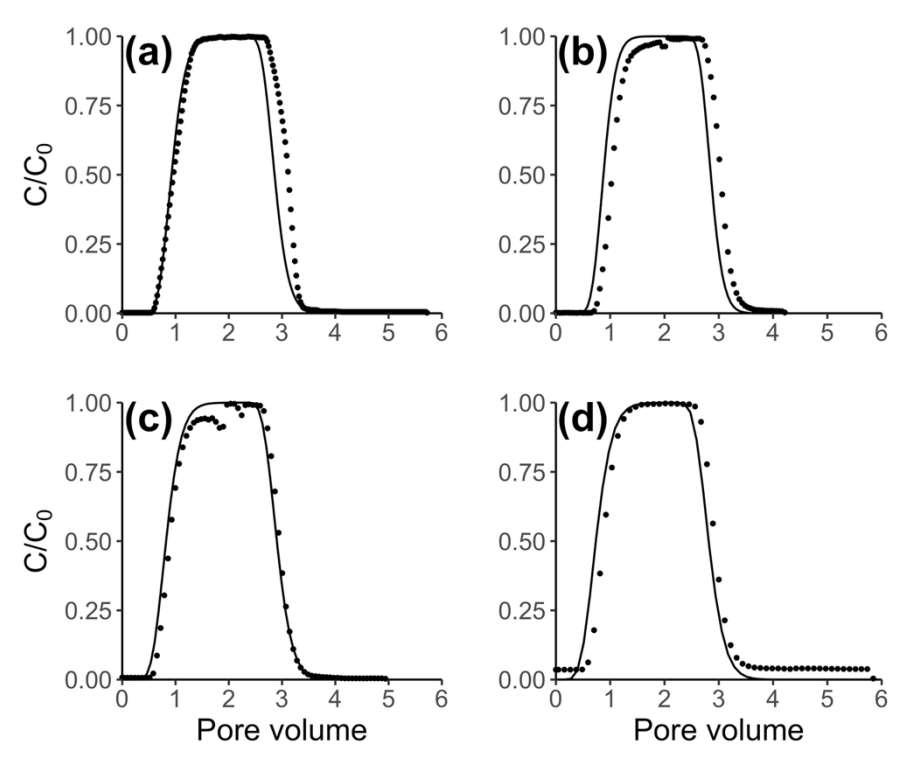


Figure 4. Breakthrough curves for tracers in second batch of column experiments. Flow speeds are: 1.34, 2.67, 3.52, and 5.50 mL min⁻¹ for graphs (a–d), respectively. Circles are experimental values and continuous lines are modeled values.

Table 1. Expected C_0 and measured C_0 in both sets of replicates for column experiments. Expected C_0 is calculated based on the mass of ZVI used in the stock solution and the percentage Fe expected (40%). Measured C_0 is back-calculated from diluted ICP-MS results.

Flow speed (mL/min)	Replicate	Expected C ₀ (mg/L)	Measured C ₀ (mg/L)	Expected C ₀ – measured C ₀
1.34	1	5028	4724.96	303.04
2.69	1	5054	2978.92	2075.08
3.55	1	5062	5028.5	33.5
5.48	1	5016	4104.58	911.42
Average:			4209.24	830.76
Std. Dev.:			905.87	907.18
1.34	2	5018	4135.05	882.95
2.67	2	5086	1390.23	3695.77
3.52	2	5000	4152.24	847.76
5.5	2	5074	4089.33	984.67
Average:			3441.71	1602.7875
Std. Dev.:			1367.91	1396.53

Table 2. Bulk density and recovery for first batch of column experiments.

Flow speed (mL/min)	Bulk density (g/cm ³)	Recovery (%)	
1.34	1.811	1.09	
2.69	1.856	0.74	
3.55	1.887	0.55	
5.48	1.911	0.76	

Publishing and archiving

Approved students' theses at SLU can be published online. As a student you own the copyright to your work and in such cases, you need to approve the publication. In connection with your approval of publication, SLU will process your personal data (name) to make the work searchable on the internet. You can revoke your consent at any time by contacting the library.

Even if you choose not to publish the work or if you revoke your approval, the thesis will be archived digitally according to archive legislation.

You will find links to SLU's publication agreement and SLU's processing of personal data and your rights on this page:

• https://libanswers.slu.se/en/faq/228318

⊠ YES, I, Clara Kieschnick-Llamas, have read and agree to the agreement for
publication and the personal data processing that takes place in connection with
this
\square NO, I/we do not give my/our permission to publish the full text of this work.
However, the work will be uploaded for archiving and the metadata and summary
will be visible and searchable.